Scanning Probe Microscopy

Method Development and Applications to Zinc Oxide Structures

Jon Borgersen

Thesis submitted in partial fulfilment of the requirements for the degree
Master of Science
in
Materials, Energy and Nanotechnology

University of Oslo
Department of Physics
May, 2016

Abstract

Scanning spreading resistance microscopy (SSRM) and scanning capacitance microscopy (SCM) are among the few techniques feasible for characterizing electrical properties on the nanoscale. With the decreasing size of electronic devices, and the interesting physics which occur at these scales, such techiques are of both technological and scientific interest. Unfortunately, SSRM and SCM has seen little use on materials other than silicon, and in particular oxide semiconductors have been scarcely investigated. Part of the reason for this is the lack of a sample preparation routine which allows repeatable and reliable experiments to be made. In this thesis, a systematic study of available sample preparation routines for oxide semiconductors, in particular zinc oxide (ZnO), has been conducted. It has been established that the optimal preparation is dictated by the substrate material, and preparation techniques for silicon, sapphire, and zinc oxide substrates are presented. Seven different probes have been compared, and it is found that the probes coated with a layer of doped diamond yields the best results. Back side contacts realized with silver paste and eutectic indium gallium have also been compared, and it was found that the former provided the best contact. Several Matlab scripts have been produced for processing of the captured data.

With the developed preparation routines, SSRM and SCM have been used to examine a range of zinc oxide thin-film samples currently under research. Specifically, in-diffused, ion implanted, and heterostructure samples have been examined. The former two sample types have been studied to correlate the electrical activity with the dopant profiles acuired from secondary ion mass spectrometry (SIMS). The heterostructures have been measured to see whether the electrical SPM methods could sucessfully detect a two dimensional electron gas (2DEG). Although no 2DEG has been observed, magnesium zinc oxide (MgZnO) barriers and a ZnO quantum well has been successfully delineated by SSRM.

Initial attempts at low temperature SSRM have been made, but has yet to produce reliable results and this is a topic for future work.

Acknowledgements

A sizeable number of people have been involved in the presented work in one way or another. First and foremost I would like to thank my family for their unconditional support in all my endeavours.

I would also like to express my gratitude to Odd-Egil Frogner and Eystein Raude for initially sparking my interest in physics. Further, for tireless day-to-day discussions, instrument training, proofreading of manuscripts, and always keeping his door open I am eternally grateful to associate professor Lasse Vines. On the same note I would also like to thank professor Andrej Kuznetsov for providing an exciting project outline, overall supervision, and his assistance with adjusting the course as the project proceeded. His enthusiasm is contagious and highly motivating in times when results are few and far between. Of course, none of us would have been here had it not been for the commendable leadership of Bengt G. Svensson, so thank you Bengt and congratulations with the Toppforsk funding.

For their assistance and training in all things related to mechanical sample preparation I thank Ole Bjørn Karlsen and Andrey Kosinskiy. Thank you also Oddvar Dyrlie for training on the AFM and for all the useful discussions. In terms of experimental work I am gratelful to Heine Riise, Martin Nyborg, and Per Lindberg for sputter deposition, Josef Ellingsen and Vishnukanthan Venkatachalapathy for MOCVD, Kristian Lausund for high-resolution SEM, Asbjørn Ulvestad for FIB, and Muhammad Tayyib for ion milling. I would like to express my gratitude to Viktor Bobal and Micke Sjödin for keeping the MiNaLab up and running, and to Klaus Magnus Johansen for his useful advice and arrangements related to ion milling. For making the LENS group an inspiring and enjoyable place to work, I would like to thank everyone here and especially my fellow master students.

Last, but definitely not least, I would like to thank Marianne for her constant love, support and encouragement through all my years of studies.

Contents

Chapter 1

Introduction

Solid materials can be classified as conductors, semiconductors, or insulators depending on their ability to conduct electricity, in decreasing order. Although adept neither at conducting nor insulating electrical current, semiconductors are found in all but the very simplest electronic devices in use today. The key property which makes them so useful is not their conductivity in itself, but rather that the conductivity can be tuned in various ways, such as (i) by introduction of impurities into the material's structure, (ii) by changing the temperature, or (iii) by exposure to light. These features are used to produce transistors, solar cells, solid state lasers, light emitting diodes (LEDs), and countless other electronic devices and components.

The Method

The transistor in particular has revolutionized the world of information technology by facilitating the design of increasingly powerful computers. One of the requirements for the continuous increase of computer power is that the size of the transistors making up the processing units must be reduced, thereby allowing more transistors to fit onto a single chip. Moore's law, stating that the maximum number of transistors on a given area will double about every two years, has been found to hold true since the sixties until today. The steady miniaturization has continuously presented scientists and engineers with increasingly difficult tasks in both production and characterization of the devices and structures. In both research, development, and production, ever smaller structures must be characterized both in terms of physical attributes such as shape, dimensions, crystal quality, and roughness, and also in terms of electrical properties, *e.g.* conductivity, carrier density, and dominant carrier type.

For macroscopic structures, a plethora of applicable characterization techniques exist. Only very few techniques are, however, suitable for measurements on nanoscale devices. A widely used family of instruments is the *scanning probe microscopes* (SPMs)[1], utilizing an extremely sharp probe which is scanned across an area of the sample while measuring some property of interest at predefined locations. For measuring surface topography, two commonly employed members of the SPM family are the *scanning tunnelling microscope* (STM) and the *atomic force microscope* (AFM), while for electrical characterization techniques such as *scanning capacitance microscopy* (SCM) and *scanning spreading resistance microscopy* (SSRM) may be used.

The Material

It is becoming increasingly obvious that the climate changes observed today are largely caused by human activities, and the Intergovernmental Panel on Climate Change (IPCC) has concluded that urgent action is required if irreversible consequences are to be avoided. In 2010 the parties of the United Nations Framework Convention on Climate Change (UNPCCC) agreed on a long term goal of keeping the global average temperature increase lower than 2°C compared to pre-industrial era levels. It has been found that the global temperature correlates strongly with the emission of greenhouse gases, and to have a 50% chance of meeting this goal the cumulative CO_2 emission caused by humans since 1861 must not exceed 3000 gigatonnes. This is a large number, but by

[1] In scanning probe microscopy, the same acronyms are used when referring to the technique as to the instruments themselves. This should not cause confusion as the context will convey the interpretation in each case.

2011 1890 gigatonnes was already emitted [1]. Also, the energy sector, which stands for two thirds of the annual emission, has produced as much CO_2 in the last 27 years as in all the years before [2].

With the world's ever increasing demand for energy both in developed and developing countries it is evident that something must be done. Part of the solution lies in the ongoing transition from fossil fuels to renewable sources of electricity with wind and solar power currently being the largest contributors. Since its conception in the 1950s the maximum power conversion efficiency of solar cells has increased from about 6% to over 45% [3]. The 45% cells, however, require the use of rare materials and advanced geometries which makes them extremely expensive, hence relevant only for specialized applications such as aerospace and military equipment. The most common solar cells in use today are based on silicon (Si) and have efficiencies of about 15 to 20%. The best silicon laboratory cells reach 25%, while the theoretical maximum is ~ 30 % [4].

To break this limit without significantly increasing cost, it is important that the materials used are abundant and readily available while still providing a high power conversion efficiency. Ideally, the materials should also be environmentally friendly, which disqualifies some popular options used today. A promising material which meets all the above criteria is zinc oxide (ZnO). This can be used either in a so called *tandem cell* where two solar cells are placed on top of each other and connected in series, or alternatively as a transparent conductive oxide which replaces the metal front side contacts on a silicon cell. Other application areas of this material are in display technology and light emitting diodes. In such applications, zinc oxide structures are most often synthesized by thin film processes such as sputter deposition and epitaxial growth, while doping is possible both by diffusion and ion implantation.

The Project

In the Light and Electricity from Novel Semiconductors (LENS) research group at the University of Oslo considerable effort is made to learn as much as possible about zinc oxide and how it can be used in the solar cells of the future.

For any cost effective solar cell, it is important to minimize the consumption of raw materials. A direct implication is that the layers of material making up the cell must be made very thin, and this necessitates the use of advanced characterization techniques. In the work presented in this thesis, SCM and SSRM are used for characterizing the carrier distributions of a range of zinc oxide structures currently under research. These techniques have been systematically employed with great success on silicon (Si) devices, but have seen only sparse use related to specific research issues on oxide semiconductors. Part of the reason is that while the techniques are inherently sensitive to sample topography, no comprehensive study of preparation routines has been made for these materials. Experiments are conducted on sample cross sections, which is significantly more complicated than plan view measurements due to the topography introduced by the cross sectioning procedure. The outcome is that the techniques appear unreliable, indeed sometimes failing to provide useful results altogether. It is expected that a systematic investigation of available preparation procedures will increase both the stability and the number of possible applications of SCM and SSRM in zinc oxide structures.

Hence, the key goal of the presented work is to determine the optimal preparation routines for a range of structures which are subject to ongoing research projects. Specifically, the considered structures can be classified by their synthesis technique as in-diffused-, ion implanted-, and heterostructure samples. As diverse substrate materials are used for these structures, a separate routine will need to be developed for each case. A secondary goal is to investigate whether the two-dimensional electron gas (2DEG) reported in heterostructures of zinc oxide and magnesium zinc oxide alloys can be imaged with either SCM or SSRM after preparation with the developed procedures. To improve the data analysis capabilities over the available commercial software, Matlab scripts will be produced.

Chapter 2

Background

This chapter provides the theoretical background required to appreciate the work presented in this thesis. The chapter is divided into four sections, where the first two establishes the fundamental framework of solid state physics and introduces properties and applications of zinc oxide. The latter two sections covers previous related work, and defines the scope of this thesis.

The treatment of solid state physics is mainly based on the initial three chapters of [5] as well as chapter 3 of [6]. The classical description of semiconductor crystallography is based on chapter 5 of [7] and chapter 2 of [8] while the quantum mechanical description is based upon chapter 1 of [7], chapters 2 and 3 of [5], chapter 3 of [9], and chapter 4 of [10].

2.1 Solid State Physics

All matter consists of atoms and is found in one of the four phases solid, liquid, gas, or plasma. In this work, only solid materials are considered. Due to interactions between the atomic nuclei and their surrounding electrons, the atoms in a solid, unlike in the other phases, occupy fixed positions from which they may move only slightly.

For quantum mechanical reasons explained in section 2.1.3 the electrons of an atom cannot have any arbitrary energy, but are limited to certain discrete values called *atomic orbitals*. Pauli's exclusion principle states that each orbital can accommodate at most two electrons, and atoms with more than two electrons must thus make use of multiple orbitals to accommodate them. The lowest energy orbitals are occupied first and are spatially localized close to the atomic nucleus. Orbitals of higher energy are more spatially extended and the electrons of these orbitals tend to shield the electrons in the lower energy orbitals from interactions with their surroundings. The most extended orbitals occupied by electrons are referred to the *valence* orbitals, while the less extended ones are called *core* orbitals. Since the core orbitals do not react significantly with their surroundings they are in many cases neglected and in this branch of physics the word electrons is commonly used to mean only the valence electrons.

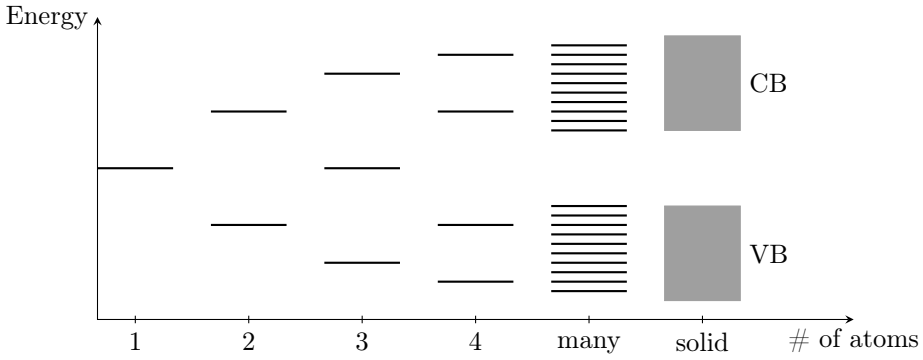

Figure 2.1: *The development from discrete molecular orbitals to energy bands and their distribution in energy space. The valence (VB) and conduction bands (CB) are indicated.*

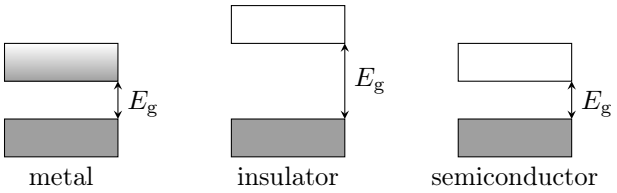

Figure 2.2: *Simplified energy bands and band gaps of a metal, an insulator, and a semiconductor at a temperature of zero Kelvin. In all three cases, the lower band is the valence band while the upper band is the conduction band. In the metal, the conduction band is partially occupied with electrons while in the other two materials it is empty. The valence band is full in all three cases.*

When atoms come in close proximity of each other, their atomic valence orbitals start to overlap and new allowed states called *molecular* orbitals are formed, one for each interacting atomic orbital. Some of the molecular orbitals have energies slightly higher, and others have energies slightly lower, than the original atomic orbitals. When many atoms are brought close together a vast number of such overlapping events occur, resulting in an abundance of molecular orbitals. Their energies are determined by the electronic properties of the atoms which produced them and tend not to distribute evenly, as illustrated in figure 2.1. Some energy ranges may have so many closely spaced molecular orbitals that they form a virtual continuum of allowed energies, which is called an *energy band*. The bands may be separated by ranges of energy where no molecular orbitals exist. The distribution of electrons in the original atomic orbitals determines the distribution of electrons in the bands, and electrons prefer to go into the band with the lowest energy possible. If atoms can lower their energy by letting their electrons occupy bands, they will do so and the atoms thereby bond together. The electrons in a band are no longer considered to belong to any particular atom but rather they all belong to the band. The occupied band of highest energy is called the *valence band* and the empty band of lowest energy is called the *conduction band*. Although gaps exist between many bands, the energy gap between these two bands is referred to as *the* band gap and denoted by E_g. If, at absolute zero, the valence band is partially empty or if the valence and conduction bands overlap, the solid is defined as a metal. Otherwise, if the valence band is completely filled and the conduction band is empty the material is either a semiconductor or an insulator. The main distinction between these two classes of materials is the size of the band gap. Materials of band gap smaller than about 3 eV are defined as semiconductors while those with larger gaps are said to be insulators. This distinction is illustrated in figure 2.2.

As long as the temperature is 0 K, neither insulators nor semiconductors are able to conduct electrical charge. Charge transport requires two conditions to be met, the band must contain at least (i) one electron, and (ii) one free state to which the electron can move. The conduction band cannot transport charge as there are no electrons available, while in the valence band (and all bands of lower energy) all the states are occupied so the electrons have no free states to move into. In insulators, the situation remains largely the same also at finite temperatures and hence they still do not conduct electricity. In the semiconductors on the other hand, some electrons may gather sufficient thermal energy to overcome the band gap. This excites them from the valence band to the conduction band where there is an abundance of free states. Under the influence of an electric field , these electrons are readily displaced and constitute a current flowing through the now conductive material. Additionally, since there are now a few electrons missing in the valence band, the remaining valence electrons can use these empty states to move through the solid. To simplify analysis, it is common to describe conduction through the valence band by the relatively few empty states rather than by the abundant electrons. The empty valence band states are called *holes* and are considered as positive charge carriers. With rising temperatures more and more electrons are able to transition to the conduction band and thus the conductivity of the material increases with temperature.

2.1.1 Basics of Crystallography

Solid materials are often classified by their microstructure as either *monocrystalline*, *polycrystalline*, or *amorphous*. As shown in figure 2.3 their difference lie in the way that the atoms are organized. In the amorphous solids the atoms occupy seemingly random positions and no systematic ordering

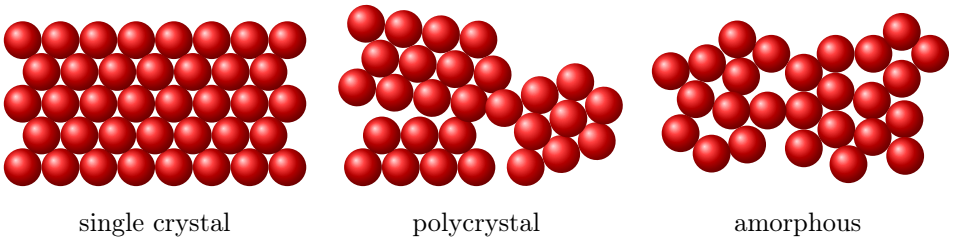

Figure 2.3: *2D representation of the atomic arrangement of a monocrystalline, polycrystalline and an amorphous material.*

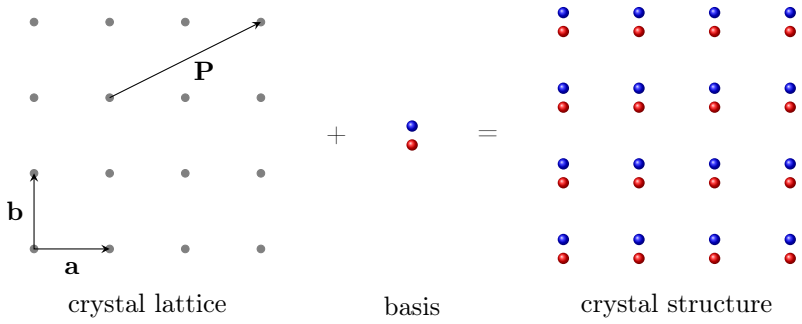

Figure 2.4: *A generic, two-dimensional crystal lattice and basis. The basis vectors* **a** *and* **b**, *as well as the lattice vector* $\mathbf{P}(u = 2, v = 1)$, *are indicated*

can be found. Conversely, the monocrystalline, or single crystal, materials are perfectly ordered and all atoms occupy well defined positions. In between these two extremes lie the polycrystals which consist of randomly oriented "bundles" of well ordered atoms called *grains*, which are separated by *grain boundaries*. If slowly cooled to a sufficiently low temperature, most materials will organize as monocrystalline. The microstructural ordering of its atoms determine many of the physical and chemical properties of a material and a scheme for characterizing the structure has therefore been developed.

Crystal Lattices and Structures

When describing the structure of a crystalline material it is useful to start from a mathematical construction called a *crystal lattice* as illustrated in two dimensions in figure 2.4. This is an infinite array of points in space with the property that in any given direction, each point is equidistant. Also, all points of the lattice are equivalent, meaning that they have exactly the same surroundings. Starting from an arbitrary lattice point, any other lattice point in a three dimensional lattice is defined by the relation

$$\mathbf{P}(u, v, w) = u\mathbf{a} + v\mathbf{b} + w\mathbf{c},$$

where **a**, **b**, and **c** are called the *basis vectors* and u, v, and w are any positive or negative integers. The crystal lattice is thus defined by the magnitudes of the basis vectors (a, b, and c) as well as the angles between them, α, β, and γ. Here α is defined as the angle between **b** and **c**, β is the angle between **a** and **c**, and γ is the angle between **a** and **b**.

To develop the mathematical idea of a lattice into a description of a real crystal structure, a single atom, a group of atoms, or a molecule is assigned to each lattice point. The assigned species is called the *basis* of the structure and, as all the lattice points are equivalent, the same species is assigned to all points. Hence, given its lattice and basis, one can construct the entire structure of any crystalline material, as shown in figure 2.4.

The volume of space spanned by the basis vectors is called the *unit cell*[1]. In three dimensions all unit cells have eight vertices and six faces, and lattice points can be located at the vertices, at the centre of each face, and/or at the body centre of the unit cell. The smallest possible unit cell (given by the shortest possible lattice vectors) is called the *primitive* cell, and is characterized

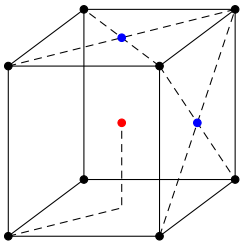

Figure 2.5: *A cubic unit cell with lattice points for a primitive cell (black), a body centered cell (black and red) and a face centered cell (black and blue). Note that the face centered cell can have lattice points on some, or all faces. For clarity only two points are shown.*

by having no lattice points except one at each vertex. Other common unit cells include the *body centered*, and *face centered* cells, as shown in figure 2.5.

Miller Indices

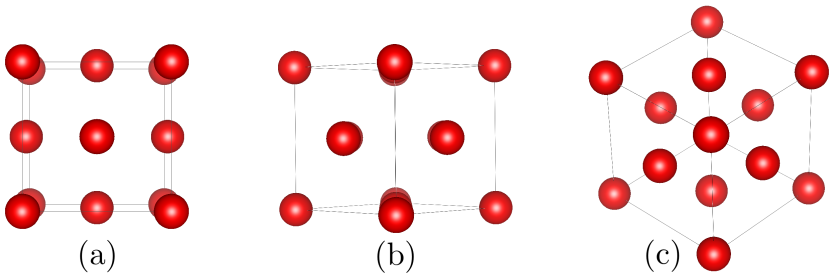

Figure 2.6: *A face centred cubic unit cell seen in the* [1 0 0] *direction (a), the* [1 1 0] *direction (b), and in the* [1 1 1] *direction (c). The figures were produced using the VESTA software [11].*

By looking at the unit cell of a crystalline material it can be seen that the cell appears exactly identical in terms of atomic arrangement and density from several viewing angles. Other angles might show different densities, as illustrated in figure 2.6. The varying atomic density gives the material different chemical and physical properties in the different directions, and the crystal is said to be *anisotropic*.

Due to this anisotropy it is important to be able to discuss individual planes and directions in the crystalline materials, and these are defined by the so called *Miller indices*. A plane in a crystal is given as a triplet of numbers enclosed in parentheses, *e.g.* (1 2 3) or more generally $(h\,k\,l)$, where the n-th index is the reciprocal of the intersection of the plane in question with the n-th basis vector. Negative indices are denoted by a bar above the index in question.

A direction in a crystal is defined in terms of a vector. The vector components are expressed as multiples of the basis vectors of the lattice, and are given as the smallest set of integers with the desired proportions, enclosed in square brackets. For instance, the body diagonal of a cubic crystal is given as [1 1 1].

For hexagonal structures, crystallographically equivalent planes may be hard to identify based on their Miller indices. To better convey their equivalence, a fourth index is introduced so that the general index becomes $(h\,k\,i\,l)$. This system of indexing is known as *Miller-Bravais* indexing and by definition $i \equiv -(h+k)$. In an analogous way, directions in hexagonal crystals may also be given by four indices.

Defects

All crystalline materials have some finite concentration of defects and impurities which manifest in a number of forms. Defects are commonly distinguished by their spatial extension as point, line,

[1] It should be noted that the basis vectors, and thereby the unit cell, are not uniquely defined. A variety of vector combinations and unit cells can be created to describe a given lattice. By convention, the preferred lattice vectors are small in magnitude and reveal the symmetry of the lattice.

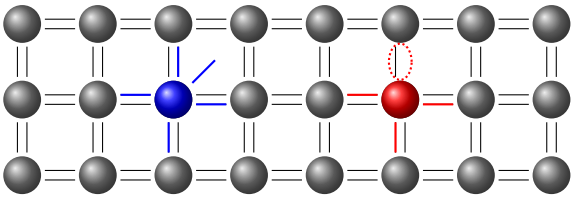

Figure 2.7: *A donor (blue) and an acceptor (red) dopant and their bonds to the neighbouring atoms. Compared to the lattice atoms the donor has an extra electron which does not take part in a bond, while the acceptor atom lacks one electron thereby leaving one unsatisfied bond.*

area, or volume defects. Only defects of the former type, which are localized at discrete points in the structure, are considered here. The other cases extend in 1, 2, and 3 spatial directions, respectively. In an elemental material without impurities the possible point defects are the *vacancy*, the *self-interstitial*, and complexes thereof. A vacancy is a lattice site without an associated atom, while a self-interstitial is a lattice atom located at a position which is not a lattice site. These can form simultaneously if an atom is, by some means, ejected from its lattice site. When this happens, the ejected atom may bring all its valence electrons, resulting in an electrically neutral vacancy and interstitial. Alternatively, the ejected atom might leave one or more of its valence electrons behind to complete the valences of the atoms it was formerly bonded to. In this case, the vacancy is said to have a negative charge, while the interstitial has an equal but opposite positive charge. In compound materials, a third kind of intrinsic point defect called the *antisite* may occur. This is a situation where an atom of one element occupies a lattice site associated with another element.

The inevitable incorporation of impurity atoms introduces two additional point defects, namely the *substitutional* and *interstitial* impurity. The former is an atom of a foreign element which occupies a lattice site while the latter, as the name suggests, is a foreign atom on an interstitial site. These defects readily change the electronic properties of a material, as explained in the next section.

2.1.2 Doping and Alloying

Doping

Doping refers to the intentional introduction of atoms of a foreign element into the crystal structure of a semiconductor. If the impurities have more electrons than the lattice atoms, the additional electrons will not participate in chemical bonds and will only be weakly bound to their nuclei by electrostatic attraction. Such electrons are easily liberated from their parent atom and excited to the conduction band by thermal or optical means. These kinds of impurities are known as *donors*, as electrons are donated to the conduction band.

The second class of dopant atoms, called *acceptors*, consist of elements with fewer electrons than the atoms of the host crystal. Their electron deficiency means that they cannot successfully bond to all their neighbouring atoms, so they tend to capture electrons from the conduction band or nearby valence electrons in order to satisfy all their bonds. This process is equivalent to the donation of a hole. A semiconductor which has been doped with donors is referred to as an n-type semiconductor, while one doped with acceptors is referred to as p-type. An illustration of acceptor and donor doping is given in figure 2.7

The commonly used dopant elements are recognized by readily accepting or donating electrons at room temperature. Other impurity atoms may have a higher activation energy and remain electrically inactive unless temperature is increased or energy is otherwise provided.

Alloying

For certain material combinations it is possible to introduce one semiconductor element into the crystal structure of a different semiconductor to form an alloy. This differs from doping in two ways, (i) in alloying the introduced semiconductor typically makes up some percent of the total structure while typical dopant concentrations are of the order of parts per million. (ii) Doping is done to control the concentration of electrons and holes while alloying is done to alter the size of the band gap.

Alloying a given material with one of larger band gap will normally increase the band gap of the compound proportionally with the concentration of the introduced species. Alloying with a material of smaller band gap has the opposite effect. In either case successful alloying requires that the two materials have similar lattice parameters and crystal structure, else an unacceptable concentration of crystal defects will result. For zinc oxide, alloys are commonly formed with magnesium oxide (MgO) or cadmium oxide (CdO). Alloying of two materials influences the band structure of the compound, and alloying a direct band gap semiconductor with an excessive concentration of a second material may turn it into an indirect band gap semiconductor.

2.1.3 Quantum Mechanics of Crystalline Materials

From a quantum mechanical perspective, the electron may be described as a wave of wavelength

$$\boldsymbol{\lambda} = \frac{h}{\boldsymbol{p}}, \tag{2.1}$$

where $\boldsymbol{p}$ is its momentum and $h = 4.136 \times 10^{-15}\,\mathrm{eV\,s}$ is Planck's constant. The electron wave obeys the Schrödinger equation,

$$-\frac{\hbar^2}{2m}\nabla^2\psi + V\psi = E\psi \tag{2.2}$$

which can be solved to find the allowed *states*, ψ, of the electron. The remaining terms of the equation are, $\hbar = h/2\pi$, m is the mass of the electron, ∇^2 is the Laplacian operator, V is the potential (periodic, in case of a crystalline material), and E is the eigenvalues of the total energy of the system. For all but the simplest of potentials, the Schrödinger equation is impossible to solve. It is therefore common to let $V = 0$, and account for the effect of the potential by replacing the mass, m, with an *effective mass*, m^* given by

$$m^* = \frac{\hbar^2}{d^2E/d\boldsymbol{k}^2}. \tag{2.3}$$

For isolated atoms the allowed states are the atomic orbitals, each with its own discrete energy. For an electron in a solid, the energy levels of the allowed states cluster into broader energy bands whose origin was discussed earlier from a chemical point of view. From a physical perspective, the bands and gaps arise due to diffraction between the individual electron waves.

Electrons in a solid are influenced by the periodic potential provided by the atomic nuclei. According to *Bloch's theorem* the states of these electrons are given by

$$\psi(\boldsymbol{r}) = e^{i\boldsymbol{k}\cdot\boldsymbol{r}}u(\boldsymbol{r}) \tag{2.4}$$

where $\boldsymbol{r}$ gives the positions of the atoms in the solid, i is the imaginary unit, $u(\boldsymbol{r})$ is a periodic function with the same periodicity as the atoms, and $\boldsymbol{k}$ is the wave vector of each electron wave, defined as

$$\boldsymbol{k} = \frac{2\pi}{\boldsymbol{\lambda}}. \tag{2.5}$$

By adopting the Born-von Karman (continuous) boundary conditions, and demanding that the electrons of a solid cannot exist outside the material, the longest possible wavelength of an electron in any direction is equal to the length of the solid, L, in this direction. Thus,

$$\psi(\boldsymbol{r}) = \psi(\boldsymbol{r} + \boldsymbol{L}), \tag{2.6}$$

where $\boldsymbol{L}$ gives the dimensions of the solid in the three spatial dimensions. This implies that $e^{i\boldsymbol{k}\cdot\boldsymbol{r}}$ must be equal to $e^{i\boldsymbol{k}\cdot(\boldsymbol{r}+\boldsymbol{L})}$, and for this to hold in general it is required that

$$\boldsymbol{k} = \frac{2\pi}{\boldsymbol{L}}\boldsymbol{n}, \tag{2.7}$$

where $\boldsymbol{n} = an_x + bn_y + cn_z$ with n_x, n_y, and n_z being unit vectors in the directions of the basis vectors and a, b, and c can take any integer value.

Combining (2.5) with (2.1) gives

$$\boldsymbol{k} = \frac{2\pi\boldsymbol{p}}{h} = \frac{\boldsymbol{p}}{\hbar}. \tag{2.8}$$

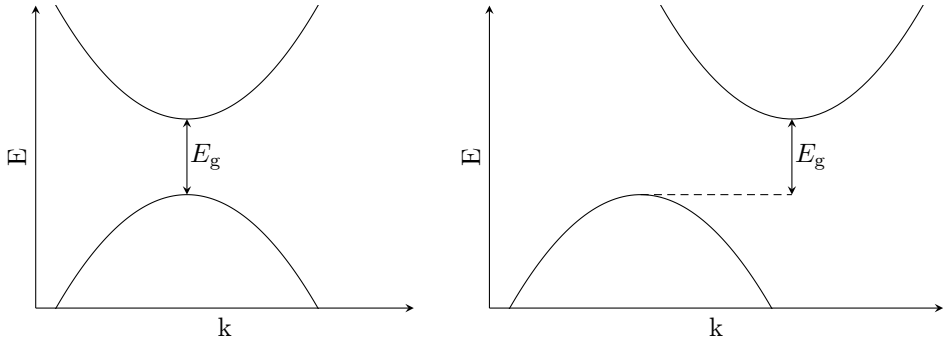

Figure 2.8: *Simplified, one-dimensional band structures of a direct (left), and an indirect (right), band gap material. For clarity only the valence and conduction bands are shown.*

The kinetic energy of a free electron can be given by the classical expression $\boldsymbol{E} = \boldsymbol{p}^2/2m^*$ where m^* is the effective electron mass. Solving this for $\boldsymbol{p}$ and inserting into (2.8) leads to the expression

$$\boldsymbol{E} = \frac{\hbar \boldsymbol{k}^2}{2m^*}, \tag{2.9}$$

which shows that the electron energy is a function of its wave vector. To simplify calculations $\boldsymbol{k}$ can be represented in the so called *reciprocal space* (also called k-space). This is a mathematical space related to the "real" space lattice of the crystal in that the lengths of the reciprocal lattice vectors are inversely proportional to the lengths of the basis vectors. Each value of $\boldsymbol{k}$ thus corresponds to a position in reciprocal space, and the allowed values of $\boldsymbol{k}$ can be determined from the reciprocal lattice vectors.

A plot of the electron energy as a function of wave vector (Equation (2.9)) is called the *band structure* of the solid and provides important information about the optical and electronic properties of a material. One of the properties which can be determined from such a plot is whether the material has a direct or indirect band gap. Simplified one-dimensional $E(\boldsymbol{k})$-diagrams for these two cases are shown in figure 2.8. For each of the cases only the valence and conduction bands are shown. In a direct band gap material, the energy minimum of the conduction band occurs at the same value of $\boldsymbol{k}$ as the valence band maximum, whereas in an indirect band gap material, the extrema occur at different values of $\boldsymbol{k}$.

If an electron receives or dissipates sufficient energy it may transition from one state to another. These transitions require that there exists an empty state with the "correct" energy which the electron can move into. Energy is absorbed and emitted by electron-electron interactions, electron-nucleus interactions, or as quanta of electromagnetic radiation called photons. Jumps across the band gap may occur if an electron can gather the required energy.

Since electrons prefer to occupy the lowest available energy states they tend to accumulate close to the bottom of the conduction band. For the same reason, any vacant states in the valence band are found close to the maximum, since a vacant state of lower energy is quickly filled with a higher energy electron. Therefore, electrons transitioning from the conduction band to the valence band are generally located very close to the conduction band minimum, and they move to a state close to the valence band maximum. For this to happen, not only does the energy of the electron decrease, but depending on the locations of the valence band maximum and conduction band minimum, its value of $\boldsymbol{k}$ might also need to change. Changes in E are readily taken care of by emission or absorption of photons, but these have very little momentum and, by (2.8), do not significantly influence k. Instead, the momentum change required for interband transitions in indirect band gap semiconductors is facilitated by interactions with modes of lattice vibrations (phonons) resulting in heating of the crystal. In direct band gap materials, no change of $\boldsymbol{k}$ is required, which implies that an electron can maintain its momentum while jumping between the bands. Consequently no energy is lost as heat to the material and this is a great advantage in materials intended for use in photovoltaic applications. When an electron jumps from the valence band to the conduction band, the electron and the hole it leaves behind in the valence band are collectively referred to as an *electron hole pair* (EHP).

2.1.4 Density of States and Electron Occupancy

Many physical and chemical properties of a material are related to its electron density. Indeed, the first *Hohenberg-Kohn theorem* of density functional theory (DFT) states that *any* property of a system can be deduced from its ground-state electron density [9, p. 11]. Determining the density of electrons in a solid requires knowledge of both the density of states (DOS) and the occupation probability.

The DOS is a function giving the number of allowed states in the energy range E to $E+dE$ per unit volume, while the occupation probability function, as the name suggests, gives the probability of occupation of any of these states. For a three-dimensional structure, the density of states as a function of energy is commonly given as

$$d_{3\mathrm{D}}(E) = \frac{1}{2\pi^2}\left(\frac{2m^*}{\hbar^2}\right)^{3/2}\sqrt{E} \tag{2.10}$$

where the symbols have all been defined earlier [10, p. 27].

The occupation probability is found from the fact that electrons in a solid follow the Fermi-Dirac function

$$f(E) = \frac{1}{e^{(E-E_{\mathrm{F}})/kT}+1}. \tag{2.11}$$

Here, E is the energy of an electron, E_{F} is the *Fermi level*, k is Boltzmanns constant, and T is the absolute temperature [5, p. 87]. $f(E)$ then gives the probability that a state of energy E will be occupied by an electron given a temperature T. It follows that the Fermi level is the energy at which the occupation probability is 50%. This implies that an n-type semiconductor will have a Fermi level close to the conduction band, while a p-type semiconductor will have the Fermi level close to the valence band. Intrinsic semiconductors typically have Fermi levels close to the centre of the band gap. If a junction is formed between two materials of different Fermi levels, electrons and holes will diffuse between the materials until the Fermi level is constant throughout under thermal equilibrium.

The electron and hole concentrations in a band can now be calculated by

$$n = \int_E d_{3\mathrm{D}}(E) f(E)\, dE \tag{2.12}$$

$$p = \int_E d_{3\mathrm{D}}(E)\left(1-f(E)\right)\, dE \tag{2.13}$$

where the integrals are taken over the energy range of interest, typically the conduction band for electrons and the valence band for holes.

From the charge carrier densities it is possible to calculate the *conductivity*, σ (and its inverse, the *resistivity*, ρ) by

$$\sigma = q(\mu_{\mathrm{n}} n + \mu_{\mathrm{p}} p) \tag{2.14}$$

$$\rho = \frac{1}{\sigma} \tag{2.15}$$

where q is the electron charge, and μ_{n} and μ_{p} are the *mobilities* of electrons and holes, respectively. The mobility is a material property which measures of how easily a charge carrier may move through the material in question.

2.1.5 Quantum Confinement and the Two-Dimensional Electron Gas

In bulk samples electrons are typically free to move in all directions, but certain sample configurations can limit their degrees of freedom. If electron motion is restricted in one spatial direction while unrestricted in the other two, the electrons are said to be *confined* in this direction. Due to the confinement, which is quantum mechanical in nature, the electrons can no longer take any energy but are restricted to discrete levels in the confined direction. If only the ground state is available, the electrons form a *two-dimensional electron gas* (2DEG). If more than one level is available, they have some freedom to move in the confined direction and are said to form a *quasi*-2DEG [12, p. 173].

The reasons for the interest in the two-dimensional electron gases are the severely enhanced current transport properties and the increased recombination efficiency of the 2DEG compared

to the free electron gas [13]. This can be utilized in creating high electron mobility transistors (HEMTs) as well as in spintronic circuits [14]. Also, due to the discrete electron energy levels, the presence of a 2DEG can influence the optical absorption and emission spectra of a material [15].

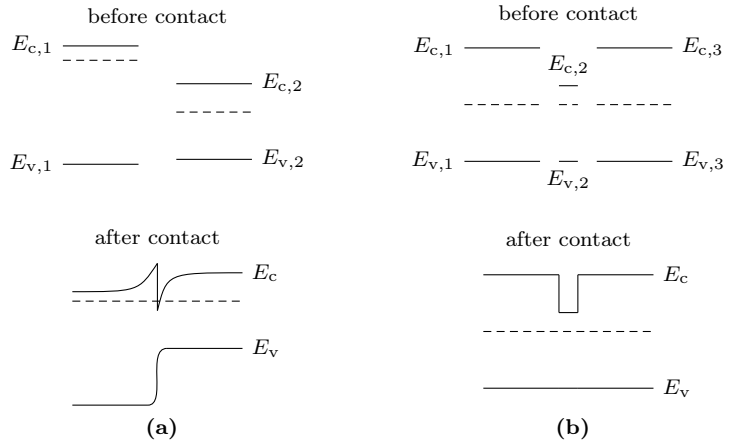

Figure 2.9: *Energies of the conduction band minimum (E_c) and valence band maximum (E_v) of a heterostructure (a) and a quantum well (b) before and after the materials come into contact. The dashed lines represent the Fermi level, E_F, in each case.*

Confinement occurs if electrons can be trapped in a narrow potential well, which may be created in for instance a semiconductor heterostructure or a quantum well structure. The heterostructure is nothing but a junction between two dissimilar materials, generally with different values of E_{F}, χ[2], and E_{g}. As electrons diffuse between the materials in order to equalize the Fermi levels, the valence and conduction bands must bend. Due to the discontinuities in E_{c} and E_{v} caused by the different χ and E_{g} of the two materials, the band bending may lead to the formation of a triangular potential well in the conduction band of one material. This is illustrated in figure 2.9a. Such wells are very narrow (on the order of nanometers), thus electron motion perpendicular to the well is severely restricted. If a well is formed in the valence band rather than the conduction band, a two dimensional *hole* gas may occur.

A quantum well is a structure where a material of smaller band gap is introduced between two layers of a material with a higher band gap as shown in figure 2.9b. If the smaller band gap material is made sufficiently thin, the allowed states here will have discrete, well separated energies. Electrons in these states will have little or no freedom to move perpendicularly to the well, thus constituting a 2DEG.

The origin of the electrons in a 2DEG depends on the specifics of the system. Causes such as differences in Fermi level, application of an external electric field, doping, polarized charges, or donor-like interface states are all common.

2.1.6 Metal-Semiconductor Contacts

The properties of contacts between metals and semiconductors are widely studied due to the importance in the electronics/integrated-circuit industry where metal conductors are used as interconnects between the individual devices on a chip. Depending on the choice of metal and doping of the semiconductor, either an Ohmic- or a Schottky contact is formed.

The Ohmic contact is the type most often wanted for device contacting, and is characterized by providing an equal electrical resistance to current flow in either direction. The Schottky contact on the other hand provides a higher resistance to current in one direction than the other, resulting in a rectifying effect.

[2]The *electron affinity*, χ, is the amount of energy required to remove an electron from the conduction band of a semiconductor.

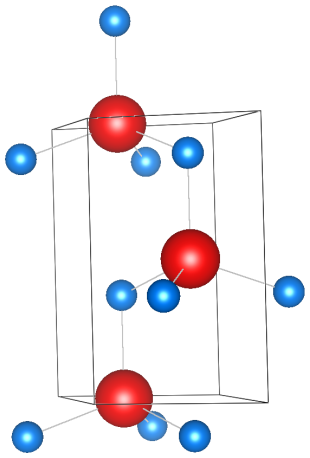

Figure 2.10: *The unit cell of the wurtzite structure of zinc oxide. Here, the large, red atoms are Zn and the small, blue ones are O. The figure was made with VESTA [11].*

2.2 Zinc Oxide

This section is mainly based on the 2005 review article of Özgür *et al.* [16].

Zinc oxide (ZnO) is a II-VI compound semiconductor first studied in the 1930s. Nowadays the material has found uses as diverse as increasing the thermal conductivity of rubber, absorbing UV radiation in textiles and sunscreens, providing dietary zinc in food products, preventing growth of moulds and fungi in food packaging, as well as a vast variety of other applications [17]. In this work however, the electronic applications of ZnO are the ones of interest, including the use as a closely lattice matched substrate for gallium nitride (GaN) devices, thin film transistors, ultraviolet (UV) and blue light emitters, and transparent conductive oxides (TCOs) in solar cell panels. The advantages of ZnO over comparable materials include low cost, abundance of raw materials, and environmental friendlyness [18]. The key factor limiting its use in electronic applications is the lack of a process to produce p-type material, which prevents the production of pure-ZnO p-n junctions, and consequently diodes and transistors. This can to some degree be circumvented by growing n-type ZnO on a p-type substrate of a different material, but this is not a fully satisfactory solution and considerable research has been, and is currently being, conducted on this topic [19, 20].

Zinc oxide is a crystalline material, which may take the rock salt (NaCl), zinc blende, or wurtzite structures. At standard atmospheric conditions the latter is the stable form, and is illustrated in figure 2.10. Each atom is bound to four others, and the bonds point towards the vertices of a tetrahedron. The bonding character is predominantly covalent, but also has a strong ionic contribution. The structure can be regarded as two interpenetrating hexagonal close-packed (HCP) lattices, one consisting purely of zinc atoms while the other consists of oxygen atoms. The sublattices are displaced with respect to each other in the $\boldsymbol{c}$ direction by $3\boldsymbol{c}/8$. The structure is thus not symmetric in this direction and is said to be crystallographically polar. An implication of this is that the $(0\,0\,0\,1)$ plane of a ZnO crystal is different from the $(0\,0\,0\,\bar{1})$ plane. By convention, the $[0\,0\,0\,1]$ direction is the positive z-direction and points from an oxygen plane towards a zinc plane.

Due to the differing bonding arrangements of the Zn-face and the O-face, many properties of the crystal depend on the termination of the surface. Through curve-fitting of experimental results Li *et al.* [21] have numerically shown that the density of 2DEG electrons with respect to the density of background electrons in ZnO-based heterostructures is strongly dependent on the polarity.

The reported lattice constants varies slightly between different sources, but are typically stated to be around $a = 3.25\,\text{Å}$ and $c = 5.12\,\text{Å}$ [22]. The material is available in bulk form, and high quality single crystalline thin films can be grown by molecular beam epitaxy (MBE), pulsed laser deposition (PLD), metal-organic chemical vapour deposition (MOCVD) as well as other techniques. Polycrystalline films can be deposited by sputtering. Although poorly matched both in terms of thermal expansion and lattice parameters, sapphire (Al_2O_3) is the most commonly used substrate material for thin film growth. This is due to low cost and the availability of large, high quality

wafers. Zinc oxide wafers are also commercially available, allowing for homoepitaxial growth.

In terms of electronic properties, zinc oxide is classified as a wide band gap semiconductor, with a direct band gap of $E_g = 3.3\,\text{eV}$ and an exciton binding energy of $\sim 60\,\text{meV}$. The high band gap provides a high break-down electric field strength, as well as the possibility of high-temperature and high-power operation. At room temperature, the mobility of bulk ZnO has been measured to $\mu_{\text{bulk}} > 200\,\text{cm}^2/\text{Vs}$ while the carrier concentration has been found to be in the region of $n = 5 \times 10^{16} - -5 \times 10^{17}\,\text{cm}^{-3}$ [23]. Epitaxial films can be grown with a similar carrier concentration but unfortunately do not match this mobility, and the highest reported value in [16] is $\mu_{\text{film}} = 155\,\text{cm}^2/\text{Vs}$ when grown by PLD on a sapphire substrate. It turns out that nominally undoped ZnO shows n-type behaviour. The reason is debated, and Zn-on-O antisites, Zn interstitials, O vacancies, and incorporation of hydrogen acting as a donor have all been proposed as likely causes. In a recent paper Feng *et al.* have found indications that unintentionally introduced hydrogen along with agglomorated zinc interstitials and oxygen vacancies *together* may be the cause of the n-type conductivity [24].

The band gap of zinc oxide can be tuned by alloying with suitable materials. If a wider band gap is desired, magnesium oxide (MgO) with a band gap of 7.7 eV can be incorporated in the ZnO structure up to at least 36%. It has been found that the band gap of the $\text{Mg}_x\text{Zn}_{1-x}\text{O}$ compound increases linearly with x to a maximum of 4.15 eV at $x = 0.36$ where it saturates due to further MgO segregating into a separate phase according to [16]. In a more recent paper, however, Tampo *et al.* claims to have achieved incorporation of as much as 61% MgO in the ZnO structure without segregation.

If a narrower gap is sought, an alloy can be made with cadmium oxide (CdO) which has a band gap of 2.3 eV. Up to 7% CdO can be incorporated in the ZnO structure before segregation occurs, at which point the band gap of the compound is reduced to 2.99 eV.

2.3 Previous Work

The following sections present previous work done on related materials, and with the same techniques as is used in this thesis.

2.3.1 ZnO Thin Film Structures

To understand the behaviour of impurities in zinc oxide, numerous experiments have been performed where a film of doped ZnO is deposited on top of hydrothermally grown commercial ZnO substrates and consequently annealed at various temperatures. The concentration profile of the impurities of interest is measured, typically by secondary ion mass spectrometry (SIMS), after each annealing step, and the results are compared to reveal how the impurities diffuse into the substrate.

In [25] Vines *et al.* found severe differences between the diffusion behaviour of different impurity species. While the lightest elements such as hydrogen and lithium diffuse rapidly at around 600°C heavier elements like Al and Mg have too low diffusivities, even at 1000°C, for annealing to be a useful purifying technique. In [26] it is found that yet heavier elements like Fe, Mn, and Ni, do not diffuse out of the material even at 1500°C.

Although aluminium is one of the most important shallow donors for zinc oxide its diffusion mechanisms have not been extensively studied until recently. In 2015 Johansen *et al.* [27] determined through modelling and experiment that Al on oxygen- or interstitial sites have too high formation energies to exist in significant concentrations. Substitutional aluminium on zinc sites was found to be a common configuration but with very low diffusivity, and it was determined that diffusion mainly takes place as complexes of interstitial aluminium and zinc vacancies (Al_{Zn}-v_{Zn}).

Impurity migration in ZnO has also been studied by a number of groups through ion implantation and subsequent characterization (again typically by SIMS) after post implantation annealing. By this procedure Johansen *et al.* has discovered that hydrogen does not diffuse significantly at temperatures below 300°C. By comparison of the obtained diffusion profiles with various theoretical models it was concluded that hydrogen migrates through a trap limited process [28]. Chan *et al.* have also studied hydrogen migration, and by the observation that the implantation peak narrows after annealing they deduced that the hydrogen concentration is bound to immobile complexes which dissociate upon heating [29].

Table 2.1: *Comparison of the mentioned ZnO 2DEG transistors and the GaAs HEMT. μ_H is the Hall mobility and n is the electron concentration in the channel region.*

Technology	HEMT	HFET	MISFET	GaAs HEMT [39]
μ_{H} [$\mathrm{cm}^2/\mathrm{Vs}$]	130	230	180	$2.7\text{–}5.9 \times 10^3$
n [cm^{-2}]	6×10^{12}	10^{13}	1.2×10^{13}	$1.2\text{–}2.3 \times 10^{12}$

In 2013 Neuvonen *et al.* discovered through self-ion implantation that the redistribution of native lithium after annealing was strongly correlated with which sublattice the atoms were implanted onto [30]. This result was used by Azarov *et al.* to determine the preferred sublattice for a range of relevant atoms, such as magnesium, cadmium, antimony, and others [31]. The correlation between ion beam induced lattice damage and the implanted element has also been investigated. It has been found that annealing after implantation of lighter elements (O, B, Zn) causes a gradual repairing of the crystal. Some of the heavier atoms (Cd, Au, Bi) show a two-stage repair progress, where smaller defects are removed at $\sim 500°\mathrm{C}$ while larger defects require higher temperatures. An exceptional behaviour has been found in samples implanted with nitrogen. These samples have shown a reverse annealing behaviour where the lattice damage increases with post implantation annealing temperature [32].

Several authors [13, 33–35] have reported the formation of a two dimensional electron gas in zinc oxide based structures. The realization of this phenomenon in ZnO has attracted significant research interest as it can be used for creating high electron mobility transistors from an abundant, affordable, and transparent material. In particular, heterostructures and quantum wells of ZnO and magnesium zinc oxide ($\mathrm{Mg}_x\mathrm{Zn}_{1-x}\mathrm{O}$) produced by pulsed laser deposition (PLD) [13], molecular beam epitaxy (MBE) [33, 34] or metal-organic vapour phase epitaxy (MOVPE) [35] have been widely investigated. Polarization charges at the ZnO/MgZnO interface has been pointed out as a likely source of the 2DEG electrons, and a donor concentration of $9 \times 10^{18}\,\mathrm{cm}^{-3}$ has been predicted by self consistent calculations and fit experimental data for nominally undoped MgZnO [33].

Tampo *et al.* [34] have proven a 2DEG in epitaxially grown ZnO/MgZnO heterostructures, and have achieved growth of single-phase wurtzite $\mathrm{Mg}_x\mathrm{Zn}_{1-x}\mathrm{O}$ with x as high as 0.61. They found that the sheet carrier concentration increased linearily with x, up to a value of $1.1 \times 10^{13}\,\mathrm{cm}^{-2}$ at $x = 0.61$. Correlation of this linearity with the results of first-principles calculations support the findings in [33] that the origin of the 2DEG is the polarization effects in the structure. The room temperature mobility was found to increase with x, reaching a maximum of $319\,\mathrm{cm}^2/\mathrm{Vs}$ at $x = 0.61$. From measurements of the sheet carrier density as a function of MgZnO layer thickness it is concluded that the source of the electrons of the 2DEG lies in the *interface* of the layers rather than the bulk of the MgZnO layer. It has however been found that a critical thickness exists for the MgZnO layer, below which a 2DEG will not form. This thickness is dependent on the Mg concentration and has been determined to 38 nm for $x = 0.05$ and 1 nm for $x = 0.45$ [35]. The same paper suggests oxygen vacancies at the ZnO/MgZnO interface as a likely candidate for the mobile electrons in the 2DEG.

In the papers mentioned, the structures have been examined with capacitance-voltage (CV) spectroscopy, temperature dependent Hall effect measurements, and photoluminescence (PL) spectroscopy which are all macroscopic techniques. No reports have however been found on microscopic investigations of the electrical properties of such structures in ZnO.

In terms of applications, Koike *et al.* has realized high electron mobility transistors (HEMTs) in MgZnO/ZnO/MgZnO quantum wells [36], and pH sensitive heterojunction field effect transistors (HFETs) intended for biosensing in single heterostructures [37]. The same group has also produced a heterojunction metal insulator semiconductor FET (MISFET) with a room temperature channel mobility of $180\,\mathrm{cm}^2\,\mathrm{V}^{-1}\,\mathrm{s}^{-1}$ and an electron sheet density of $1.2\,\mathrm{cm}^{-2}$ with an $\mathrm{Al}_2\mathrm{O}_3$ dielectric [38]. In Table 2.1 the mobilities and sheet carrier concentrations of these ZnO transistors are summarized and compared to a gallium arsenide HEMT. Although the GaAs is superior in terms of both these parameters, the lower cost, and transparency to visible light implies that ZnO transistors may still be commercialized in the future.

2.3.2 Scanning Spreading Resistance Microscopy

Scanning spreading resistance microscopy (SSRM) and scanning capacitance microscopy (SCM) are both scanning probe techniques which have been utilized to investigate carrier distributions on the micro- and nanoscale.

Though developed for silicon based devices, SSRM has also been employed on various other semiconductor materials such as silicon carbide, indium phosphide, and gallium nitride. For indium phosphide (InP) it has been found that SSRM requires significantly reduced sample preparation compared to silicon. The tip-sample force can also be reduced, enabling the utilization of metal probe tips on silicon cantilevers. It is however found that a satisfactory signal-to-noise ratio requires bias voltages on the order of volts, rather than millivolts as for Si. Application of the technique to a n- and p-doped InP test structure has shown that dopant layers of width down to 50 nm can be resolved and that the sensitivity is on the order of 15 nA per $10^{17}\,\mathrm{cm}^{-3}$ [40]. From SSRM experiments on optoelectronic InP structures grown by metal-organic vapour phase epitaxy a resolution of 10 nm has been achieved with boron doped diamond probe tips. Single quantum wells have been resolved, and layer thicknesses show good correlation with complementary SIMS measurements. It has also been observed that the current in p-type InP increases faster with voltage than the current in n-type InP for bias voltages in the range 0.5–2 V [41].

Aluminium dopants (p-type) in the 4H polytype of silicon carbide have been detected at concentrations in the range 2×10^{16}–$2 \times 10^{20}\,\mathrm{cm}^{-3}$ and correlated with SIMS profiles. It has been found that the bias must be above 3 V for stable contact, but the force can be as low as a few µN. Due to the hardness of the material, doped diamond probes are required to avoid unacceptable degradation [42].

Scanning spreading resistance microscopy has seen very little use on zinc oxide but a few reports do exist in the literature. One of the earliest is by Monakhov *et al.* who used the technique to investigate the electrical activity of hydrogen implanted ZnO after various stages of annealing [43]. Johansen *et al.* studied the same material a few years later, and also compared two different materials for back side contacting of the sample to the microscope stage [44].

In the article by Neuvonen *et al.* [30] mentioned previously SSRM was used in combination with SIMS to determine the charge polarity of substitutional and interstitial lithium. Børseth *et al.* used the technique in combination with SCM to characterize the applicability of Al (donor) and Sb (acceptor) as dopant species for ZnO. It was then found that aluminium doping produced well conducting n-type material while antimony did not cause stable p-type material. Instead electrical compensation effects were observed.

2.3.3 Scanning Capacitance Microscopy

Although initially developed for topographical analysis of RCA's SelectaVision capacitance electronic discs, scanning capacitance microscopy has been put to more use in characterizing the carrier concentration in semiconductor structures [45, 46]. Not surprisingly, silicon has been the most widely studied material, but in later years it has been demonstrated that the technique is also applicable to other semiconductors. Anand *et al.* has demonstrated the ability of SCM to detect buried metal wires and to delineate pn-junctions in gallium indium phosphide (GaInP) [47]. In the work by Brezna *et al.* an important issue was brought up. During scanning capacitance microscopy of silicon samples damaged by a focused ion beam they found that heavily damaged regions produce a low dC/dV signal which cannot be distinguished from an area of high carrier concentration [48].

The III-V compounds gallium nitride (GaN), indium phosphide (InP), and indium gallium arsenide (InGaAs) have been studied by Lamhamdi *et al.* [49] and Douhéret *et al.* [50], respectively. They demonstrate that SCM is applicable for all these materials, and particularly that 5 nm wide InGaAs quantum wells separated by n-type InP barriers can be successfully detected.

In the quest to produce stable p-type zinc oxide, Krtschil *et al.* [51] co-doped a ZnO film with nitrogen and arsenic during deposition with MOCVD. In a subsequent SCM experiment, they utilized the capability of simultaneously capturing topography and capacitance data to correlate the grown n- and p-type regions with the film growth mode. It was found that under conditions which produced flat films, large areas were in fact p-type, only separated by cracks or particles in the film. In contrast, samples grown under conditions which led to three-dimensional particles showed a mixed conductivity where the particles were n-type and flatter regions between particles were p-type.

In a recent paper Wang *et al.* [52] report successful discrimination of n-doped regions with carrier concentrations on the order of 10^{17}–$10^{20}\,\mathrm{cm}^{-3}$ in zinc oxide. The structures were grown homoepitaxially by molecular beam evaporation and received no particular preparation apart from manual cleaving to access the cross section. A spatial resolution of 20 nm was achieved, and the SCM results were found to qualitatively correlate well with doping densities found by secondary ion mass spectrometry.

2.3.4 Sample Preparation

For silicon samples, substantial preparation work is needed before SSRM can be successfully conducted. After cleaving the sample either manually or with a dicing saw, successive polishing steps with incrementally finer grit sanding paper is followed by further polishing with even finer grit diamond lapping films. Final polishing may be done with aluminium oxide lapping films with grit sizes as small as 50 nm [53].

For SCM on silicon samples Williams [54] and Kopanski [46] both point towards the need for thorough mechanical polishing after cross sectioning, followed by the formation of a thermal oxide. Kopanski mentions that the surface quality can be further improved by using chemical-mechanical polishing in the final polishing step and also by performing a post-polishing anneal at 300°C under UV radiation.

For zinc oxide as well as indium phosphide, the preparation may be far simpler. Often, samples can be measured as cleaved without requiring neither cleaning nor polishing [40, 43, 44, 55], but the results depend heavily upon the prior processing of the sample. For instance, implanted samples in some cases suffer from significant crystal damage which results in excessive roughness of the cross section upon cleaving.

No reports have been found on scanning spreading resistance microscopy nor its preparation on sapphire based structures, but simply cleaving the sample manually without further processing has been used for SCM [49]. The authors express concerns that this probably limited the resolution of their experiment, but they could not achieve better results with more elaborate preparation routes. Wang *et al.* and Douheret *et al.* have successfully used the same technique for ZnO and InP substrates, respectively [50, 52].

2.4 Scope of This Work

The key goal of this project is to develop SSRM and SCM for applications on thin film zinc oxide structures. As no standardized procedures are available for the relevant materials, a fundamental part of this lies in the establishment of cross sectional sample preparation routines enabling reliable and reproducible reults.

The developed techniques will be applied in exploring the applicability of SSRM and SCM to typical and important thin film structures. For this part of the project, structures synthesized by sputtering, in-diffusion, ion implantation, and epitaxial growth will be examined, several of which are subjects to other ongoing masters and PhD projects. In particular, it will be examined whether SSRM or SCM is capable of detecting the two-dimensional electron gas in ZnO heterostructures reported by several groups.

Chapter 3

Experimental Techniques

This chapter introduces the most important experimental techniques used in this thesis. As the entire work revolves around scanning probe microscopy, this receives a strong focus and is presented first. Section 2 covers scanning electron microscopy as this has also been utilized routinely, while the remaining sections describe relevant methods for sample synthesis and preparation.

3.1 Scanning Probe Microscopy

Scanning probe microscopy (SPM) is a vast family of techniques used for characterization of surface properties such as *e.g.* topography, temperature, resistance, capacitance, magnetic properties, adhesion, and elasticity [56, 57]. The common feature of the SPM techniques is that the surface is investigated by scanning a sharp probe across it in a raster pattern while measuring the property of interest along the way. The scanning motion can be achieved either by keeping the sample fixed and moving the probe or, conversely, by keeping the probe fixed while moving the sample. In both cases the motion is effected by piezoelectric actuators which provide nanometer resolution. The following sections introduce the SPM techniques utilized in this project.

3.1.1 Atomic Force Microscopy

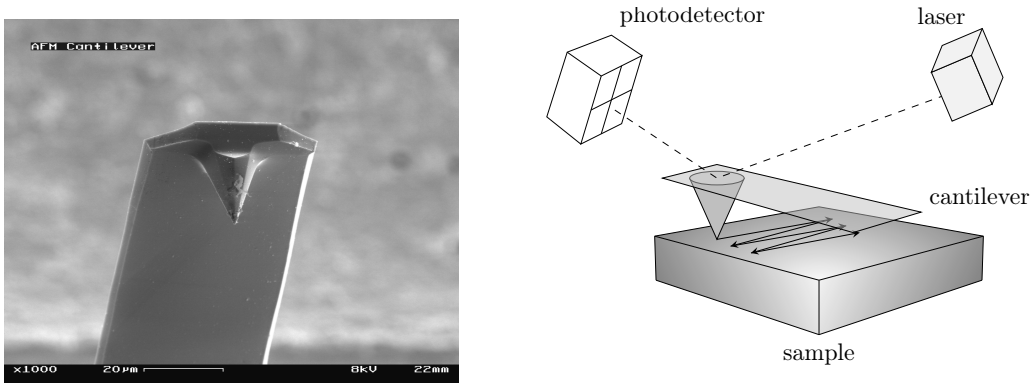

(a) **(b)**

Figure 3.1: *(a) A scanning electron micrograph of a typical probe used in atomic force microscope consisting of a sharp tip on the end of a comparatively long cantilever [58]. (b) The working principle of an atomic force microscope.*

In the early 1980s, Gerd Binnig and Heinrich Rohrer developed the first of the scanning probe microscopes, the scanning tunneling microscope (STM), which won them the Nobel prize in physics in 1986. The STM measures topography with angstrom resolution, but is based on the detection of a tunnelling current between the probe and the sample, restricting its applicability to conductive samples only [59].

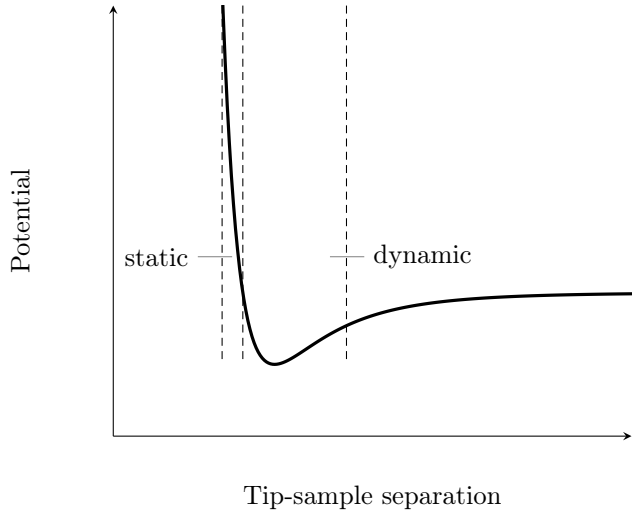

Figure 3.2: *Schematic of the Lennard-Jones potential used to describe the tip-sample interactions in an atomic force microscope .After [64]*

In the same year that he was awarded the Nobel prize Binnig, along with Calvin Quate and Cristoph Gerber, invented the second member of the SPM family, the atomic force microscope (AFM) which enables topographic characterization regardless of sample conductivity [60]. These instruments have a vertical resolution of < 1 nm and in-plane resolution down to $0.1 - 0.2$ nm [61]. For certain materials, even atomic resolution has been achieved, see for instance [62, 63]. Minimal sample preparation is strictly required[1], and samples can be investigated in air, vacuum, as well as in aqueous solutions while temperatures may typically range from 4 K to 250°C. This range of applicability has made AFM one of the most widely used measurement techniques in materials science today [64].

The probe used in the AFM consists of a cantilever which is held fixed at one end and has a very sharp tip on the other end as seen in figure 3.1a. Typical cantilevers may be 50–250 µm long with a radius of the tip curvature of 2–50 nm [64]. The height of the cantilever over the sample is adjusted through a piezoelectric actuator ensuring accurate control of the interaction between the probe tip and the sample.

As the probe tip is brought in proximity of the sample it experiences a variety of forces, of which the most important are attractive van der Waals forces, short range repulsive forces, adhesion, and capillary forces. The van der Waals forces arise from asymmetries in the electron clouds surrounding the atomic nuclei in the tip and sample. Such instabilities may be caused by fluctuations in the thermal- or zero-point energy of the atoms. The short range repulsive forces come into play when the separation of the tip and the sample is so small (on the order of angstroms) that the electron clouds of the tip atoms overlap with those of the surface atoms. In the limit where these forces dominate the van der Waals forces the probe is considered to be in "contact" with the sample. Capillary forces apply in experiments done under ambient conditions. At atmospheric pressure, a thin film of water covers any hydrophilic surface and as the tip comes in contact with the water, an attractive capillary force pulls the tip towards the surface [65]. The combination of these forces is well represented by the Lennard-Jones potential, illustrated in figure 3.2. At large tip-sample separations, no forces apply. As the tip is brought closer to the surface, the attractive van der Waals forces come into play, pulling the tip downwards. If the tip is lowered further still, the electron clouds eventually start to overlap and repulsion becomes increasingly powerful with decreasing separation.

The deflection of the probe is most commonly measured by the *beam bounce* technique as illustrated in figure 3.1b. This works by reflecting a laser beam off the back of the cantilever and onto a four-zone photodetector. During scanning, the various topographical features of the surface will cause a spatially changing force between the tip and the sample. As a response the cantilever bends by an amount proportional to the magnitude of the force and this changes the point of impact of the reflected laser beam on the photodetector. The output signal from the detector

[1] However, if optimal resolution is required some sample preparation is necessary.

is then a measure of the force between the tip and the sample which, assuming the base of the cantilever is held at a fixed height, is directly proportional to the topography of the sample.

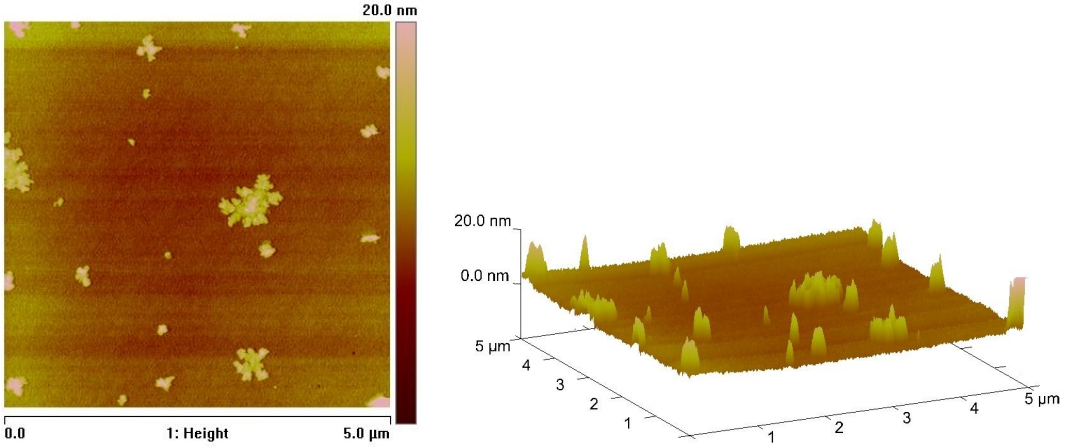

(a) (b)

Figure 3.3: *(a) A 2D and (b) a 3D representation of the same AFM measurement.*

The output from an AFM measurement is a list of (x, y) coordinates, each with a corresponding measured height. The dataset can be presented in various ways, of which a 2D or 3D image are the most common, as shown in figure 3.3. In the case of a 2D image (figure 3.3a), the height of each point is represented by a colour. As the scanned area is generally far larger than the height of the topographical features, the z-axis in the 3D image (figure 3.3b) is greatly magnified. It is therefore important to pay close attention to the scales of the axes to get an accurate impression of the size of the features.

The atomic force microscope has a variety of operating modes, which can be coarsely divided in the simple *contact mode* (also known as static mode) and the slightly more advanced *dynamic modes*. In contact mode a measurement is initialized by moving the probe towards the sample surface until the repulsive tip-sample forces causes a predetermined deflection of the cantilever. This is defined as the "zero-level" of height. As the probe is scanned across the hills and valleys of the sample, the deflection of the cantilever continuously changes corresponding to the surface topography. The signal from the photodetector is recorded at equidistant points in the scanned area, and from each measured value a corresponding height is calculated. If the surface is rough, this can lead to large tip-sample forces, possibly damaging both tip and sample. To avoid this it is common to use feedback circuitry which continuously adjusts the height of the scanner corresponding to the measured deflection [66]. In this way the tip-sample force can be kept constant, and the motion of the scanner in the z-direction is the recorded representation of the surface topography. Despite this improvement, tip and sample damage are still serious concerns with contact mode operation. The most explicit forms are scratching of the sample surface and breaking of the tip upon impact with steep topographical features. More subtle and harder to detect are the effects of rounding of the probe tip. As the tip is worn, the achievable resolution gradually diminishes and surface features will appear smeared out in the captured image. This can be hard to identify, unless particular feature sizes are expected with some certainty. For these reasons, few topography measurements are conducted in contact mode.

In the dynamic modes the cantilever is set to oscillate at, or close to, its resonance frequency by a piezoelectric actuator. As the cantilever is lowered towards the surface, the tip-sample forces will affect the amplitude, frequency, and phase of the oscillation relative to the excitation signal. The change in any of these parameters can be used as a means of detecting the tip-sample forces and thereby the topography of the surface, giving rise to the three dynamic modes, amplitude-modulated (AM), frequency-modulated (FM), and phase-modulated (FM) AFM. The theoretical minimum detectable force is dictated by the thermal Brownian motion of the cantilever for all three modes. In practice, however, PM-AFM has been proven superior to the other two techniques [67].

The quality factor (Q factor) of a resonating object is commonly defined as $Q \equiv f_0/\Delta f$, where f_0 is the resonance frequency of the object and Δf is the bandwidth where the power is half of that at f_0. The probes used in the dynamic AFM modes generally have Q factors of 10 in water,

400 in air and $10^4 - 10^5$ in ultra high vacuum (UHV) [64, 68]

Amplitude-modulated AFM was the first of the dynamic modes to be developed [69]. In this mode, the cantilever is excited at an amplitude, $A \sim 1$–$100\,\text{nm}$, with a fixed frequency close to its natural resonance frequency, f_0. As the tip approaches the surface, the tip-sample forces causes a change in the oscillation amplitude ΔA [65]. A feedback circuit adjusts the height of the scanner in order to keep ΔA constant and the motion of the scanner is recorded as a representation of the surface topography. This technique is the most frequently used in measurements under ambient conditions and in liquids. As the changes in amplitude are not instantaneous but happens on a time scale of $\tau \sim 2Q/f_0$, AM-AFM is not applicable in vacuum where the Q factor of the cantilever frequently reaches values on the order of tens of thousands and the amplitude response is far too slow [68].

Frequency modulated AFM was introduced by Albrecht *et al.* in 1991 [70], and is today the most commonly used technique for measurements in vacuum. Here the cantilever is oscillated at its resonance frequency, maintaining a constant amplitude at all times. As the tip is influenced by the forces from the surface, the resonance frequency changes by an amount, Δf. During measurements the height of the scanner is continuously adjusted to maintain Δf at a predetermined value, and the motion of the scanner is recorded as a representation of the surface topography [65]. The advantage of FM-AFM over AM-AFM in vacuum is that unlike the amplitude, the frequency change occurs within a single oscillation cycle with a time constant given approximately by $\tau \sim 1/f_0$, independent of the Q factor. The high Q factor achieved in vacuum gives the frequency modulated mode a very high sensitivity [68]. FM-AFM is, however, not used in ambient conditions as it requires two feedback loops which makes it slower than AM-AFM for low Q factors [65].

The most recent addition to the dynamic AFM modes is the phase modulation technique. In this mode the cantilever is excited at a fixed amplitude at its resonance frequency, and the tip-sample interactions are detected as a phase difference between the cantilever and the excitation signal. This phase difference is routed back to the scanner through feedback electronics adjusting the height of the scanner in order to maintain a constant phase difference. Like in the other dynamic modes, the motion of the scanner is recorded. The phase is not influenced by the Q factor of the cantilever, making PM-AFM a feasible alternative to FM-AFM for experiments conducted in vacuum [67]. Kobayashi *et al.* [71] has shown that PM-AFM is also applicable in experiments done under ambient conditions, demonstrating a one order of magnitude increase in the signal-to-noise ratio over AM-AFM.

The silicon cantilevers commonly used in AFM are not without drawbacks. The two most notable are a the low Q-factor in air and the dependence upon the laser-photodetector system which may lead to light-induced artifacts in some applications. To overcome these challenges, a completely different type of probe has been designed around a quartz tuning fork, where the probe tip is formed on the end of one of the tines. Due to the piezoelectric properties of quartz, the application of an alternating voltage to electrodes on the tines can set them to oscillate, and from a separate set of electrodes the amplitude, phase, and frequency of the oscillation can be read out [72].

According to [69], the vertical resolution, r, of the AFM follows

$$r \propto \sqrt{\frac{k}{Qf_0}}$$

where k, Q, and f_0 are the force constant, Q-factor, and resonance frequency of the probe, respectively. For biological-, or other samples where adhesion might be an issue, a probe with a high force constant is required, which is detrimental to the resolution due to the low Q-factor of the ordinary cantilever probes. Due to their design, the tuning fork probes typically have Q-factors one order of magnitude higher than that of the ordinary cantilevers allowing the use of higher k probes while maintaining the resolution. Several groups have demonstrated atomic resolution with these probes, *e.g.* in [73, 74].

A fundamental limitation of the AFM is caused by the finite size of the probe. If a sharp vertical step is encountered, the bevel of the tip will cause the measured profile to appear more gradual than it really is, as illustrated in part (a) of figure 3.4. Feature (b) is still to steep to be resolved, and it is impossible to differentiate this from feature (a). Features (c) and (d) illustrate the effect of feature height on apparent lateral dimensions. Higher features are more strongly affected by the probe size, and thus appear to have larger lateral dimensions than equally wide, but lower,

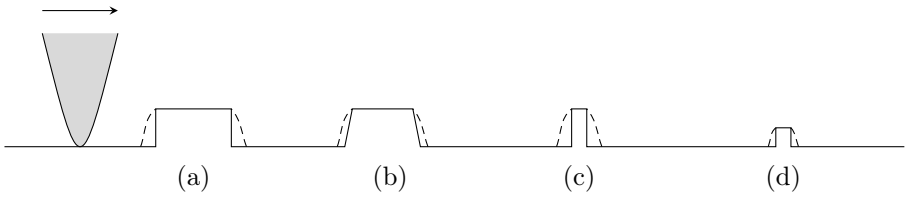

Figure 3.4: *Schematic of a sample with various topographical features. The path of the probe is indicated by the dashed lines. Figure after [64]*

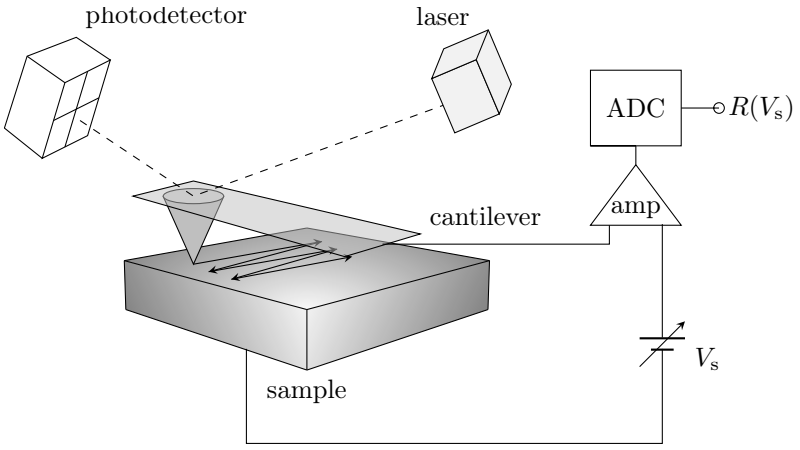

Figure 3.5: *The working principle of a scanning spreading resistance microscope, after [53].*

features. The same kind of errors will result if the hills in figure 3.4 are replaced by equally shaped valleys.

An important feature of the AFM is that its capabilities can be extended by fitting various add-on modules. One such module enables the AFM to be used for scanning spreading resistance microscopy.

3.1.2 Scanning Spreading Resistance Microscopy

Scanning spreading resistance[2] microscopy (SSRM) is a technique developed for two-dimensional charge carrier profiling and can be regarded as the successor of the spreading resistance probe (SRP) technique. The advantage of SSRM over SRP is the significantly reduced radius of the probe tip apex which allows experiments to be conducted on cross sectioned samples without the need for beveling. This eliminates challenges related to bevel rounding [75], carrier spilling [76], and surface damage caused by the beveling process [77]. Also, unlike their SRP counterparts, the SSRM probes do not require any form of conditioning and can be used in experiments directly as received from the manufacturer [78].

In scanning spreading resistance microscopy an AFM is fitted with a conductive probe, typically made from silicon coated with a layer of boron doped diamond. The probe is connected in a circuit with an adjustable voltage source, a current amplifier, and an analog to digital converter (ADC) as illustrated in figure 3.5. A DC bias is applied between the probe and the sample and the resulting current is measured, amplified, and recorded. The amplifier must have a large dynamic range, high sensitivity for small currents, and a good signal-to-noise ratio. These demands effectively rule out the use of simple linear amplifiers as their sensitivity rapidly diminishes when measuring resistances dissimilar from the reference value. The current amplifiers in practical implementations of SSRM are therefore most often logarithmic and typically provide a range of 10 pA to 100 µA [53].

To ensure sufficient tip-sample contact most SSRM experiments are done in contact mode, but applicable dynamic modes have also been developed. A high force is required in order to penetrate

[2]The Electrical and Electronics Engineering Dictionary defines spreading resistance as: *"For a contact with a small area, such as a point contact, the resistance which does not lie strictly along the path between electrodes. This may occur, for instance, in semiconductor materials whose dimensions are large in relation to such a contact. . . . "* [79]

any native oxide on the sample. The exact recommended value has been decreasing steadily as the technique has matured and a recent paper suggests a force of 1–5 µN to be suitable [80]. In a first approximation the probe-sample contact is assumed perfectly ohmic, and the measured resistance assumed to be caused solely by spreading resistance, following

$$R_{\text{spreading}} = \frac{\rho}{4a}, \tag{3.1}$$

independent of applied bias [81]. Here, ρ is the local resistivity of the sample and a is the radius of the tip-sample contact area. In this approximation, the bias voltage can be chosen freely to obtain the optimum signal-to-noise ratio. Care must however be taken, as an excessive voltage may permanently damage the sample due to the high current density. In practice the probe shape, force between tip and sample, surface states, as well as non-uniform sample resistivity must be accounted for, thus

$$R = \text{CF}(a, \rho)\frac{\rho}{4a} + R_{\text{contact}}(\rho) \tag{3.2}$$

has been proposed as a more accurate representation of the measured resistance [81]. CF is a correction factor accounting for the spreading of current from the location of the probe to nearby layers of lower resistivity, while R_{contact} is the non-zero contact resistance between the probe and the sample. The correction factor is a function of the three-dimensional resistivity distribution in the region beneath the probe and can typically not be found analytically. Instead, the conversion from measured resistance to carrier density is performed by making a first approximation of the resistivity profile based on the resistance profile, comparing this to a predetermined database of correction factor profiles, calculating a new resistivity profile based on the correction factor profile, and then iterating until convergence. When the resistivity profile has been found, the mobility equation (2.14) and the Poisson equation

$$\nabla^2\varphi = -\frac{q}{\varepsilon}(N_{\text{D}}^+ - N_{\text{A}}^- + p - n), \tag{3.3}$$

are used to determine the charge carrier profile. Here, q is the elementary charge, n and p are the concentrations of electrons and holes while, ∇^2 is the Laplacian operator, φ is the electrostatic potential, ε is the dielectric constant of the material in question, and N_{A}^- and N_{D}^+ are the concentrations of ionized acceptors and donors, respectively. In this project, SSRM is used only for qualitative measurements and no conversion to carrier density is attempted.

In practice, there will always be some resistance in the wiring, probe, connectors, and any other part of the measurement system. The measured resistance is thus the sum of all these contributions and not strictly the spreading resistance alone. However, since the spreading resistance is inversely proportional to the contact area and the probes used have an apex radius down to only a few tens of nanometers, it is a common approximation that the total resistance of the system is dominated by $R_{\text{spreading}}$ and that the first term of (3.2) is a good representation of the measured resistance.

In addition to the spatial resolution, the resolvable carrier gradient [nm/decade] and concentration sensitivity, *i.e.* the ability to detect marginally different concentrations, are important performance metrics for a carrier profiling technique [82]. Also, for broad applicability, a large dynamic range is desirable. For SSRM, the resolvable carrier gradient is on the order of 1–2 nm/decade [82] while the sensitivity and dynamic range (10^{14}–$10^{19}\,\text{cm}^{-3}$) are comparable to SRP [78]. Interestingly, the spatial resolution has been reported to be better than 5 nm even though typical tip radii are larger than 5–10 nm. Two factors influence this. Firstly, as the diamond coating of the probe tip is not perfectly smooth, contact can be made between the surface and crystallites of the tip which are smaller than the overall radius. Secondly, it has been found that the high pressure from the tip onto the surface may cause a phase transition in the surface material in the region around the contact point, and that it is the size of this region which determines the resolution. In silicon samples the region under the probe transitions into a so called beta-tin phase which exhibits metallic conduction. Other materials show similar behaviour [80, 83]. Overall, SSRM is regarded as at least as good as SCM, and generally better than SEM, KPFM, and electron holography for 2D carrier profiling [84]. The technique can also be used as a complement to SIMS for electrical characterisation. The key difference in the output is that SIMS provides information about the *dopant* distribution, whereas SSRM gives information about the *carrier* distribution.

Like for any other characterization technique, it is important to be aware of the limitations of SSRM in order to correctly interpret its results. One of the key assumptions of the technique is that the tip-sample contact shows ohmic behaviour. If this assumption fails, the recorded resistance

will not be a true representation of the resistivity of the sample. Like in the case of AFM, the use of a probe of finite size also introduces uncertainties. One issue is that if the probe passes an abrupt boundary between regions of considerably different resistivity, the tip will briefly contact both layers at the same time. The result is that such junctions may appear more gradual that they really are, especially if a worn probe is being used. A second probe related challenge is that due to the high force required for contact, the probe may dig a groove in the sample as it is scanned across the surface. As the probe is pulled out of the groove when it reverses direction at either end of the scan line, the electrical contact may momentarily be lost, resulting in the recording of an unexpectedly high resistance along the edges of the image. If the probe runs over the edge of the sample during scanning it easily breaks. To reduce the risk of this happening, measurements are typically performed a few hundred nanometers away from the edge if possible. Determining the exact distance is however difficult without risking running the probe off the sample, and it is complicated by that this distance will gradually change from one end of the scanned area to the other if the sample is not perfectly aligned with the scanners of the microscope.

3.1.3 Scanning Capacitance Microscopy

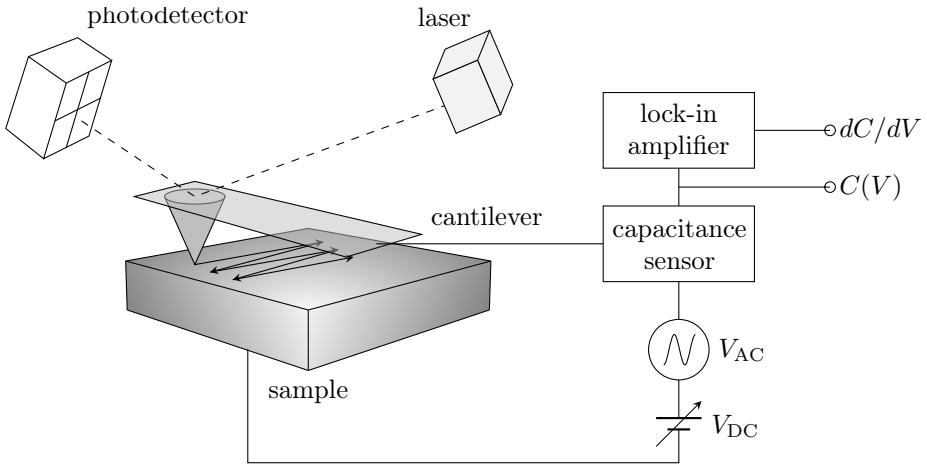

Figure 3.6: *The working principle of a scanning capacitance microscope. After [46].*

Complementary to SSRM, a second method of characterizing the charge carrier distribution of a material is scanning capacitance[3] microscopy (SCM). On the macroscopic scale, capacitance measurements gives direct access to the carrier concentrations without influence from the mobility. Like SSRM, SCM is based on the atomic force microscope, but cantilevers of lower force constant and different electronics are employed. The capacitance measurement circuitry consists of AC and DC bias voltage sources, a capacitance sensor, and a lock-in amplifier as illustrated in figure 3.6. The following is based on [46].

Traditionally, scanning capacitance microscopy has been performed with the probe tip in constant contact with the sample surface. The technique is based on alternating accumulation and depletion of charge carriers from the region directly beneath the probe, and therefore requires the formation of either a metal-insulator-semiconductor (MIS) or a Schottky junction between the tip and the sample. For simplicity only the MIS case is explained. Extension to Schottky contacts must account for the flow of current when the junction is forward biased.

The driving force for the accumulation and depletion is an AC voltage with a magnitude, V_{AC}, on the order of a few volts and a frequency, ω_{AC}, in the range 10–100 kHz which is applied between the probe and the sample. When the probe is positively biased with respect to the sample, electrons accumulate close to the probe while holes are pushed away. In the opposite case the holes are attracted and the electrons repelled , and the region is said to be depleted of electrons. V_{AC} is centered around a DC level, V_{DC}, which ensures that both attraction and repulsion of the charge carriers occur during each period of the AC signal. The result is a voltage dependent separation of

[3]Capacitance, C, is a measure of the ability of a device to store electric charge, generally expressed as $C = |dQ/dV|$, where Q is the amount of charge stored and V is the applied voltage [5, p.213].

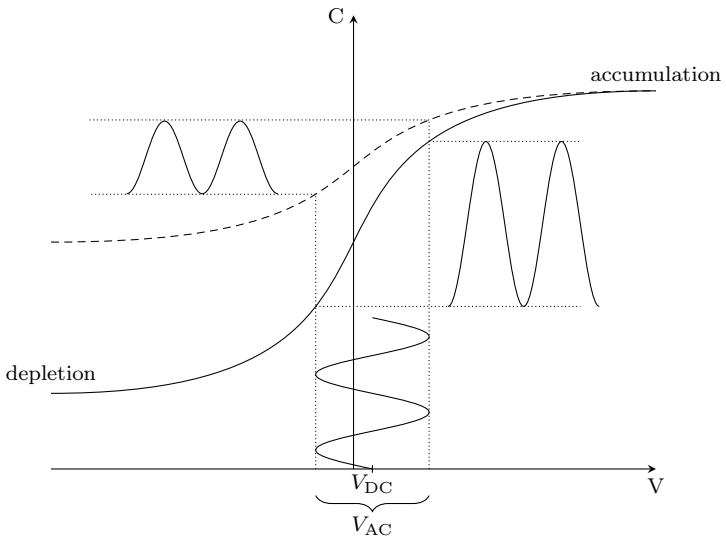

Figure 3.7: *A generic CV curve. The applied AC and DC biases as well as the changing capacitance signal is indicated in the case of a high (dashed line) and low (solid line) electron concentration. After [46].*

the charges in the probe tip and the electrons in the sample. This situation can be approximated as a parallel plate capacitor following

$$C = \frac{\varepsilon A}{d}, \tag{3.4}$$

with C being the capacitance, ε being the dielectric constant of the medium between the plates, A the plate area, and d the separation between the plates. When the majority carriers are attracted to the probe tip, d is small, and when they are repelled d is large. The consequence is that the capacitance is proportional to V_{AC} in the case of an n-type semiconductor and inversely proportional to V_{AC} for a p-type semiconductor. As the area of the probe tip is extremely small, the magnitude of the capacitance is generally on the order of attofarads and difficult to measure. The solution is to construct the measurement system such that the measured quantity is not the capacitance, C, itself but rather the change of capacitance with voltage, dC/dV. A highly sensitive capacitance sensor detects this changing capacitance and outputs a proportional voltage signal, which in turn is amplified by a lock-in amplifier. The result is a measure of the amplitude and phase of the differential capacitance caused by the changing voltage. Figure 3.7 shows a generic capacitance-voltage (CV) curve, from which both the dominant carrier polarity and its concentration can be qualitatively determined. In an n-type semiconductor with a low concentration of electrons only a small bias voltage is required to deplete the region beneath the probe. The few electrons which are present are pushed far away, resulting in a very low capacitance. For n-type semiconductors with a higher electron concentration a larger voltage is required to produce appreciable depletion. The high electron density and comparatively small depletion width results in a higher depletion capacitance than in the low-n case. P-type samples behave the same, but for the opposite polarity of V_{AC}. From figure 3.7 it can be identified that the magnitude of the slope of the CV curve (dC/dV) can be used as a measure of carrier density in the sample, while the phase of the CV curve with respect to the excitation signal provides information of the polarity of the dominant carrier species. The scanning capacitance microscope provides maps of both the magnitude and phase of dC/dV as outputs.

An evolution of the contact mode SCM is the tapping-SCM technique. Here the capacitance is measured as a function of tip-sample distance by a lock-in amplifier referenced to the cantilever oscillation frequency. The advantage is that no modulation of the depletion region width is required to produce a capacitance change, hence the technique can be used on non-semiconducting materials.

3.1.4 Temperature Dependent Scanning Probe Microscopy

Many important electrical properties of semiconductor materials are temperature dependent. A few of these properties and their temperature dependence are given in this section, which follows

chapter 2 of [85].

The magnitude of the band gap has been found to decrease with increasing temperature according to the Varshni equation

$$E_{\mathrm{g}}(T) = E_{\mathrm{g}}(0) - \frac{\alpha_E T^2}{T + \beta_E}, \tag{3.5}$$

where $E_{\mathrm{g}}(0)$ is the band gap at absolute zero, T is the temperature, and α_E and β_E are material-specific constants.

The densities of electrons and holes, n and p, respectively can be calculated from (2.12) and (2.13) and are found to depend on temperature according to

$$n = N_{\mathrm{c}} e^{-(E_{\mathrm{c}} - E_{\mathrm{F}})/(kT)} \tag{3.6}$$

$$p = N_{\mathrm{v}} e^{-(E_{\mathrm{F}} - E_{\mathrm{v}})/(kT)}, \tag{3.7}$$

where N_{c} and N_{v} are the effective densities of states in the conduction and valence band, respectively, and the remaining symbols have the same meaning as before. For a doped semiconductor the carrier concentration rises sharply once the thermal energy is sufficient to ionize the dopant atoms. After the dopants are fully ionized, the carrier concentration is independent of temperature until the temperature is so high that significant excitation from the valence band to the conduction band can take place. This excitation of intrinsic charge carriers follows

$$n_{\mathrm{i}} \propto T^{3/2} e^{-E_{\mathrm{g}}(0)/(2kT)}. \tag{3.8}$$

The mobility of charge carriers is, among other effects, limited by scattering from phonons and coulombic interactions with charged species. Each of which have some degree of temperature dependence. The inverse of the effective mobility is found by taking the inverse sum of the mobility due to each of these components, where the mobility due to phonon scattering is proportional to $T^{3/2}$, and the mobility due to coulombic interactions is proportional to T. Considering only these two causes of scattering, the effective mobility becomes

$$\mu_{\mathrm{eff.}} \propto \frac{T^{5/2}}{T^{3/2} + T}. \tag{3.9}$$

More advanced SSRM and SCM setups allow measurements to be performed in a chamber with accurately controlled temperature by, for instance, implementing cooling with liquid nitrogen. In this way, successive scans can be performed at different temperatures to characterize the temperature dependence of the charge carrier density, mobility, and electrical resistivity distribution of the sample.

3.2 Scanning Electron Microscopy

This section is based on chapters 1 and 5 of [86].

The smallest feature distinguishable in an optical microscope is given by the *Rayleigh criterion*

$$\Delta x \sim \frac{0.6\lambda}{\sin\theta}, \tag{3.10}$$

where Δx is the feature size, λ is the wavelength of the light, and θ is the angle subtended by the aperture which the light passes through. In the case of large apertures $\sin\theta \sim 1$, so $\Delta x \sim 0.6\lambda$. Visible light has wavelengths in the range 300–700 nm giving an optimal resolution of ~ 180 nm. To improve resolution, ultraviolet (UV) light ($\lambda \sim$ 100–300 nm) or x-rays can be used. By (3.10), UV ligh microscopes have a resolution limit of about 60 nm which is still too large for many of today's applications. X-ray microscopes on the other hand rely on a syncrotron source for producing sufficiently intense x-rays, which greatly reduces their desirability due to the size and cost of such sources. To allow studying minute features without the use of x-rays, a scanning electron microscope (SEM) is commonly used. Here electrons are used in place of light, typically yielding a resolution in the range 1–10 nm.

The working principle of an SEM is illustrated in figure 3.8. Electrons are emitted from an electron gun and accelerated towards the sample by a potential of between a few hundred volts and

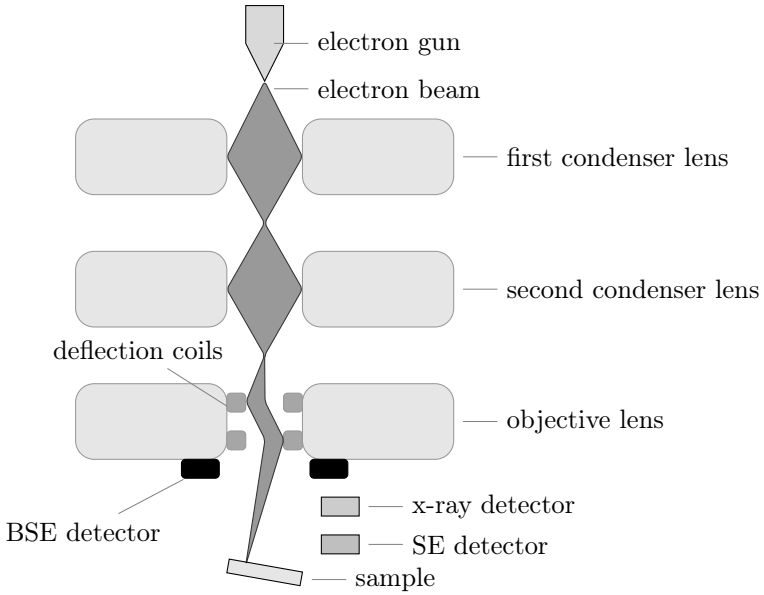

Figure 3.8: *Cross sectional schematic of a scanning electron microscope. Illustration based on [87].*

about 30 kV. After being shaped by condenser and objective lenses, the beam is scanned across the sample, where it causes emission of electrons. The emitted electrons are collected by a detector, and after the signal has been amplified an image is presented on a display. Areas of the surface which are directed towards the detector will scatter more electrons into it than areas which are tilted away and will thus appear brighter in the resulting images.

The electron gun typically generates electrons either by heating of a tungsten or LaB_6 filament (thermionic gun), or by applying a high electric field to a tungsten single crystal (field emission gun). The field emission gun typically has the highest resolution and longest lifetime, but it is also the most expensive and requires the highest vacuum ($\sim 10^{-11}$ Torr, versus $\sim 10^{-5}$ Torr for a tungsten gun). The condenser lenses act to converge the electron beam to a point below. After convergence the beam diameter increases again, before it is reconverged by the objective lens and directed at the sample surface. While both the condenser and objective lenses impact the diameter of the electron beam at the sample, the largest influence comes from the condenser, and the main task of the objective lens is to focus the beam [88].

As the electron beam impinges on the sample, several kinds of emission occur. The most important for scanning electron microscopy are the backscattered and secondary electrons emitted due to the incident (primary) electrons. The secondary electrons (SEs) are electrons belonging to atoms of the sample which are emitted due to the energy of the beam. These electrons generally have low energies, and the only ones that make it to the detector are the ones emitted from the topmost ~ 2 nm of the sample. The secondary electrons thus provides information of the surface structure [86, p. 131].

The backscattered electrons (BSEs) are beam electrons which have been scattered by the sample. These generally have significantly higher energy than the secondaries, and hence the two kinds can be distinguished by energy measurements. The BSEs can result from scattering events at half the penetration depth, which can mean up to hundreds of nanometres. These electrons thus probe the bulk of the sample [86, p. 137]. An important feature of the BSEs is that their energies are directly related to the element that scattered them. This provides elemental contrast, contrary to the secondary electrons which show topographical contrast.

In addition to electrons, x-rays are also emitted as the primary electrons cause shell transitions in the atoms of the sample. The energy of the emitted x-rays can be used to determine the element which produced them, and this allows the SEM to be used for identifying the elemental composition of the topmost 2 µm of a sample [89]. This technique is called energy dispersive x-ray spectroscopy (EDS).

The two most essential settings of an SEM are the accelerating voltage and the probe current. The voltage directly affects the incident energy of the electron beam, and excessive voltages may permanently damage the sample. High voltages will also provide electrons in a comparatively large

volume with enough energy to reach the detector, thereby reducing image resolution. The probe current determines how many electrons are incident on the sample per unit time. Using a low probe current results in good resolution, but a bad signal to noise ratio, while for a high probe current the opposite is true.

As SEM experiments proceed by bombarding the sample surface with electrons it is essential that the studied specimen is electrically conductive to avoid charging effects and possibly sample damage. Samples which are not inherently conductive can be coated with a suitable metal prior to investigation in the SEM.

3.3 Physical Vapour Deposition

Physical vapour deposition (PVD) refers to several ways of depositing materials on top of a substrate. Common for these techniques is that they are based on liberating the deposited material from its source by physical, rather than chemical, processes. Two such methods are described in the following sections, both based on chapter 12 of [8].

3.3.1 Thermal Evaporation

Thermal evaporation was for a long time the method of choice for creating metallised contacts to integrated semiconductor circuits. In today's industry, evaporation has largely been superseded by sputtering due to better step coverage and wider range of applicable materials. Evaporation however continues to be a valuable tool in research and prototyping as it is a quick and simple process which produces predictable results.

Thermal evaporation takes place in a vacuum chamber pumped to a pressure below 10^{-3} Torr. In the bottom of the chamber, the material to be deposited, called the *charge*, is placed in a crucible of high melting point. The substrate is placed face down in the top of the chamber, and is set to rotate to increase the uniformity of the layer thickness. The charge is heated until reaching a molten state by passing a high current through the crucible. Due to the vacuum in the chamber, the vapour from the molten charge rises in an approximately straight line with few collisions with air molecules until it condenses at the substrate above.

To avoid any oxides or contamination from the surface of the charge from reaching the substrate, a mechanical shutter blocks the vapour stream right above the charge. Some time after the charge has melted, all the impurities from its surface has been deposited on the face of the shutter. The shutter is then opened to let the vapour reach the substrate.

Accurate control of the film thickness is provided by a crystal vibrating at its resonance frequency close to the substrate. The vapour condensing on the substrate also deposits on the crystal causing its resonance frequency to change. From this change, along with knowledge about the density of the deposited material, the film thickness can be calculated. When the desired thickness has been reached, the shutter is closed before the current through the crucible is turned off.

3.3.2 Magnetron Sputtering

The sputtering system is in effect a plasma chamber with horizontal electrodes, where the upper electrode is the cathode and the lower electrode is the anode. The substrate is attached to the anode while the material to deposit, called the *target*, is placed at the cathode. The chamber is pumped to a vacuum and a noble gas is introduced at a pressure of around 0.1 Torr. To ignite the plasma, a high voltage is applied momentarily across the electrodes resulting in dielectric breakdown of the gas in the region between. A high voltage arc shoots from cathode to anode, exciting and ionizing the gas atoms between the electrodes. As soon as the plasma has been started, the voltage is reduced. The positively charged ions are accelerated towards the cathode by the electric field and as they strike the target they eject secondary electrons as well as atoms of the target material. The electric field causes the electrons to be accelerated towards the anode, and a fraction of them will collide with gas atoms along the way. This produces more ions, thereby sustaining the plasma.

The atoms ejected from the target are electrically neutral and thus not affected by the electric field. Their only influence is from gravity, hence they fall down and adsorb on the substrate below. Upon ejection from the target the atoms have energies in the range 10–50 eV, which is about 100 times more than in the case of evaporation. The extra energy gives the atoms more time to diffuse around on the substrate surface before bonding, resulting in improved step coverage.

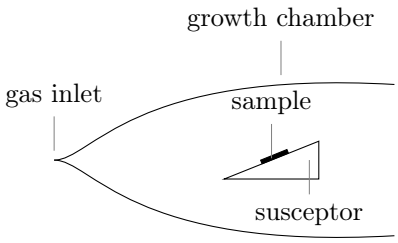

Figure 3.9: *Schematic of a MOCVD growth chamber, after [8].*

3.4 Metal Organic Chemical Vapour Deposition

This section is basedd on chapter 14 of [8].

Metal organic chemical vapour deposition (MOCVD) is a technique used for growing thin films epitaxially[4] on top of suitable substrates. Thin layers of high structural quality and low impurity concentration can be grown with well controlled thickness and dopant density. The key difference from the standard CVD technique lies in the supply of the precursor species. For growth of III-V semiconductor layers it is common to supply the group III element in the form of a liquid metal organic compound, typically based on ethyl or methyl groups. This should be chemically stable to prevent undesired reactions, and extremely pure to avoid introducing impurities into the grown layer. The organometal is heated to a carefully chosen temperature where it has the desired vapour pressure. A carrier gas, often H_2, is bubbled through the liquid and transports it to the reaction chamber via a mass flow controller. Depending on the species used, the tubing between the organometal supply and the growth chamber might need to be heated to avoid condensation, or cooled to avoid gas phase reactions.

The group V species is supplied in the form of a gas phase hydride from a high pressure cylinder. The cylinder is connected to the growth chamber through a pressure regulator, reducing the pressure to a few atmospheres, and a mass flow controller.

The growth chamber, illustrated in figure 3.9, is kept at a vacuum of about 10–100 Torr, and the substrate is placed on a susceptor maintained at 500–1000 °C. The group III and V species are mixed as close to the chamber as possible to avoid parasitic reactions, and run through the chamber in a laminar flow. The absence of turbulence and recirculation cells ensures a stable supply of gas to the substrate and is crucial for achieving uniform films. It is desired that both species adsorb to the substrate individually and delay reacting until they have diffused into proximity of each other, as reactions taking place in the gas above the substrate tend to cause irregular growth. In addition to the desired growth species the reaction produces a hydrocarbon molecule which desorbs from the substrate surface before being pumped out of the chamber by the vacuum pump.

Epitaxial growth can be used to grow a layer of material onto a substrate of (i) the same material (so called *homoepitaxy*), or (ii) a different material (*heteroepitaxy*). Perfect heteroepitaxy requires that the grown material closely matches both the crystal structure and lattice parameters of the substrate. For thin layers, differences will be compensated by straining of the epilayer. For thicker layers or unacceptably different lattice parameters, the strain is released by the formation of defects in the crystal structure.

3.5 Ion Milling

The following is based on [90] and [91].

An alternative to mechanical and chemical polishing is ion milling, which is applicable for polishing both plan-view and cross sections and also for thinning of samples prior to transmision electron microscopy. Ion milling is fundamentally a sputtering process run in reverse, where the target from the sputtering system is replaced by the sample to be polished. This takes place in a vacuum chamber pumped to about 10^{-6} Torr where ions are accelerated to an energy of a few keV, focused into a beam of micron thickness, and directed towards the sample at a shallow angle. The

[4] Epitaxial growth refers to the deposition of a crystalline layer on top of a crystalline substrate in such a way that the depostied layer takes the crystal structure of the substrate.

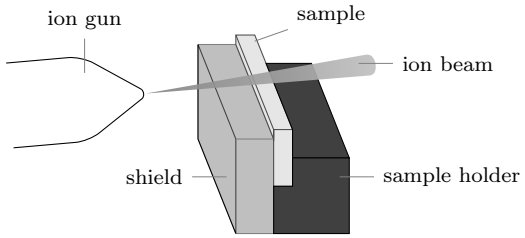

Figure 3.10: *The cross sectional ion milling setup.*

angle is chosen to encourage removal of sample material rather than implantation of the incident ions.

The ions used are most commonly Ar^+ as they are inert and heavy, but other alternatives also exist. For certain samples the use of reactive ions, *e.g.* iodine, may provide enhanced etching rates. A problem with the reactive ions is however that they might also corrode the milling chamber.

For cross sectional milling, the sample is positioned such that the beam strikes it parallel to the cross section. To avoid interacting with too much of the sample, a metal shield is placed such that only a small part of the sample edge is visible to the beam as shown in figure 3.10. To increase the polished area, the sample is continuously rotated through a predefined angle during milling resulting in a trapezoidally shaped polished area.

Some implantation will inevitably take place during the process, and this leaves a layer of physically damaged material close to the surface. In severe cases the polished surface may even be amorphized. The damage can be reduced by using lighter ions and lower accelerating voltages, but this comes at the cost of increased milling time. As a compromise, Ar^+ ions may be used while the accelerating voltage and angle of incidence is reduced gradually for incrementally finer polishing.

The ion-sample interaction may cause substantial localized heating in the area under the beam, which can reach temperatures of several hundred degrees centigrade. This can cause unintentional diffusion as well as agglomeration or segregation of defect clusters. If this is expected to be an issue, the sample may be cooled with liquid nitrogen during polishing. A final issue is caused by the sputtering nature of ion milling which implies that atoms removed from one location on the sample may redeposit in other locations.Despite these challenges, ion milling can polish many materials to a very smooth finish.

Chapter 4

Method Development

This chapter describes the developmental work done for the electrical SPM techniques. Following an introduction to the relevant equipment and the samples used, characterization of probes and back side contacts are presented. Further, a section is devoted to the development of the Matlab scripts used for data analysis before the final section covers polishing processes for silicon, sapphire, and ZnO substrates.

4.1 Equipment

Over the course of this thesis, the following equipment has been used.

AFM, SSRM, and SCM experiments have been conducted on a Bruker Dimension 3100 with a Nanoscope IIIA controller and Nanoscope 5.33 r1 software. For SSRM and SCM, boron doped diamond coated silicon probes supplied by Nanosensors have been utilized, and a logarithmic current amplifier has provided a dynamic range of 10 pA to 100 µA for the SSRM experiments. Initial low temperature SSRM experiments have been conducted on a Nanonics Cryoview SPM. SEM has been performed routinely on a Hitachi TM3000, while high resolution images have been captured in collaboration with Kristian Lausund on a Hitachi SU8230 and Muhammad Tayyib at the University College of Southeast Norway on a Hitachi SU3500. An Allied High Tech Products Multiprep tripod polisher and a Struers DAP-V turntable have been used for mechanical polishing, while ion milling has been done at JEOL on a JEOL CP, and in collaboration with Muhammad Tayyib on a Hitachi IM4000. Thermal evaporation of metals has taken place on a Balzers BAE 250. A set of reference samples to be used for method development, quality assurance, and quantification was sputter deposited in collaboration with Heine Nygard Riise, Per Lindberg, and Martin Nyborg on a Semicore TriAxis. MOCVD was done by Josef Ellingsen and Vishnukanthan Venkatachalapathy using an EMF Titan reactor. In collaboration with Asbjørn Ulvestad, polishing with focused ion beam (FIB) was conducted on a JEOL JIB-4500.

Table 4.1: *Sputter deposition parameters for the reference samples.*

Parameter	ZnO	AZO	Cu_2O
Temperature [°C]	400	400	400
Argon flow [sccm]	50	50	50
O_2 flow [sccm]	0	0	17
Al target power [W]	0	3	0
ZnO target power [W]	50	50	0
Cu_2O target power [W]	0	0	90

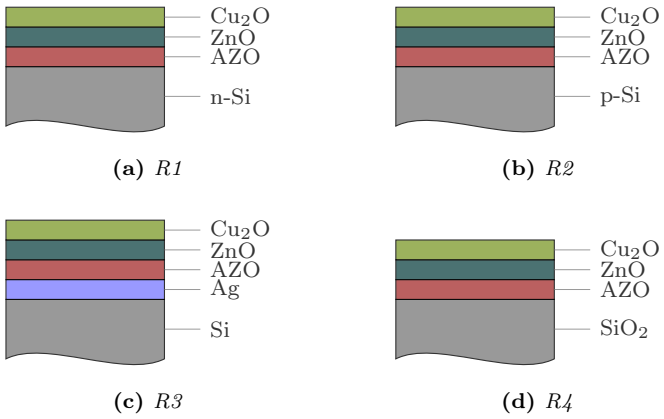

(a) *R1* **(b)** *R2* **(c)** *R3* **(d)** *R4*

Figure 4.1: *Schematic cross sections of the reference samples.*

4.2 Reference Samples

Early in the experimental work a set of reference samples were produced. These have been used for testing various polishing procedures, verifying that the Dimension 3100 could discriminate between the relevant materials, and have also provided reference levels for SSRM measurements of other samples. The reference samples consisted of a stack of thin films sputter deposited on top of (i) n-type silicon, (ii) p-type silicon, (iii) silicon with an approximately 500 nm thick thermally evaporated silver film on top, and (iv) SiO_2. These were named R1 to R4, respectively and are illustrated in figure 4.1. All the substrates were sputter coated with thin films of aluminium doped zinc oxide (AZO), nominally undoped zinc oxide (ZnO), and finally undoped cuprous oxide (Cu_2O). Each film had a nominal thickness of ∼300–500 nm, but thickness was not considered a critical parameter for these structures and was therefore not controlled rigorously. Deposition parameters for the films are summarized in Table 4.1. All structures have been examined during the work, but only results from the R3 geometry are presented as the other structures do not provide additional information.

4.3 Probe Characterization

To obtain the best possible resolution from an SPM experiment the quality of the probe, and in particular its tip, is paramount. As a part of the method development program, experiments were conducted to investigate the capability of the various available probes to produce high contrast SSRM images for thin film structures of ZnO and related materials. For optimal resolution and minimal sample damage the ability of the probe to provide high contrast at low bias voltages is important, preferably also with a low tip-sample force. Tests were done with the probes given in Table 4.2 on a polished R3 sample at voltages spanning from −4 to +4 V.

Table 4.2: *Force constants of the examined SSRM probes.*

Probe	Force constant [N/m]
Micromasch DPE16/AlBS	45
Micromasch NSC16/Ti-Pt	45
Micromasch HQ:NSC15/Pt	40
Nanosensors CDT-CONTR	0.5
Nanosensors CDT-NCHR	80
Nanosensors CDT-NCLR	72
Nanosensors PtSi-NCH	42

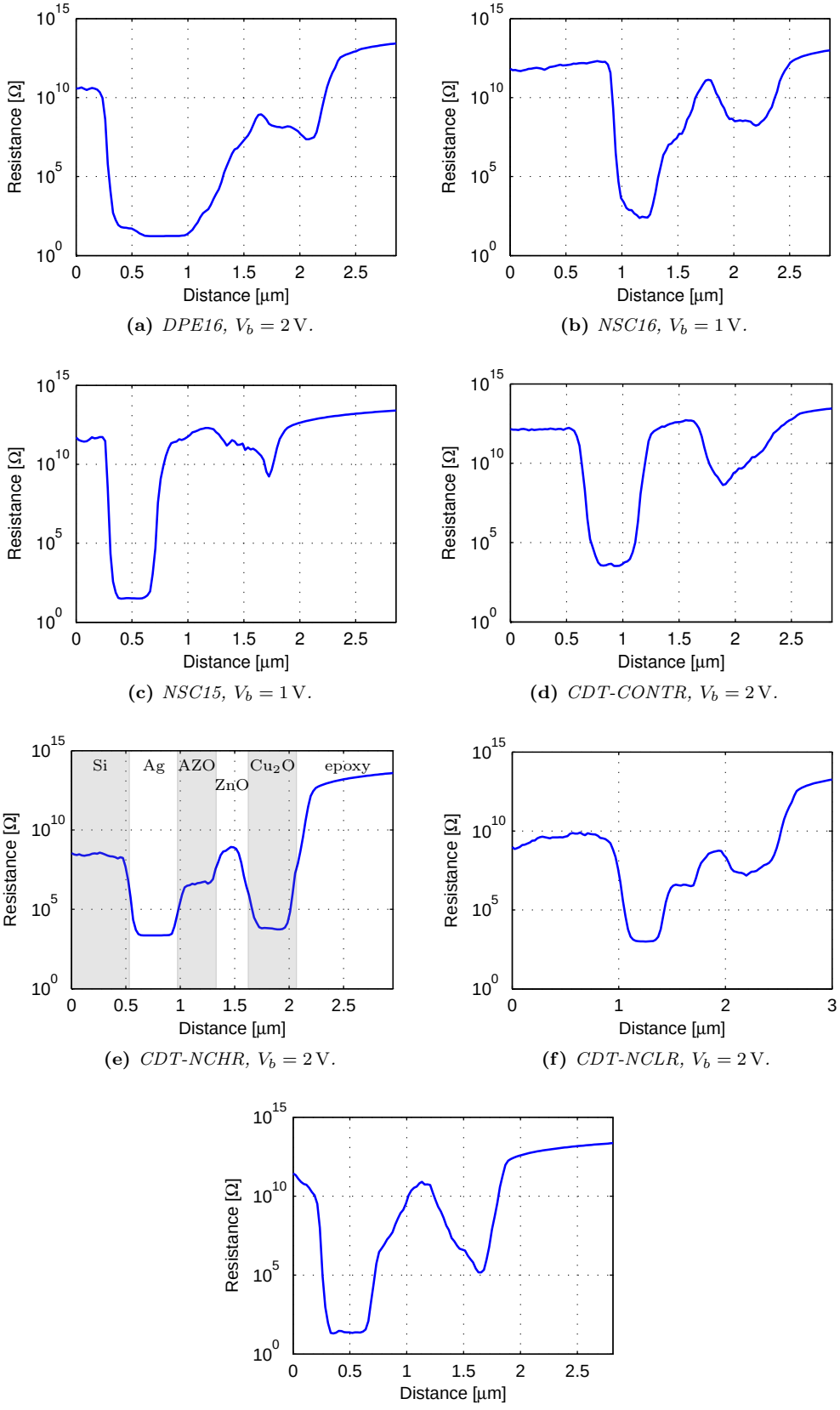

(a) *DPE16*, $V_b = 2\,\mathrm{V}$.

(b) *NSC16*, $V_b = 1\,\mathrm{V}$.

(c) *NSC15*, $V_b = 1\,\mathrm{V}$.

(d) *CDT-CONTR*, $V_b = 2\,\mathrm{V}$.

(e) *CDT-NCHR*, $V_b = 2\,\mathrm{V}$.

(f) *CDT-NCLR*, $V_b = 2\,\mathrm{V}$.

(g) *PtSi-NCH*, $V_b = 1\,\mathrm{V}$.

Figure 4.2: *Average resistance profiles of the seven SSRM probes listed in Table 4.2 when scanned across the films of the R3 sample. The applied bias voltage is given in the caption of each profile.*

All three of the Micromasch probes have silicon tips coated with a layer of platinum. The DPE16 is designed to provide stable electrical contact and low noise, at the expense of a somewhat increased tip radius of 40 nm which may limit the resolution. On the NSC16/Ti-Pt probes, a 20 nm layer of titanium is deposited beneath the platinum surface layer to improve adhesion and reduce electromigration. The resulting tip radius is the same as for the DPE16. The HQ:NSC15/Pt has a tip radius of 30 nm, and is designed for providing optimal contrast in topography and phase images.

The Nanosensors CDT range all feature boron doped diamond coatings on the tips. Although the macroscopic radius of these tips are in the range 100–200 nm, the coating is rough and has grains of size on the order of 10 nm which provide excellent resolution on flat surfaces. For the applications in this thesis, the key difference between the three CDT probes is the force constant. Where the CDT-CONTR has a force constant less than 2 N/m, the other two has force constants greater than 70 N/m. This should make the former suited for SCM experiments, and the latter two better for SSRM experiments. The last probe from Nanosensors, the PtSi-NCH, is a relatively recently developed probe for electrical characterization. This has a platinum silicide tip with near metallic conductivity and a tip radius of 25 nm.

With all probes, the tip-sample force required for achieving optimum contrast was set first, before successive scans were made while changing the bias between each scan. All scans were done in different locations on the sample to avoid influence of scratches left by prior measurements. The averaged resistance profile of the best image acquired with each probe is shown in figure 4.2, where the applied bias is given in the caption of each plot. Panel (e) has been annotated with the films corresponding to each resistance level. Ideally, all the measured probes should provide results similar to this.

From the figure it can be recognized that the Nanosensors CDT-NCHR and CDT-NCLR produces the best contrast, easily discriminating all four films. A striking difference between these two is the measured resistance in the Cu_2O film, which is measured to three to four orders of magnitude higher with the NCLR than the NCHR. The latter measures the cuprous oxide to a resistance almost as low as that of silver, which is highly surprising and discussed further in section 5.3. The remaining probes all clearly find the Ag-film, but various contrast are observed for the oxides. In particular, the interface between the aluminium doped ZnO and the pure ZnO proves challenging to pinpoint.

4.4 Back Side Contacting

In order to conduct accurate electrical SPM measurements it is important that the contacts between the sample and the measurement circuit does not have excessive resistance, and that they are of an ohmic character. In the literature there are reports that the zinc oxide–silver junction frequently used as a back contact exhibits rectifying behaviour [44,92]. Meanwhile, it has been shown that ZnO forms an ohmic contact to a eutectic mixture of indium and gallium (InGa) [93]. A comparative study of the two contact materials was thus conducted to see which would produce the best results.

Three samples which had been measured previously when contacted with silver glue were cleaned and prepared. The samples were one R3 reference sample, one low resistivity ZnO substrate with in-diffused Cu (elaborated further in section 5.1.1), and one high resistivity ZnO substrate doped with Ga. The reference sample was one where the edge was protected by a second sample rather than by an Al-slab during polishing to eliminate a parallel conduction path through the Al. The sample was polished using diamond slurry, as explained in section 4.6.2, before the exposed back side of the sample was placed on an Al-slab with a layer of InGa in between. The two ZnO samples did not undergo any preparation apart from cleaving before they were coated with InGa and attached to an aluminium support.

The three samples were measured both with identical and with different parameters than when contacted with Ag to characterize the differences. Due to either excessive resistance or too low contrast in conductivity, the high resistivity ZnO sample did not give meaningful results neither with InGa nor with Ag-paste. Averaged resistance profiles of the R3 and low resistivity ZnO samples contacted with InGa and silver epoxy are shown in figure 4.3. It can be seen that the silver paste provides the best contrast for both samples.

The reason for the unsuccessful use of InGa and the discrepancy with literature may be related to the magnitude and polarity of the applied bias voltage. In the R3 sample a bias of 2 V was

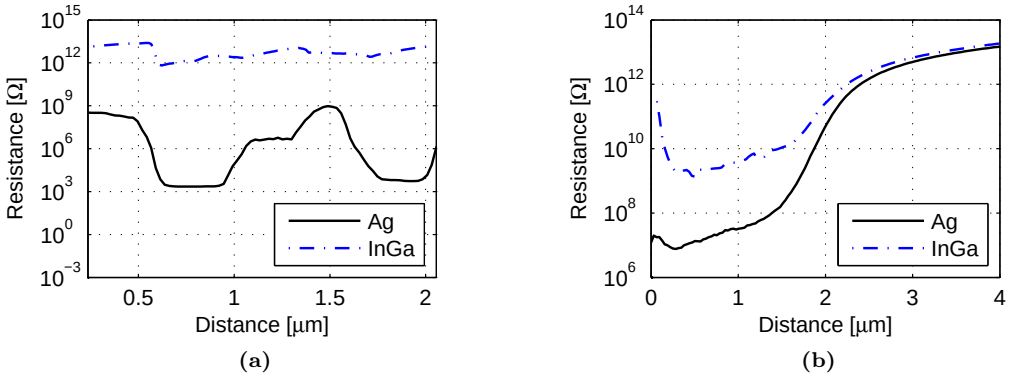

Figure 4.3: *Average resistance profiles of the (a) R3, and (b) Cu-doped ZnO samples when contacted with Ag paste and eutectic InGa. In all measurements, the bias voltage was selected to provide optimal contrast.*

applied to the sample, while in the ZnO sample the bias was 500 mV. In [44] where InGa was found to be superior to the Ag-paste on the other hand, the biases used were 6–7 V. Also, the tip-sample contact may play a role here. In this work boron doped diamond tips (CDT-NCHR) were used, while in [44] platinum coated silicon tips were utilized. A final possible cause of the discrepancy lies in the specifics of the samples themselves, where the doping concentration and sample processing may affect the tip-sample contact.

4.5 Data Processing and Quantification

To increase the data processing possibilities beyond what is provided by the software supplied with the Dimension 3100 microscope Matlab scripts have been produced. These have been used for processing all data output from both SCM and SSRM experiments. Three scripts have been written, and can be found in their entirety in Appendix A. The scripts have been written to be useful also for other users of the microscope. It has therefore been focused on readability, rather than brevity and outright performance. Here the key features of each script are described.

4.5.1 BinaryImport.m

The data files output from the Dimension 3100 are composed of a mixture of ASCII and binary data. The header of each file contains all the relevant parameters used during data capture, such as scan size, bias voltage, the number of samples per line, and various scaling parameters. The actual datapoints, on the other hand, are stored in binary form as little-endian 16-bit signed integers. The script BinaryImport.m separates the header and datapoints into two separate variables, extracts the relevant parameters from the header, and converts the datapoints into units of nanometers for the topography image and volts or degrees for the SSRM/SCM image. This script is made as a function, which takes a folder and filename as inputs and returns SSRM/SCM and topography data, as well as the bias voltage, scan size, number of samples per line and number of lines in the raster scan, to be used by the scripts described in the following sections.

To characterize the precision of the datapoint extraction and conversion routine, a typical dataset was converted from its binary form both with Bruker's Nanoscope 6 software and with BinaryImport.m. After loading the converted datasets into separate Matlab matrices, one was subtracted from the other to find the difference between the two. After doing this for numerous datasets of both topography, SSRM, and SCM data the largest discrepancy found was on the order of 10^{-5}.

4.5.2 Multiplot.m

After capture of multiple datasets, quick and easy display of the key information for initial review and discussion is desirable, hence the script Multiplot.m has been created. The files output from the microscope have names consisting of a user specified base followed by a decimal point and then

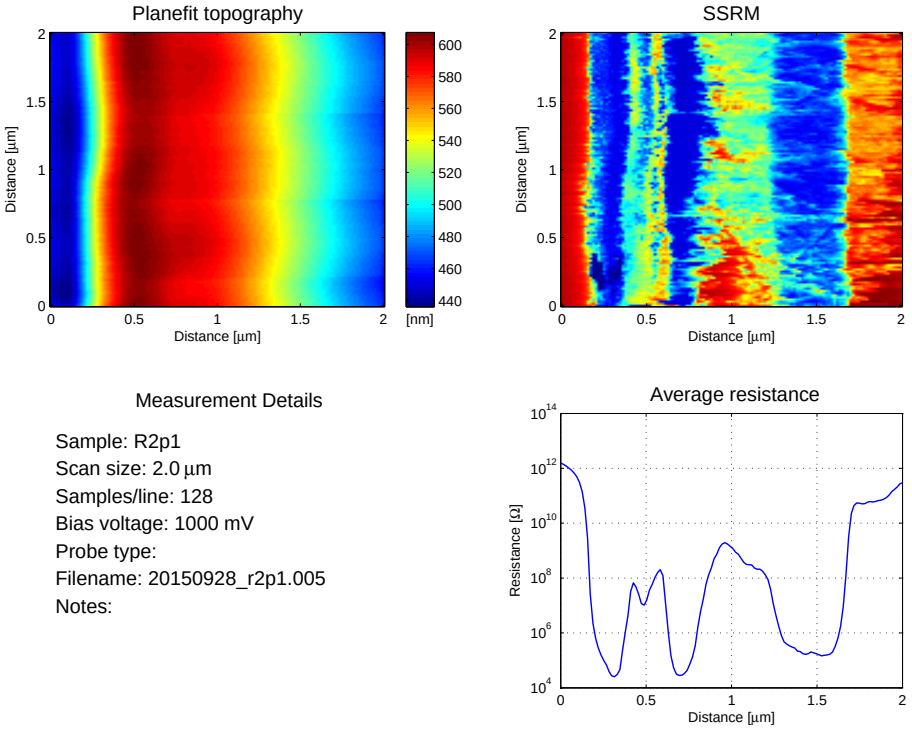

Figure 4.4: *Output of the Multiplot.m script.*

a running serial number, *e.g.* `filenamebase.001`. In the Multiplot.m script, the user specifies the folder containing the data files to be plotted, the base of the filenames, and the starting and ending serial numbers. The script then enters a loop which calls BinaryImport.m for each file, and produces plots of topography, SSRM or SCM data, averaged resistance[1] or capacitance gradient, and a text box containing key parameters of the measurement, arranged in a 2×2 panel display suitable for printing. An example of the output from an SSRM experiment is given in figure 4.4. Both topography and SSRM data are visualized in a color scheme where the lowest values are blue and the highest values are red, as this appears to provide the best contrast.

4.5.3 D3100processing.m

For processing before use in this thesis, the datasets passing the initial review are loaded into the D3100processing.m script. This script has modules providing

- Rotation of topography and SSRM/SCM images
- Planefitting of topography data
- Averaging of SSRM/SCM data
- Plotting other measurements along with the averaged SSRM/SCM data
- Plotting of measured SSRM resistance versus nominal resistivity of the sample

All these modules are based on the fact that, in Matlab, the images are represented as matrices. Image data can thus be manipulated by simply performing matrix operations on the datasets.

The ability to rotate the images is handy as it is very difficult to load the samples perfectly straight into the microscope. This algorithm works by letting the user specify a rotation factor which determines the amount of rotation. All rows above the centre of the image are then shifted in one direction, while the rows below the image centre are shifted in the opposite direction. The amount of shift applied to a given row is determined by the rotation factor multiplied by distance

[1] The averaging procedure is elaborated in the description of D3100.m.

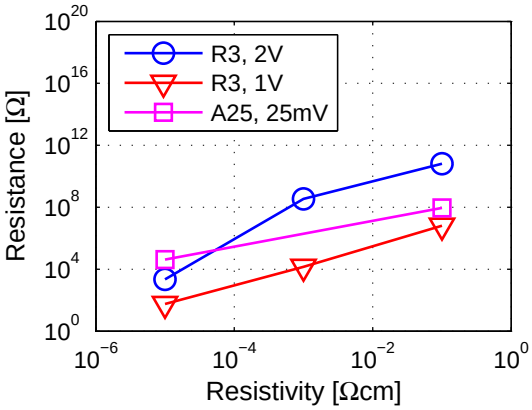

Figure 4.5: *Calibration curves for three samples measured with different probes and bias voltages.*

of the row from the image centre. This makes the rows furthest away from the center shift by the largest amount, thereby avoiding distorting the image.

As the examined samples are prepared by hand they are never perfectly level. This frequently saturates the dynamic range of the color scheme used to represent the data, and may hide fine details of the topography. To recover the details a two step planefitting algorithm has been implemented. This works by first calculating the average slope of each row of the image, and then doing a weighted subtraction of the slope from each column of the image. The weight of a column is determined by how far it is from the left edge of the image. The rightmost column is thus shifted by the largest magnitude. Once this is complete, the procedure is repeated in the up-down direction by subtracting the average slope of each column from each row. This process changes the absolute height of the datapoints, but retains their relative height which normally is what is interesting.

To filter out noise and get a clearer view of the general resistance distribution of a sample, an averaging algorithm has been implemented. As the structures of interest in the samples being studied in this work typically extend from top to bottom of the SSRM or SCM images, the averaging procedure takes the sum of the elements of each column and divides by the number of elements in the column. The result is then a row vector of average values. In the case of an SSRM experiment, each element of the vector is subsequently converted to a resistance in Ohms by a formula given in the instruction manual for the Dimension 3100. In the plot of the averaged data, other measurements from *e.g.* SIMS experiments may be included.

To correlate the measured resistance to known resistivities, a module has been added where the user can enter the nominal resistivity for a set of chosen points in the image. The script then outputs a calibration curve with resistivity on the horizontal axis and resistance on the vertical axis.

Finally, the images are formatted to a size suitable for the intended use and presented in the same color scheme as used in Multiplot.m.

4.5.4 Quantification

To relate the measured resistance with empirically known resistivities, ρ, calibration curves are commonly employed. Such curves for three different experiments are shown in figure 4.5, where the data points correspond to silver ($\rho = 10^{-5}\,\Omega$cm), aluminium doped ZnO ($\rho = 10^{-3}\,\Omega$cm), and undoped ZnO ($\rho = 10^{-1}\,\Omega$cm). An important point to note here is that the measured resistance increases monotonically with the nominal resistivity for a given probe, sample, and bias voltage. However, different experiments may give drastically different measured resistances. for a given resistivity. This is especially pronounced when comparing the red and blue curves, where a resistivity of $10^{-1}\,\Omega$cm in the red curve results in a lower measured resistance than a resistivity of $10^{-3}\,\Omega$cm in the blue curve. These curves are based on two measurements on the same sample geometry (R3) and, interestingly, the measurement conducted with the lower bias voltage reports lower resistance. This is likely caused by the use of different probes in the two cases, Micromasch NSC16 in the red curve and Nanosensors CDT-NCHR in the blue, where the former has provided

a lower contact resistance to the sample. The magenta curve stems from a measurement of the A25 geometry introduced in section 5.3.2, performed with a CDT-NCHR probe and a bias voltage of 25 mV. This experiment yields the highest resistance in the silver film, while the undoped ZnO is stated to be intermediate between the two experiments on the R3 structure.

From these results it is evident that simple comparisons between individual SSRM experiments cannot be expected to provide reliable information, neither qualitatively nor quantitatively. Within a given experiment, on the other hand, good qualitative agreement between the resistance and the resistivity can be expected as long as the polarity of the dominant charge carrier is the same in all the measured materials. If both n and p-type regions are present in the same measurement, the non-ideal-ohmic contact between the tip and the sample may significantly promote current flow in one material relative to the other, with potentially radical implications for the measured resistances.

4.6 Sample Preparation

As SSRM and SCM are performed on cross sections rather than in plan-view in this work, the first step to every sample preparation routine is to gain access to a suitable cross section. Thin films of ZnO and related oxides are grown on a variety of substrates depending on application and study. Due to their very different hardnesses, given in Table 4.3, and crystal structure, each material requires an individual preparation routine for preparing sufficiently flat cross sections. A flat surface not only increases the area suitable for scanning, but also provides better reproducibility of the experiments, less noise, and allows the probe to maintain stable contact with the surface with reduced force. This in turn causes less wear of the probe, reduced surface damage of the sample, and also reduces the "effective" tip radius, thereby improving the resolution [53, 95].

4.6.1 Cross Sectioning

Cross sectioning starts by scribing a line across the back side of the sample using a diamond tipped scriber where the sample should be cleaved, preferably along a crystallographic axis. The sample is then sandwiched, top surface down, between two parallel glass microscope slides such that the scribed line follows one edge of the slides. A sheet of clean-room paper between the bottom microscope slide and the sample prevents scratching its surface. A blunt object is used to strike the piece of sample protruding from the two slides, hopefully cleaving the sample along the scribed line. This process is repeated until the sample has the desired dimensions, which in these experiments are often an approximate square or rectangle of sides 0.25–0.5 cm. The size is arbitrary for the sake of the experiment, apart from that a larger specimen is simpler to handle.

Kopanski [46] asserts that an option to the simple cleaving procedure used here is to glue the sample face to face with a glass slide or silicon dummy before using a dicing saw to cut the sample into suitable pieces. Both this route as well as the use of a laser cutter for cleaving were assessed, but the potential increase in sample quality was considered too small for justifying the increased process time and complexity. Also, laser cutting the sample would inevitably cause uncontrolled heating of the cross sections, with unknown effects on the films.

The topography of the cross sections after cleaving depend radically on the substrate material and the history of the sample, *i.e.* what other experiments the sample has been exposed to. For instance, for a given material an ion implanted sample with poor post implantation annealing will typically have a far rougher as-cleaved cross section than, say, a carefully in-diffused sample.

Of the materials studied it has been found that zinc oxide substrates, in general, gives the smoothest cross sections, while as-cleaved silicon and sapphire typically have too much topography for reliable SPM experiments.

Table 4.3: *Room temperature Vickers hardness of substrate materials [94].*

Substrate material	Si(111)	ZnO(0001)	Al_2O_3(0001)
Hardness [GPa]	12.0	4.7	28

4.6.2 Mechanical Polishing

The optimal polishing treatment has been found to be severely dependent on the substrate material. Hence, each of the three studied substrates are treated separately in the following.

Silicon Substrates

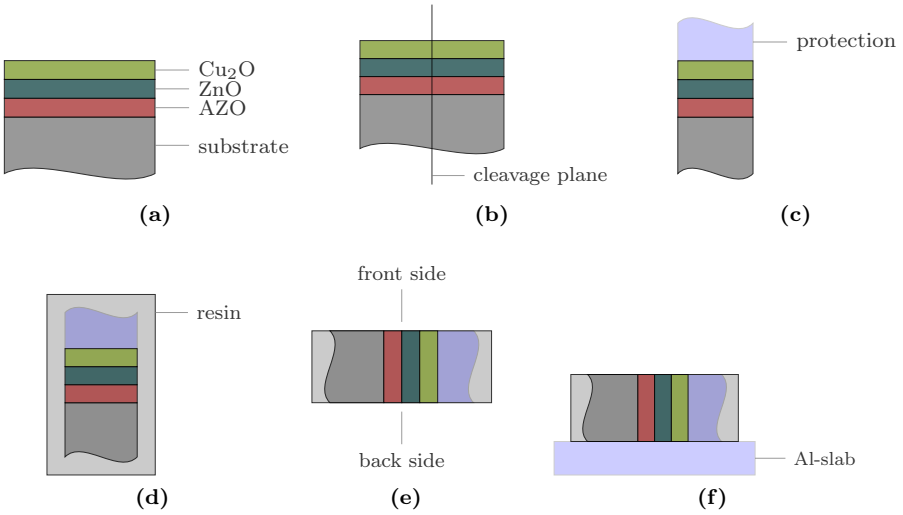

Figure 4.6: *Typical silicon sample preparation routine. (a) shows an example of a typical sample geometry. In (b) the sample is manually cleaved as explained in section 4.6.1 before it is placed against a protective slab in (c) and embedded in epoxy resin in (d). In step (e) both sides of the sample are coarsely ground with wet sanding paper until the sample is visible, and the front side is further polished. Finally, in step (f) an aluminium slab is glued to the back side with a conductive glue.*

In the earliest attempts at polishing silicon cross sections, a reference sample was glued to a metal chuck exposing the cross section to be polished. The chuck was then mounted to an Allied High Tech Products Multiprep and incrementally polished with diamond lapping films of 30, 9, 6, 3, 1, and finally 0.25 µm grain sizes. Each film was used until an examination under an optical microscope revealed that all scratches left from the previous film had been removed. Following the last polishing step the sample was removed from the chuck by dissolving the glue with acetone. Although this process is viable in theory, it was quickly found that the samples were prone to breaking both during polishing and upon removal from the chuck. Thus, for protection during polishing, experiments with embedding the samples in a cold-setting epoxy resin were conducted.

A prerequisite for SSRM studies is that a current path of reasonably low resistance exists from the area of investigation to the sample chuck of the instrument. In samples of low resistivity conduction through the sample itself may suffice, but for robustness it is in general advantageous to provide such a path externally. The Technovit 5000 cold curing resin from Heraeus Kulzer is stated to be well conductive, and was therefore deemed to fit the application. In the first attempt, the sample was clamped in a plastic support to keep it upright and placed in a cylindrical casting mold. Following the specifications in the datasheet, approximately 16 grams of the Technovit resin was mixed and poured into the mold. After the resin had hardened, the mold was removed, and the epoxy was ground away with a 120 grit wet sanding paper until both the front and back sides of the sample were visible. The front of the embedded sample was further polished with incrementally finer grit wet sanding paper, ending with P1200 which has a mean grain size of 15.3 µm. The embedded sample was then glued to the Multiprep chuck and polished with diamond films as explained above. In the subsequent SSRM experiment no electrical contact could be made, and this raised a question about the actual conductivity of the epoxy resin. Measuring its resistance with a multimeter revealed that it was in fact not conducting at all[2], and so an alternative way of providing contact through the epoxy had to be found.

[2]It was found that the liquid component of the resin was two years outside the expiry date, and this is expected to be the cause of the lack of conductivity.

The first attempt at providing a separate current path through the resin followed the procedure just described, but with a brass sample holder in place of the plastic one used previously. To ensure good contact to the chuck of the microscope, the back side of the epoxy was ground down until the sample holder was visible and glued to a piece of aluminium with a conductive glue. This gave adequate contact through the resin, but it was evident that the sample edges were still quite rough, even after polishing. Examining the edge in a scanning electron microscope even showed signs of the edge flaking off in some areas. It was assumed that this had happened during polishing, hence a way of protecting the edge was sought.

To protect the sample edge, two approaches were tested. Both consisted of placing the sample face down on top of a similar sized piece of aluminium before mounting it in the sample holder. In addition to protection, the aluminium also provided the wanted current path through the resin. In one experiment a layer of conductive glue was applied between the sample and aluminium, while in the other the sample and aluminium were in direct contact with no glue in between. After embedding in the epoxy resin, the back side of each sample was ground down until the aluminium piece was visible. The front side was ground with wet sanding paper and polished with the Multiprep as described earlier. Finally a second piece of aluminium was glued to the exposed aluminium slab on the back side for secure contact to the AFM chuck. This process is illustrated in figure 4.6. An EDS analysis of the glued sample showed that silver particles from the glue had been smeared out to partly cover the edge of the sample. The sample mounted without glue did not have this problem, and an SEM examination showed that the edge was still in good condition. The approach of protecting the sample with a slab of aluminium prior to epoxy embedding was thus adopted as the standard procedure for the subsequent samples.

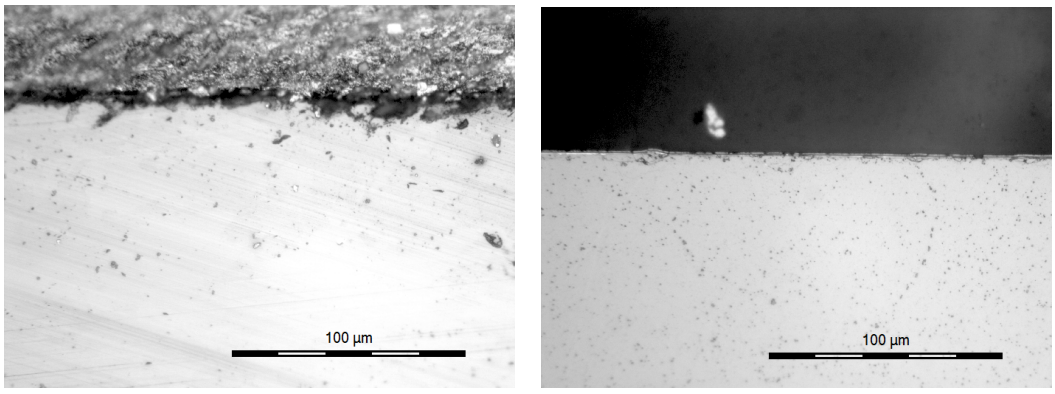

(a) **(b)**

Figure 4.7: *Light micrographs of samples polished with diamond films (a) and polishing cloths with diamond particle sprays (b). In both images the sample is seen at the bottom, while protective Al slab is seen at the top. In (a) the sample was glued to the aluminium piece, while in (b) no glue was applied. It can be seen that the edge in (a) is substantially rougher than the one in (b).*

Although providing a vast improvement over the unpolished samples, the Multiprep process still had two significant issues. Although other authors [53] state that each polishing step should take less than a minute, this could not be replicated here and the process was found to be time consuming. More importantly, if the lapping films were not in perfect condition and free from any debris, severe scratching of the samples would result.

To test an alternative approach, a sample was embedded in the Technovit 5000 resin and initially prepared with abrasive paper as before. Instead of using the lapping films, polishing proceeded on a Struers DAP-V turntable with Struers DP-Suspension diamond particle sprays of 6, 3, 1, and 0.25 µm particle sizes. The 6 and 3 µm sprays were used with MD-Dur polishing cloths, the 1 µm spray was used with an MD-Mol cloth, while the 0.25 µm spray was used on an MD-Nap polishing cloth. On all cloths Struers DP-Lubricant Green was used for lubrication and cooling. This polishing process was found to be significantly quicker than using the Multiprep, and the result also appeared to be better. Figure 4.7 shows a comparison of the results of the two processes where it can be seen that the polishing cloths apparently produces both fewer scratches and a smoother sample edge.

Table 4.4: *Comparison of sample preparation process and corresponding average RMS roughness. The polishing procedure is given in the parentheses.*

Sample	Details	$\langle R_q \rangle$ [nm]
R3p1	R3 sample glued to Al slab (lapping films)	3.4
R3p2	R3 sample without glue between sample and Al slab (slurry)	21.2
R3p4	R3 sample glued to Al slab (slurry)	10.7
R1u	Unpolished R1 sample	75.2

To quantitatively compare the two polishing procedures, tapping mode AFM images were taken of four different samples and their RMS roughnesses were computed in the Nanoscope Analysis 1.40 software. The RMS roughness, R_q, was calculated as

$$R_q = \sqrt{\frac{\sum z_i^2}{N}}$$

where z_i is the deviation of the height of point i from the mean plane of the entire image, and N is the number of points evaluated. On each sample R_q was determined at three different locations and the average of these three values, denoted $\langle R_q \rangle$, is listed in Table 4.4 along with the sample specifics. For all measurements, the scan size was $1 \times 1\,\mu m^2$ and the resolution was set to 256 samples per line. The scans were performed in locations which would be suitable for SSRM measurements, *i.e.* seemingly flat regions close to the sample edge. The scans were, however, conducted on the substrate rather than on the films to avoid being influenced by the different hardness of the various films. As expected, the unpolished sample showed the highest roughness, but surprisingly the best sample was the one polished with lapping films. Even though it appears more scratched under the light microscope, the RMS roughness is better than the best slurry polished sample by about a factor three. The discrepancy between appearance and measurements is expected to be caused by that the roughness measurements are performed in very small areas which may be located between the observed scratches.

Comparing the two slurry polished samples, the one with glue between the sample and aluminium slab has twice the roughness of the one without glue. This is expected to be caused by glue particles left on the surface after polishing. Why this is not seen in the glued sample polished with lapping films is not known.

With a polishing procedure similar to the lapping film process explained here, Eyben [53] achieved an RMS roughness of 0.2–0.3 nm. The one order of magnitude improvement over the results obtained here can, at least partially, be attributed to that while a 0.25 µm diamond film was used in the final step here, Eyben used a 0.05 µm aluminium oxide film for the final step.

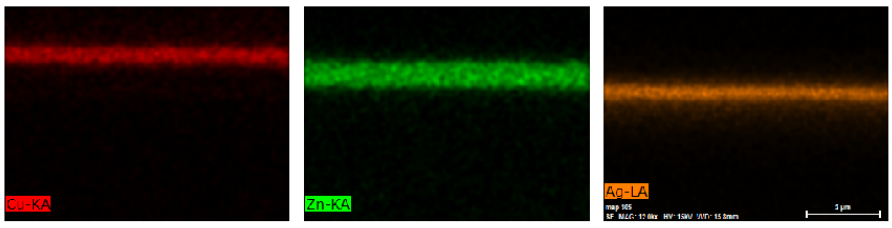

Figure 4.8: *EDS map of a polished R3 sample. Copper is represented in red, zinc in green, and silver in orange.*

A concern with the polishing scheme was that it would cause smearing of the films making it impossible to detect any interfaces. To investigate whether this would be an issue, a high resolution EDS analysis was conducted on a polished R3 sample. As can be seen in figure 4.8 the interfaces between the copper, zinc oxide, and silver films are all sharp, proving that no significant smearing of the films has taken place.

A resistance profile of an R3 sample cleaved and polished according to the described procedure is shown in figure 4.9. Each individual film is easily recognized, demonstrating the applicability of

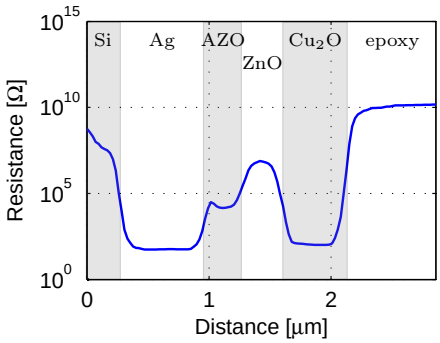

Figure 4.9: *Averaged resistance profile of a polished R3 sample.*

SSRM to samples of this geometry and material system. From left to right, the resistance levels correspond to the silicon substrate, silver, AZO, ZnO, Cu_2O and finally epoxy. It is again found that the cuprous oxide is indicated as having a resistance almost as low as that of silver, and this will be discussed in section 5.3.

Sapphire Substrates

Following the successful polishing of silicon substrates with cloths and diamond slurry, the initial preparation experiments on sapphire substrates were also conducted with this technique. As for silicon, the sapphire sample was aligned face to face with a slab of aluminium and embedded in Technovit 5000 resin prior to polishing. It was however quickly found that the considerable difference in hardness between the sapphire and the deposited films caused the films to be polished at a far higher rate than the substrate. The resulting bowing of the sample rendered ensuing SPM measurements difficult and no sensible results could be obtained.

The Multiprep tripod polisher which was tried on the silicon samples places a more uniform load on the sample surface than can be obtained manually, and the lapping films are also flatter than the polishing cloths. Hence, it was investigated whether this could be a viable alternative for sapphire samples. Initial experiments revealed that the Multiprep was indeed capable of polishing the sample without causing appreciable bowing, but as expected the process was time consuming. To speed up the polishing process, as much as possible of the epoxy resin was cut away with a hacksaw prior to the initial polishing step. The majority of the epoxy is required only to embed the brass sample holder (as explained in the silicon section), and very little is required for embedding the actual sample. To permit the removal of more of the epoxy, the use of the brass sample holder was discontinued and the samples were held upright in the casting mold by attaching them to the base of the mold with a strip of double sided tape.

It was seen that the Multiprep process left the edge of the sample quite rough, even when protecting it with a slab of aluminium. This is critical as the edge, where the films are deposited, is really the only interesting part of the sample. It was questioned whether the polishing could cause particles from the aluminium slab to break off and damage the sample edge. As the edge of the sample facing the Al-slab was most often in a better state than the edge facing away from the slab, it was however concluded that the Al had an overall positive effect.

The Technovit 5000 resin is known to have sub-optimal adhesion to surfaces, hence two alternative resins, Epofix and DuroCit, both manufactured by Struers, were tested. The former is a slow setting epoxy with excellent adhesion, while the latter is a hard acrylic with alumina particles, engineered for optimized edge retention [96]. It was also investigated whether gluing the sample to the protecting slab with a commercially available two component epoxy prior to embedding in the resin would improve the state of the edge. Figure 4.10 shows optical micrographs of the results of five different sample preparation routines. Samples (a–d) were all polished with lapping films, while sample (e) was polished with polishing cloths. As it can be observed, the cloths caused severe bowing of the edge area, a feature not seen on any of the film polished samples. Further, in (a) the sample was protected by an Al slab as explained for Si samples, and embedded in Technovit 5000. The same was done in (b), but here the resin was replaced by Epofix. Sample (c) was also embedded in Epofix, but the edge protection was here taken care of by a sapphire dummy

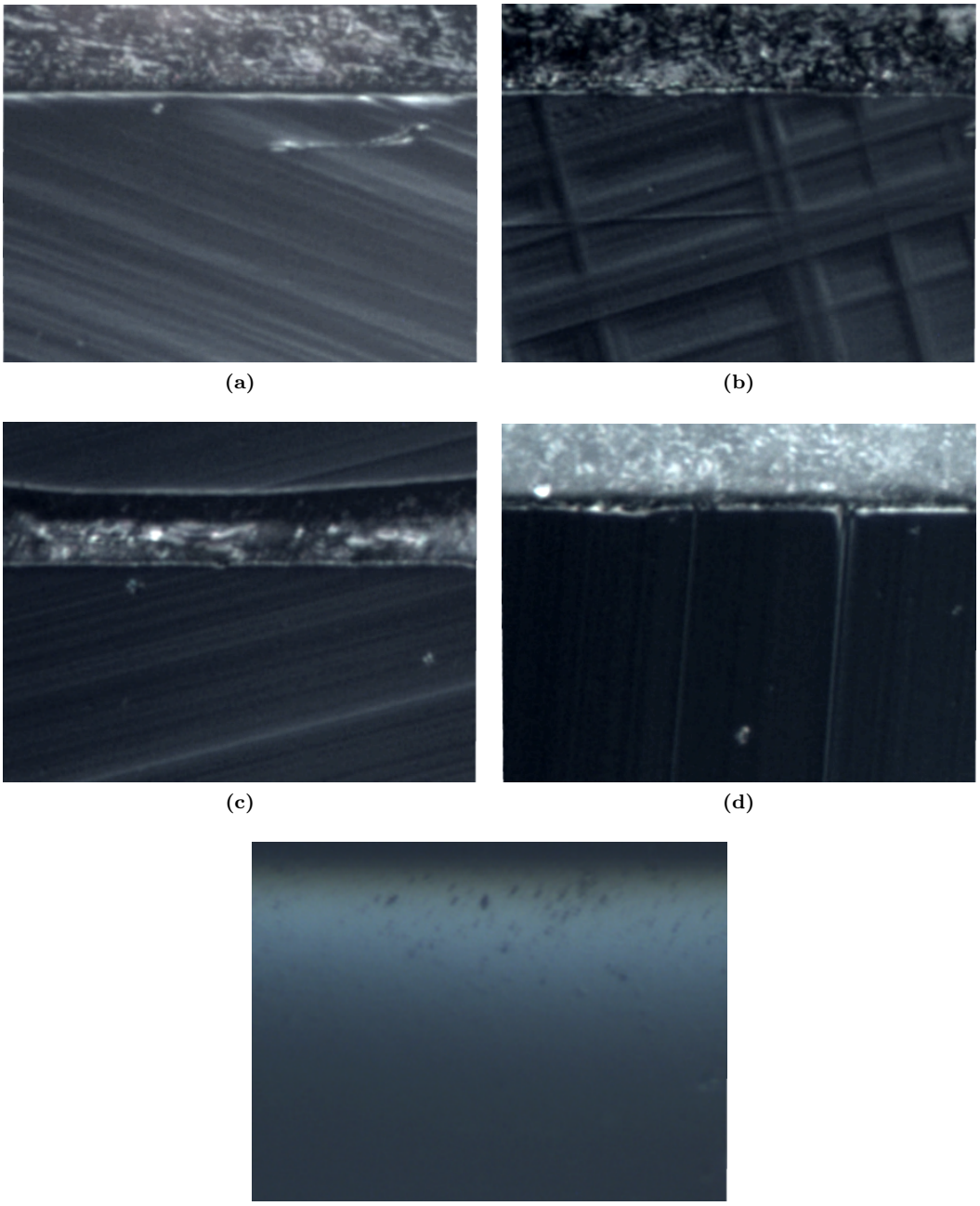

(a) **(b)** **(c)** **(d)** **(e)**

Figure 4.10: *Optical micrographs of an about 120 µm wide area of the edge on five mechanically polished sapphire samples. In all images, the sample is seen at the bottom while the resin can be seen at the top. In (c) the protective specimen is seen at the very top.*

substrate. A two-component epoxy was used to glue the two samples to each other. Finally, in (d) an unprotected sample was embedded in DuroCit.

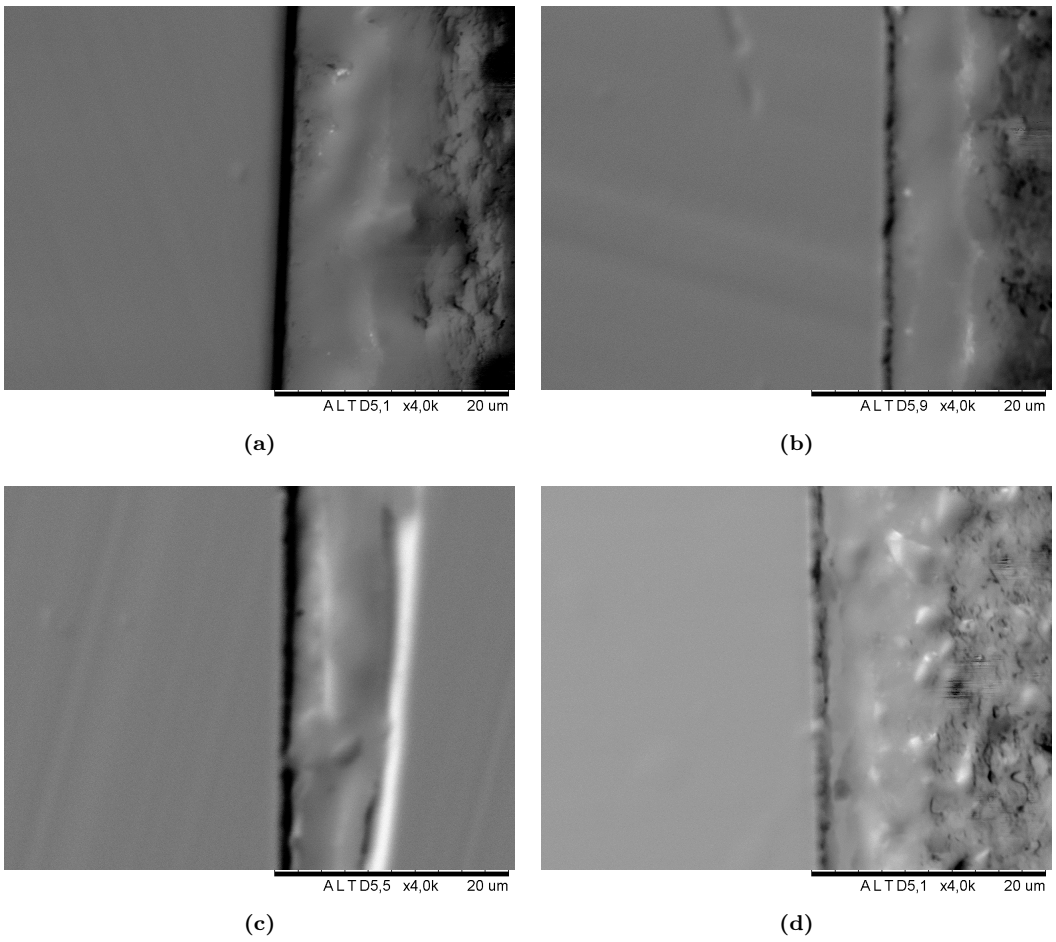

Figure 4.11: *Scanning electron micrographs of mechanically polished sapphire samples. In each panel, the sample is seen to the left while the protective slab is on the right.*

The optical microscope is insufficient for comparing the quality of the sample edge in cases (a)–(d), hence scanning electron micrographs were taken. The results are shown in figure 4.11, where each panel corresponds to the same sample as in figure 4.10 (figure 4.10a shows the same sample as 4.11a, etc.). From the SEM images, it appears that the processing of the samples of panels (a) and (c) gives a less damaged sample edge than in the other two cases. Panel (a) however gives the impression of a slight bowing of the sample edge which is not seen in (c), and this suggests that Epofix epoxy and protection by a second piece of sapphire is the optimal solution.

Unfortunately, neither the sample in figure (c) nor any of the other mechanically polished sapphire samples have provided significant contrast in SSRM experiments. The discrepancy between SEM and SSRM is expected to be caused by the simple scanning electron microscope used here having insufficient resolution to reveal the finer details of the edge.

From this study it was concluded that mechanical polishing of sapphire is not viable as a sample preparation routine for SPM, hence an alternative procedure had to be found.

Zinc Oxide Substrates

The typical zinc oxide substrate is grown along the crystallographic c-axis ([0 0 0 1]), which implies that the earlier described cleavage procedure should produce a very flat cross section. While this holds true in some cases, the result is strongly dependent on the processing history of the sample. In samples with flat as-cleaved cross sections, no further preparation or cleaning is required. However,

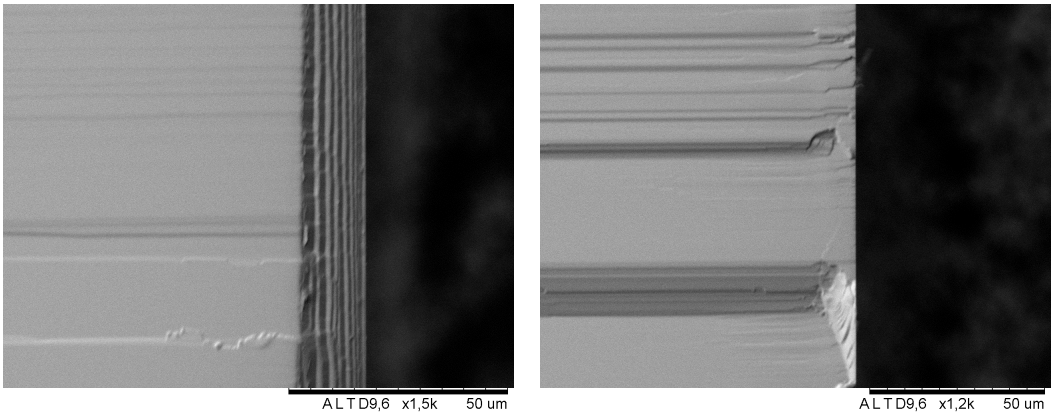

(a) **(b)**

Figure 4.12: *Scanning electron micrographs of two areas of the edge of a ZnO sample after cleaving. In (a) a staircase-like structure has formed, while in (b) no steps are formed. In both (a) and (b) grooves can be seen running perpendicular to the sample edge.*

in some cases the cleaving produces a stepped edge rather than a perfect 90° angle, as illustrated in figure 4.12. As the sample edge is most often the area of interest, determining the state of the edge, by for instance scanning electron microscopy, prior to SSRM is recommended. Cleaving also tends to leave grooves perpendicular to the sample edge (parallel to the c-axis) but these are rarely an issue in SSRM experiments as they are readily identified and can be avoided when setting up the experiment. In cases where the synthesis or prior experimental work has severely damaged the crystal structure, the as-cleaved cross section may be too rough for scanning probe microscopy. For these samples, further processing in the form of polishing is required.

Based on the experience gained from preparing the silicon and sapphire substrates, several experiments were conducted on zinc oxide dummy samples. To examine the effect of edge protection and choice of resin, three different sample arrangements were embedded in both Epofix and DuroCit. The arrangements were (i) an unprotected sample, (ii) a sample protected with an Al-slab, and (iii) a sample protected by a ZnO substrate. After the resins had hardened, each sample was ground and polished with diamond slurry as explained for the silicon samples. Unfortunately, the unprotected ZnO in epofix was damaged during removal from the casting mold and was not processed further.

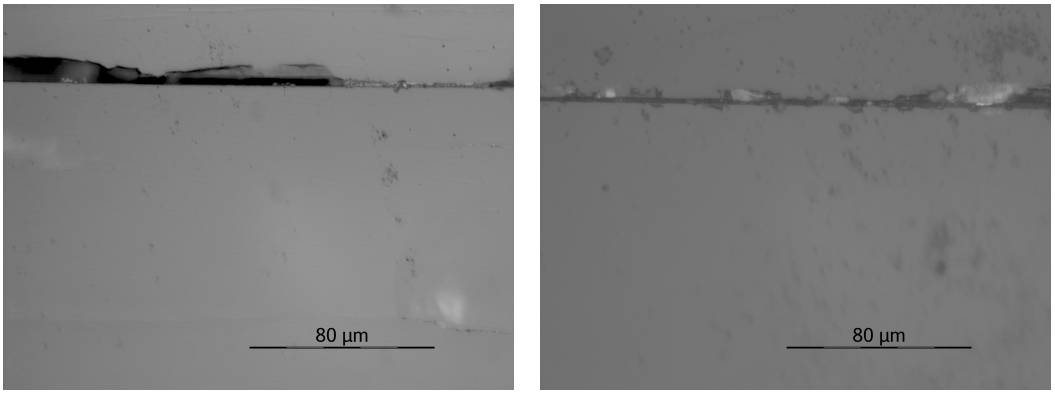

(a) **(b)**

Figure 4.13: *Optical micrographs of zinc oxide samples protected by zinc oxide. (a) is cast in Epofix while (b) is cast in DuroCit, and both were polished with cloths and diamond slurry prior to imaging. The lower part of the image shows the sample of interest, while the upper part shows the protective specimen.*

An examination under an optical microscope revealed that the sample edge was less damaged when cast in Epofix than in DuroCit regardless of protection method. It is expected that this is

caused by the relatively low hardness of the Epofix being the closest match to that of the zinc oxide. Figure 4.13 illustrates the point by showing a sample protected by ZnO embedded in (a) Epofix and (b) DuroCit.

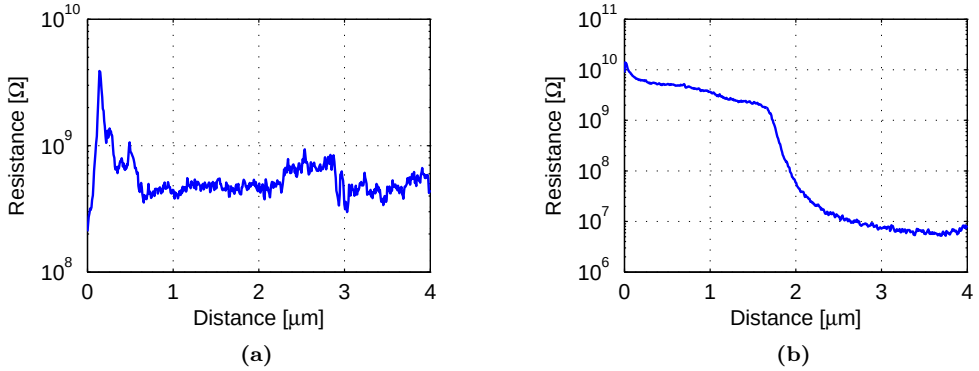

Figure 4.14: *Average resistance profiles of an as-cleaved (a) and polished (b) zinc oxide sample with in-diffused aluminium. The sample edge is situated outside the right edge of the plots, and the electrical activity of the in-diffused species can be seen in the polished sample.*

The practical applicability of this polishing routine was immediately obvious, as it enabled an SSRM experiment to be successfully conducted on an in-diffused zinc oxide sample which had yielded no results in past experiments due to the too rough as-cleaved cross section. Average resistance plots of the as-cleaved and post-polishing SSRM measurements are shown in figure 4.14. While the as-cleaved sample gives no usable information, the polished sample displays a smooth profile which closely follows the chemical profile acquired by SIMS.

An interesting feature of this sample, which has also been recognized in other polished ZnO samples, is that the scratches left from the polishing show up in the SSRM plots, as shown in figure 4.15. This may either be an artifact resulting from the probe losing contact as it passes the scratches, or alternatively the polishing might have altered the microstructure of the sample in the scratches causing an increased resistivity.

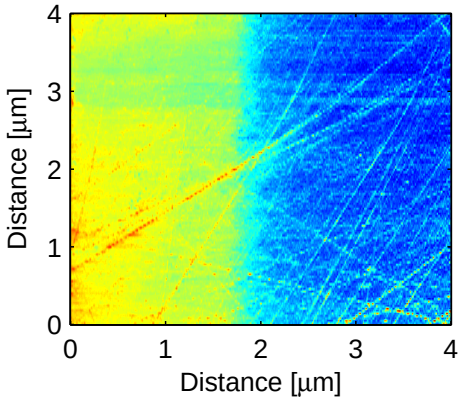

Figure 4.15: *SSRM data for a polished zinc oxide sample. Scratches left from the polishing are readily observable.*

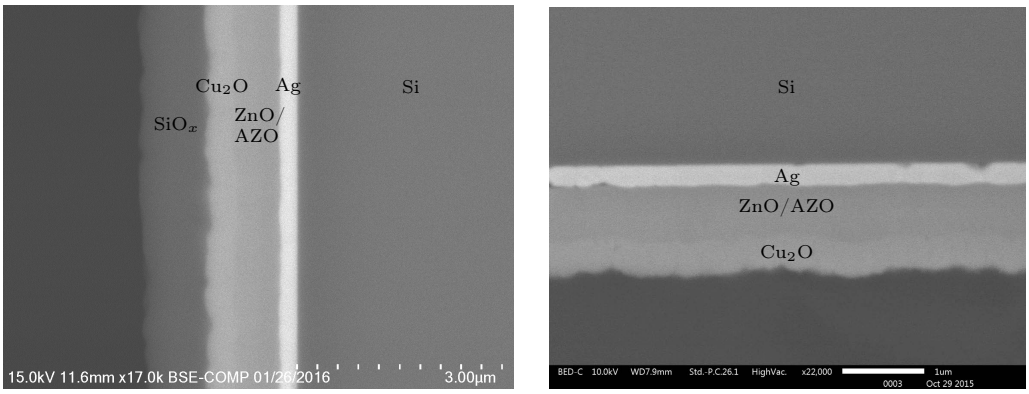

(a) **(b)**

Figure 4.16: *Backscattered electron SEM micrographs of the R3 sample polished with (a) the Hitachi IM4000, and (b) the JEOL CP. In (a) the sample edge faces towards the left, while in (b) it faces towards the bottom of the image. (a) courtesy of Muhammad Tayyib, University College of Southeast Norway, (b) courtesy of JEOL.*

4.6.3 Ion Milling

As an alternative to the fairly labor intensive manual polishing processes detailed above, two ion milling machines were tested to see whether they could prepare samples suitable for SPM. One R3 sample was sent off to JEOL for polishing on their JEOL CP cross sectional polisher, while a second sample of the same geometry was taken to the University College of Southeast Norway for polishing on their Hitachi IM4000 ion mill. The settings used on the IM4000 were an accelerating voltage of 6 kV, a discharge voltage of 1.5 kV, and an angle of rotation of 30°. No sample cooling was available hence milling took place at room temperature.

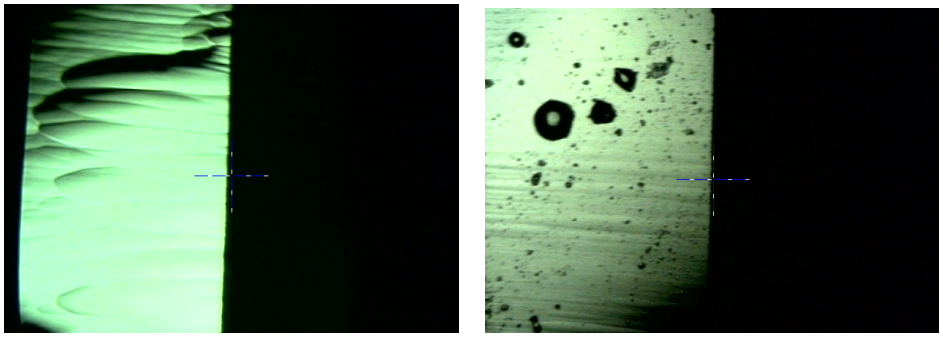

(a) **(b)**

Figure 4.17: *Light micrographs of the sample polished with (a) the Hitachi IM4000, and (b) the JEOL CP. Both taken with the light microscope on the Dimension 3100. In (a), the entire sample width ($\sim 500\,\mu$m) is visible, while in (b) the left edge of the cross section is just outside the edge of the picture. In both images, the films are deposited on the sample edge facing towards the right.*

Scanning electron micrographs of the results are shown in figure 4.16. In both images the substrate and the Ag, Cu_2O, and ZnO films are discernible. Not surprisingly, no difference can be observed between the ZnO and AZO films. EDS maps (not shown), however, clearly indicate the presence of Al in part of the ZnO film. From EDS it has also been identified that a layer with a high concentration of silicon and a significant oxygen content has formed on the surface. The exact composition of this layer has not been investigated, but it is in any case an undesired effect. From these images, ion milling anyhow seems like a good solution. The images taken with the optical microscope on the Dimension 3100, shown in figure 4.17, however reveal topographical features not seen in the SEM. In figure 4.17a rather large bulge-like features can be seen, while in 4.17b smaller bulges and quite substantial amounts of particles are left from the polishing. SSRM

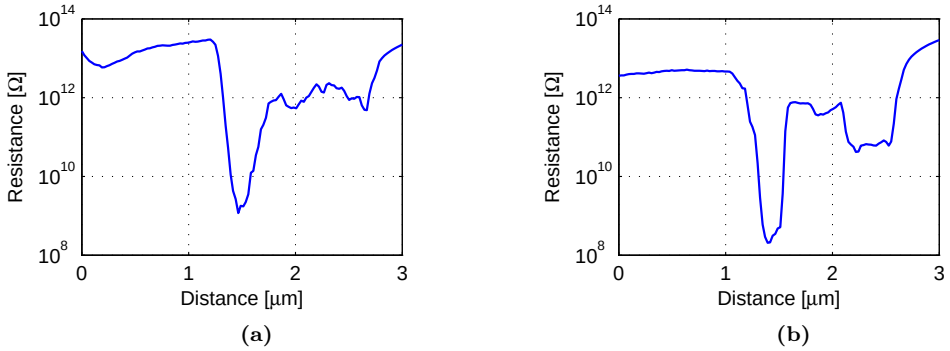

Figure 4.18: *Averaged resistance plots of two successive SSRM scans in the same area of an ion milled R3 sample.*

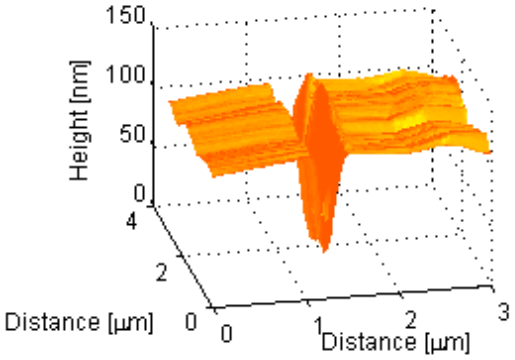

Figure 4.19: *3d representation of the topography data acquired during SSRM on the Hitachi-polished R3 sample.*

experiments have been conducted on both samples, but neither have yielded satisfactory results.

During the SSRM measurements on the sample polished on the IM-4000 it was found that if two successive scans were made in the samea area, the latter scan yielded better contact and less noise than the first. This is not seen with the manually polished samples, and correlates well with the theory that the ion milling process leaves behind a somewhat damaged surface layer. Figure 4.18 shows averaged resistance profiles of two consecutive scans which should both ideally be similar to figure 4.9.

In figure 4.19, the topography data captured during an SSRM experiment on the sample polished with the IM-4000 is presented. Here, the sharp groove is the silver film, which has obviously been removed to a far greater extent than the surrounding silicon and zinc oxide layers. The reason is unknown, but it is possible that it is related to the heating of the sample by the ion beam during milling. If this is indeed the case, cooling the sample with *e.g.* nitrogen during processing may be beneficial.

From the optical images, topography data, and resistance profiles it is concluded that ion milling is not suitable for preparing silicon samples for electrical SPM techniques, at least not with the current parameters and procedure. It is likely that better results could be achieved by optimizing the procedure, but this was not pursued further as the mechanical polishing process was already developed.

For sapphire substrates on the other hand, no satisfactory mechanical polishing route was found, hence it was questioned whether ion milling could be an option for this material. A sapphire substrate with a stack consisting of epitaxially grown ZnO and magnesium zinc oxide (MgZnO) capped by thermally evaporated Ag was brought to the University College of Southeast Norway and polished on the IM4000. To reduce the ion dose of the films the sample was milled backwards,

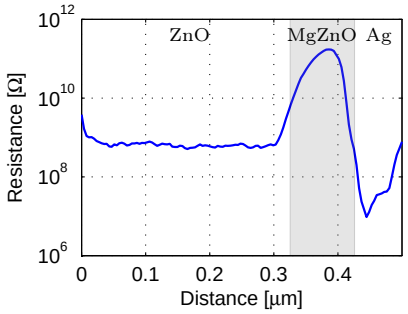

Figure 4.20: *Average resistance profile of an ion milled thin film stack on sapphire substrate. The increased resistance towards the edges of the measurement is expected to be caused by a poor electrical contact when the probe reverses direction.*

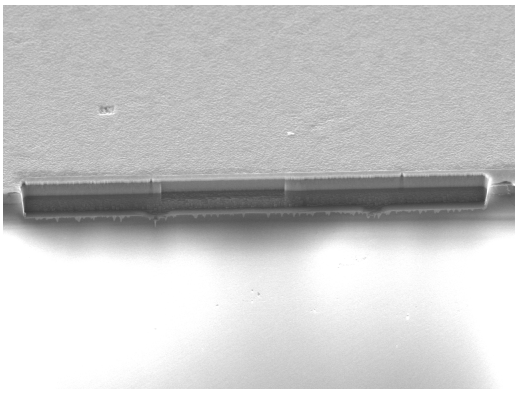

Figure 4.21: *SEM micrograph taken after the final step of the FIB polishing. The total width of the polished area is approximately 100 µm and the image is taken at an angle such that the top surface of the sample is seen above the polished region and the cross section is seen below it.*

i.e. the ion beam was incident on the back side of the substrate rather than on the topmost film. Apart from this, the setup and parameters were identical to the ones used with the silicon sample, leading to an effective polishing time of around 6 hours before the ion beam had penetrated the entire cross section. After ion milling no further preparation was done to the sample before scanning spreading resistance microscopy. The results were superior to the ones obtained from the mechanically polished samples and each film could be successfully discriminated as shown in figure 4.20. From left to right the resistance levels correspond to zinc oxide, MgZnO, and silver.

4.6.4 Focused Ion Beam

Focused ion beam (FIB) was not expected to be suitable for polishing SPM samples due to its low milling rate. However, as a FIB machine was available an attempt was made on a sapphire sample. The sample had a silver film as the topmost layer, and this was expected to protect the structure beneath from the ion beam. For further protection, 300 nm of carbon was deposited just inside of the area to be polished. In FIB terms, a large area of 100 µm wide by 10 µm deep, was polished in four stages. The former two were dedicated to sample removal and were conducted with a beam current of 10 nA. The latter two steps were conducted for fine polishing of the central region of the already polished area. For these steps, the sample was tilted, and the beam current was reduced to 0.1 nA. For each step gallium ions were used, and the accelerating voltage was 30 kV. The accumulated dose after the final step was around 50 nC/µm^2.

The scanning electron micrograph of figure 4.21 shows the state of the sample edge after the final stage of the polishing, and it seems that the edge is well polished. As expected, though, the polished area was too small to be located by the optical microscope on the Dimension 3100, so no successful SPM measurements could be carried out.

Chapter 5

Applications in ZnO Research Structures

Three kinds of thin film structures have been examined during the course of this project. These are (i) in-diffused samples, (ii) ion implanted samples, and (iii) heterostructures, as elaborated in the following sections. These structures have been chosen due to their relevance both in applications and in ongoing research projects. The in-diffused and implanted samples are subjects of other master's and PhD projects and it should be emphasized that, apart from SSRM, SCM, and related preparation, all experiments described on these samples have been performed by other staff and students. Those experiments are described here only for context and correlation purposes.

As SSRM and SCM rely on the physical interaction between the probe and the sample, there is always a risk of breaking the probe if scanning across the edge. For this reason, one tries to avoid the edge during measurements and this induces a degree of uncertainty in the location of the scanned area. For measurements where this is relevant, an estimate of the distance to the edge is provided, but this should not be considered as an absolute measure.

5.1 Electrical Properties of In-Diffused Elements in Bulk ZnO

In-diffusion of foreign species is a process of fundamental interest for any substrate material for several reasons. Not only is this one of the key doping processes employed in device fabrication, but the electrical behaviour of the dopants is essential in understanding the interplay of crystallographic defects.

Diffusion has not yet been widely studied in zinc oxide, but from other substrate materials it is well known that vacancy- and interstitial mediation are common diffusion mechanisms. By modelling and experiments it has recently been shown that the diffusion of aluminium proceeds through complexes of interstitial aluminium and zinc vacancies (Al_{Zn}-v_{Zn}) [27]. This is rational as Al is a donor and v_{Zn} is positive, thereby causing a coulombic attraction between the two. For acceptor dopants, such as copper, less is known about the diffusion mechanism.

In currently running research projects the behaviour of various in-diffused acceptor and donor dopants in zinc oxide are investigated. The approach is to deposit a thin film of highly doped ZnO on top of a nominally undoped substrate. A subsequent annealing step lets the dopants diffuse from the film into the substrate before the diffusion profile is chemically characterized using secondary ion mass spectrometry (SIMS). SIMS does however not give any insight into the electrical properties of the in-diffused region. These properties are of utmost importance, and may reveal information about site selectivity of the dopant species, as well as their interplay with defects. To microscopically characterize the resistance and capacitance distributions, SSRM and SCM have been conducted on three such samples, one with in-diffused copper, one with gallium, and one with aluminium as parts of the characterization schemes. The three cases are elaborated in the following sections, respectively.

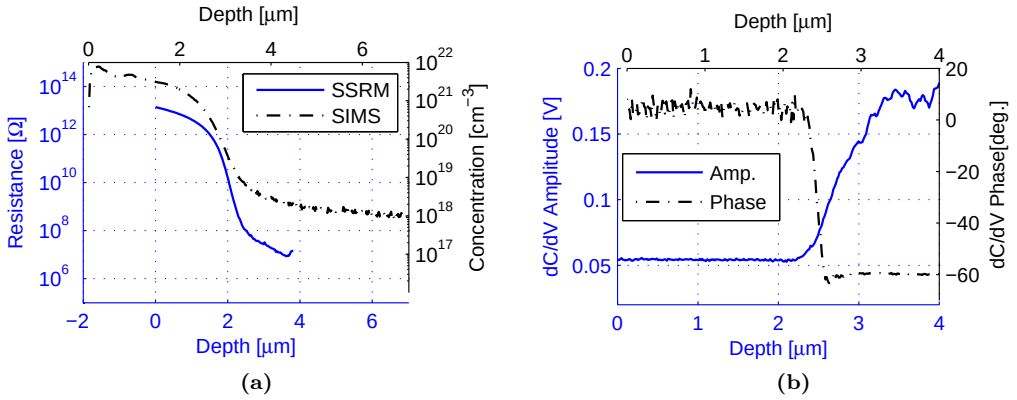

Figure 5.1: *(a) Average resistance and Cu concentration after diffusion into ZnO as measured by SSRM and SIMS, respectively. The SSRM profile has been shifted to the right by ∼ 2 µm to correlate with the SIMS profile. (b) Averaged SCM amplitude and phase. SIMS data courtesy of Eva H. Enoksen [97].*

5.1.1 Copper Diffusion in Zinc Oxide

Background

In the continuous effort to synthesize p-type zinc oxide, a masters project [97] targets the understanding of diffusion of copper in ZnO. Earlier work has narrowed the list of possible diffusion mechanisms down to (i) diffusion through zinc vacancies or (ii) diffusion through interstitial positions. It has also been concluded that in case (i) the copper atoms will act as acceptors and be negatively charged (Cu^-), while in case (ii) they will act as donors and carry positive charge (Cu^+) [98]. In a natively n-type substrate such as ZnO, mechanism (i) will thus result in a higher resistance while the opposite is true for case (ii), following (2.14).

An additional question was whether experimental evidence of copper diffusing into the substrate in concentrations exceeding the solid solubility, resulting in the formation of precipitates as theoretically predicted by Gallino [99], could be obtained.

Experiments

In an attempt to answer these questions, a copper doped zinc oxide film was deposited on top of a commercial (Tokyo Denpa) zinc oxide substrate. After annealing at 1000°C for 30 minutes secondary ion mass spectrometry was conducted, yielding the results shown in figure 5.1a. Subsequently, the sample was manually cleaved and SSRM was done on the freshly exposed cross section. The sample was scanned over a 4×4 µm area at a scan rate of 0.25 lines/s with a bias of 0.5 V applied to the sample relative to the probe. The resulting average resistance profile is shown along with the SIMS results in figure 5.1a. The sample edge is located some hundred nanometres to the left of the start of the SSRM curve.

To complement the findings from SSRM a scanning capacitance measurement was carried out. This was performed with a DC bias of −0.5 V applied to the sample, while the AC excitation signal had a magnitude of 4 V and a frequency of 70 kHz. Plots of the averaged SCM amplitude and phase are shown in figure 5.1b.

Results and Discussion

The initial ∼ 1 µm of the SIMS profile is the remaining film, while the rest shows the in-diffused copper. The extremely high concentration of copper close to the surface alone strongly suggests that some form of precipitation has taken place.

As can be seen from the SSRM profile, the resistance is significantly higher close to the sample edge than in the bulk. Although it cannot be extracted whether this is caused predominantly by copper atoms in the ZnO structure or by precipitates, it *can* be concluded that if interstitial copper is present, its influence is severely outweighed by substitutional impurities and/or precipitates. It can also be seen that the SSRM curve closely follows that of the chemical profile.

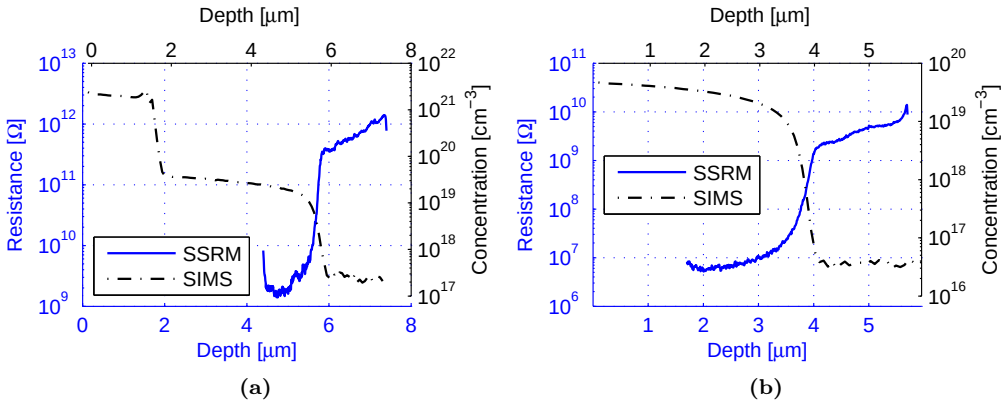

(a) (b)

Figure 5.2: *(a) SIMS and SSRM profiles for Ga in-diffused in ZnO and subsequently annealed at 950° C for 5 hours. The increased resistance towards the left of the curve is an artifact, probably resulting from the probe momentarily losing contact with the sample as it reverses direction. (b) SIMS and SSRM profiles for Al in-diffused in ZnO and annealed at 1200° C for 3 hours. The increase in resistance on the far left of the SSRM curve in (a) and the far right in (b) is again most likely an artifact which results from the probe losing contact with the sample when it reverses direction. SIMS measurements courtesy of Thomas N. Sky.*

The SCM profiles in figure 5.1b provide additional interesting information. The lower amplitude signal in the in-diffused region should normally signify a higher concentration of charge carriers here than in the bulk, but since the resistance measured by SSRM is higher in this region this can not be true. This may be explained by the introduced copper either in some way obstructing the depletion of electrons, or that the concentration of mobile electrons is reduced to a level close to the detection limit of the capacitance sensor. Interestingly, the phase signal shows an approximately 60° change in the diffused area relative to the bulk value. This may indicate that the in-diffused region is less n-type than the bulk of the sample, but since the phase is far smaller than 180° it has not become p-type. A similar result is reported by Børseth *et al.* for ion implanted antimony, which was also expected to act as an acceptor in ZnO [100].

No signs of precipitates were observed with SSRM or SCM, suggesting that the possible inclusions are either too small to be detected by these techniques or that they have resistance and capacitance characteristics similar to the surrounding matrix.

5.1.2 Donor Diffusion in Zinc Oxide

Background

Continuous research is conducted towards replacing the expensive and environmentally harmful indium tin oxide (ITO) by ZnO for applications as transparent conductive oxides (TCOs) in display technology and solar cells. The main drawback of ZnO over ITO is the reduced conductivity, so understanding the processes governing donor doping is a key goal. From earlier work [27] it is known that aluminium diffuses in zinc oxide through zinc vacancies in accordance with Fair's vacancy model. In an effort to increase the general understanding of ZnO, and in particular diffusion of common donor species and their interplay with defects, zinc oxide substrates were annealed at various temperatures after being sputter coated with a 1.5 µm thick film of gallium doped ZnO. Subsequently, the distribution of gallium atoms, zinc vacancies, and complexes thereof were studied with SIMS, positron annihilation spectroscopy (PAS), and electron paramagnetic resonance (EPR), respectively. However, the electrical properties in the in-diffused region had not been confirmed. For comparison, the same process was done with samples with in-diffused aluminium.

Experiments

To gain insight into the resistance distribution around the diffusion front, SSRM was conducted on one sample with in-diffused Ga (annealed at 950°C for 5 hours) and one with Al (annealed at 1200°C for 3 hours). For the Ga sample, a bias voltage of 1 V was applied to the sample with

respect to the probe, and the scan was conducted over an area of $3 \times 3\,\mu m$. The sample with Al was examined with a bias of 1.5 V, and the area was $4 \times 4\,\mu m$. In both experiments the scanning was performed at a frequency of 0.25 lines/s and the same doped diamond probe was used. SCM experiments were also attempted, but no contrast could be obtained.

Results and Discussion

Figure 5.2 shows averaged resistance profiles of the diffusion fronts of the Ga and Al doped ZnO samples plotted along with concentration profiles for the respective dopant species. In both plots, the resistance profile has a steep gradient between bulk on the right side and the in-diffused area on the left, with a slope that matches well with the SIMS profiles when plotted with the same length scale. It is seen that the introduced donors leads to a 2–3 orders of magnitude reduction in the resistance in both cases. The substrate for the Al-diffused sample is expected to have an intrinsic electron concentration of $\sim 10^{17}\,cm^{-3}$, which is in reasonable agreement with the chemical profile. This shows a dopant concentration on the order of $1 \times 10^{19}\,cm^{-3}$ in the in-diffused area, and assuming the dopants are fully activated, would then be expected to reduce the resistance by about two orders of magnitude..

The Ga-diffused sample was prepared on a highly resistive substrate, and it is somewhat surprising that the resistance decrease after diffusion is only by the same order of magnitude as for the Al-samples. The reason is expected to be that the processing of the sample has significantly reduced the bulk resistivity.

The reason for the lack of contrast in the SCM measurements on the Al-diffused sample could be an insufficiently rectifying tip-sample contact which prevents the depletion of electrons beneath the tip. This can be expected for such a highly doped sample. In the Ga-diffused sample it is not known why no contrast could be obtained, and gaining knowledge about the resistivity of the substrate after processing seems like a natural place to start elucidating this matter.

5.2 Ion Implantation of Group IV Elements in ZnO

As an alternative to aluminium and gallium, silicon and germanium are expected to be suitable shallow donors for zinc oxide. Although some publications exist, *e.g.* Schifano *et al.* [101], the behaviour of these elements in ZnO is far from fully understood. Both Si and Ge can be accurately introduced via ion implantation which is a common unit process in semiconductor device manufacturing. A technological disadvantage of this technique is that lattice damage is inevitable. For scientific purposes, however, this can be utilized in elucidating correlations between the introduced species and lattice healing during post-implant annealing. Silicon, for instance, has shown a remarkable resilience to damage accumulation and heals quickly upon annealing.

As the group IV elements are closer in size, valency, and electronegativity to oxygen than to zinc, one could argue that the implanted atoms would occupy sites on the O, rather than the Zn, sublattice. From experience with other impurities, *e.g.* antimony (Sb), however it is known that such simple reasoning does not necessarily hold and the impurity configuration must be experimentally verified for each element [102].

It is a known fact that the hydrothermal process used to grow zinc oxide substrates inevitably introduces a significant concentration of lithium. From [30] it is further established that lithium residing substitutionally on a zinc site (Li_{Zn}) acts as an acceptor and traps electrons. Lithium on an interstitial site (Li_i), on the other hand, acts as a donor. Since zinc oxide natively is an n-type semiconductor substitutional lithium decreases conductivity, while interstitial lithium increases the conductivity.

Azarov *et al.* [31] have demonstrated that the behaviour of native lithium after ion implantation in zinc oxide is strongly correlated with the preferred sublattice into which the implanted species incorporates. Implantation of species which take zinc sites have been found to cause depletion of lithium far beyond the projected range of the implantation. The reason is that the implantation causes an excess of zinc interstitials (Zn_i) which react with the substitutional lithium according to

$$Zn_i + Li_{Zn} \rightarrow Zn_{Zn} + Li_i.$$

The interstitial lithium is a fast diffuser which rapidly redistributes during implantation or annealing.

Conversely, implantation into oxygen sites results in a pile up of lithium around the projected range. The excess oxygen interstitials caused by the implantation does not promote ejection of Li from the Zn sites, but rather results in Li_{Zn}-O_i complexes [31].

Another related topic of scientific interest is the formation of precipitates and voids after ion implantation. It is known from literature that co-sputtering of zinc oxide and silicon may produce silicon nanoclusters in a ZnO matrix [103]. It is also established that voids and precipitates may result from ion implantation, but whether this occurs with group IV elements and how this might affect the electrical properties is not known [104, 105].

To elucidate the behaviour of silicon and germanium in ZnO, a masters project [106] is currently undertaking a holistic experimental investigation of structural, optical, and electrical properties of Si- and Ge-implanted zinc oxide. As part of the electrical characterization scheme, Hall effect measurements have been performed in the van der Pauw geometry. From these experiments it is, however, not known how much of the measured current has actually passed through the implanted area. In order to gain insight into the electrical activity of the implanted samples SSRM has therefore been conducted before and after isochronal post-implantation annealing at various temperatures.

5.2.1 Silicon Implanted Zinc Oxide

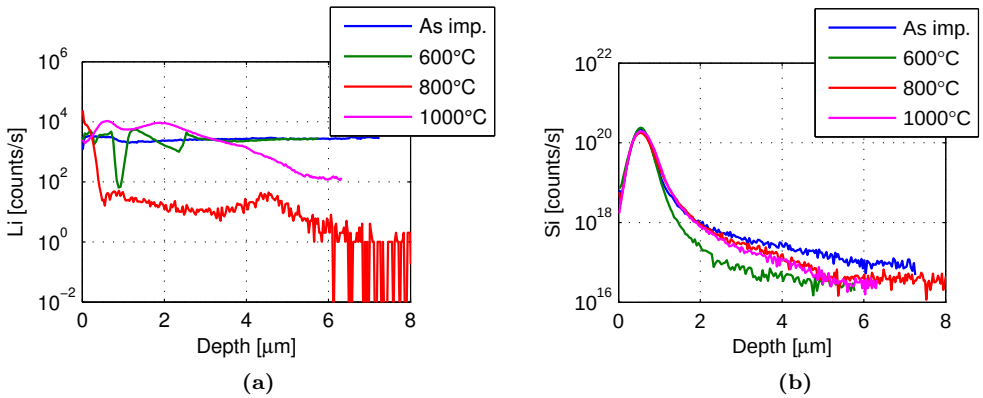

Figure 5.3: *Uncalibrated SIMS profiles of (a) lithium and (b) silicon in the silicon implanted samples. The erratic behaviour of the Li curve of the 800° C sample between 6 and 8 µm is caused by the lithium signal falling below the detection limit of the instrument. SIMS data courtesy of Bjørn Brevig Aarseth [106].*

Background

A dose of $10^{16}\,cm^{-2}$ silicon ions was implanted into four bulk ZnO samples at an energy of 375 keV, corresponding to a projected range of 450 nm. One of the samples was kept as implanted while the remaining three were annealed at temperatures of 600°C, 800°C, and 1000°C, respectively. The annealing time was 60 minutes for all samples.

To investigate the relationship between the impurity distribution identified by SIMS and the electronic characteristics, SSRM experiments were conducted.

Experiments

For the SSRM experiments, no sample preparation apart from manual cleaving was done, except in the case of the sample annealed at 1000°C. The as cleaved cross section on this sample was too rough to allow reliable measurements and it was hence polished according to the procedure described in the previous chapter. The other samples were glued to aluminium slabs with silver paste for contact to the microscope. It was found that a bias voltage of 4 V applied to the sample was necessary for stable contact to the unpolished samples, while 500 mV was sufficient for the polished one. The scanning was performed at 0.25 lines/second, and the same doped diamond probe was utilized for all samples.

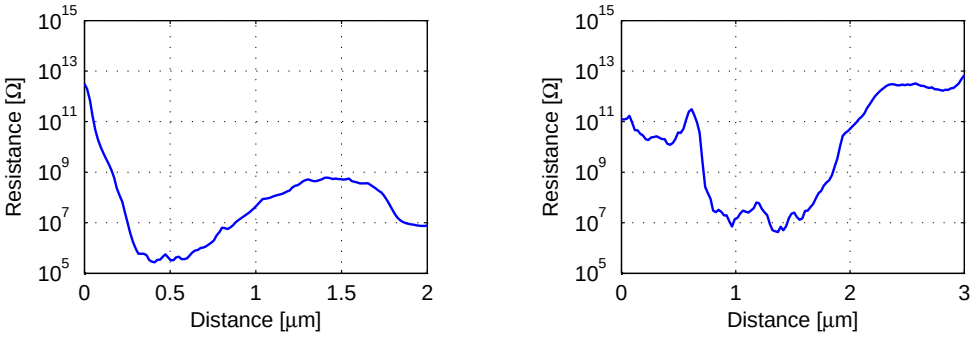

(a) *As implanted.* **(b)** *Annealed at 600° C.*

(c) *Annealed at 800° C.* **(d)** *Annealed at 1000° C.*

Figure 5.4: *Resistance profiles of silicon implanted zinc oxide samples. In all profiles, the sample edge is located 100–300 nm to the left of the plot.*

Results and Discussion

The results from the measurements are shown in figure 5.4 where the sample edge is located approximately 100–300 nm to the left of the plot in each case. In the as-implanted sample of figure 5.4a it is assumed that the highly resistive region close to the sample surface (far left in the plot) is due to lattice damage caused by the implantation process. Further into the sample, the dip in the resistance at about 0.5 µm is caused by the implanted silicon acting as a donor, while the increased resistance in the range 1–1.75 µm again may result from lattice damage caused by the implantation. The dip in resistance at the far right showed up in two out of three measurements and does not appear to be an artifact of the measurements. It is however not clear what exactly the origin of this decreased resistance may be.

After a 600°C anneal, the low resistance region has widened slightly and shifted further into the substrate. Also, the resistance below the low resistance region has increased. From the SIMS profiles in figure 5.3 it is seen that the depths at which this occurs correlates fairly well with a sharp dip in the lithium signal. In addition, the 600°C anneal is likely to have reduced the lattice damage to some degree, which should also contribute to the conductivity increase. From these measurements, the only apparent reason for the resistance increase beneath the low resistance region is the small accumulation of lithium seen in figure 5.4b.

In the sample annealed at 800°C, the resistance profile has the same general shape as in the as-implanted sample. However, the resistance peak correlated with the implantation damage is less pronounced. This may partly be due to further activation of silicon dopants, but it is also seen from the SIMS profile that the anneal has considerably reduced the concentration of lithium. Lithium acts mainly as an acceptor, and its removal significantly increases the carrier concentration [30]. Hence in this sample, the conductivity is no longer dominated by the implanted Si.

In figure 5.4d it can be seen that annealing at 1000°C gives a similar shape of the resistance distribution as the 800°C anneal, but the resistance is generally about two orders of magnitude higher throughout. A likely explanation is lithium returning both from bulk and from the surface, and this is supported by the SIMS measurement. An additional contribution stems from reduced mobility as evidenced by Hall effect measurements. From RBS experiments it was found that the crystal structure is more damaged in this sample than in the 800°C sample, and this explains the mobility decrease. The origin of the damage is expected to be the returning lithium forming defect complexes with the silicon dopants. These can compensate the donor action and thus explain the observed resistance increase. Several SSRM measurements were conducted along the sample edge, and it should be noted that not all measurements produced similar results to figure 5.4d. In some locations, the resistance decreased exponentially (linearly on a log-scale) from the edge down to a value of about $10^7\,\Omega$ at a distance of 1.5 µm into the sample, where it remained constant.

In summary, based on the behaviour of lithium and the resistance evolution, silicon implanted in ZnO has been found to exhibit donor behaviour. The low resistance around the implantation peak seen in the as-implanted and 600°C samples, signifying a high degree of dopant activation and little lattice damage, is unusual but correlates well with Hall effect and RBS measurements (not shown here).

5.2.2 Germanium Implanted Zinc Oxide

Background

Like for the silicon implantation, four ZnO samples were used for the germanium experiments. To achieve a similar projected range as for silicon (450 nm), Ge ions were implanted with an energy of 800 keV. The dose was $10^{16}\,\mathrm{cm}^{-2}$ and post-implantation anneals were performed at 600, 800, and 1000°C for 60 minutes. One of the samples was left as-implanted to act as a reference.

The experiments done on these samples closely follow those of the silicon doped ones. Again, SIMS has been used to determine the dopant distribution and the crystal quality has been characterized by RBS and TEM. Correlation of these results with the resistance distribution has been provided by SSRM.

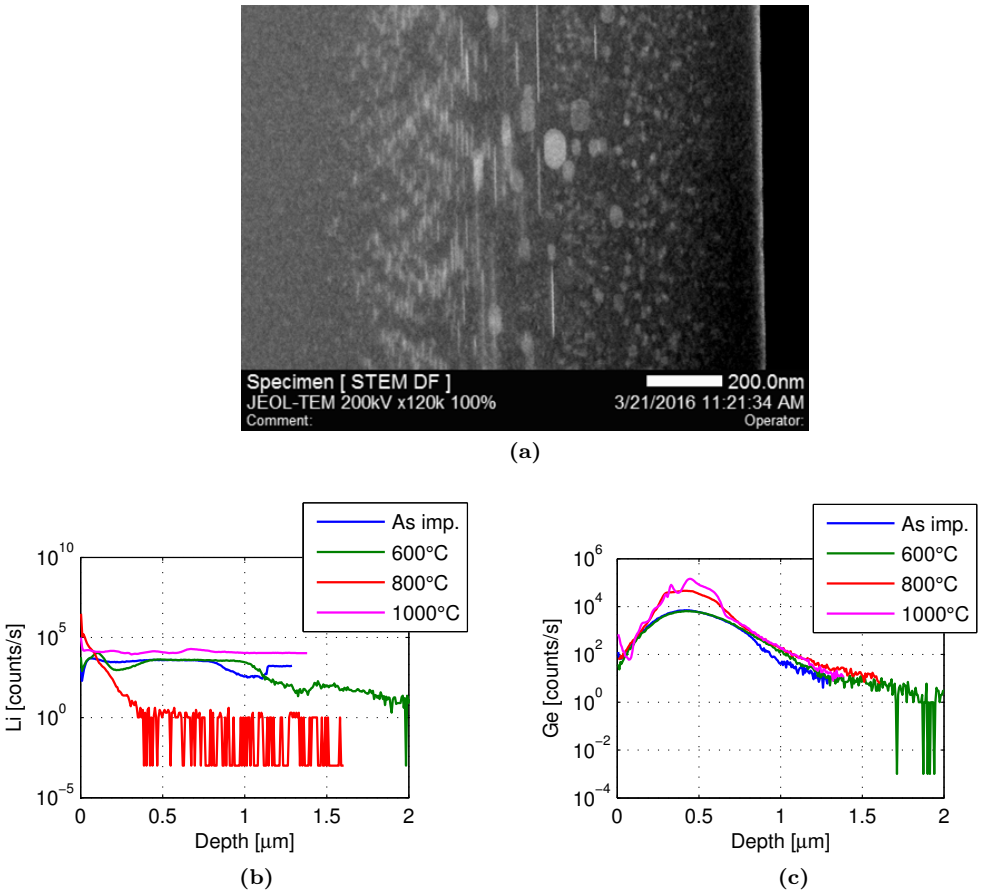

Figure 5.5: *(a) A scanning tunnelling electron micrograph (STEM) of precipitates in the Ge implanted sample after annealing at 1000° C. (b) and (c) Uncalibrated SIMS profiles for lithium and germanium, respectively. SIMS measurements and STEM image courtesy of Bjørn Brevig Aarseth [106]. As for the silicon implanted sample, the erratic behaviour of the 800° C lithium curve and the 600° C germanium curve is due to the signal falling below the detection limit of the instrument.*

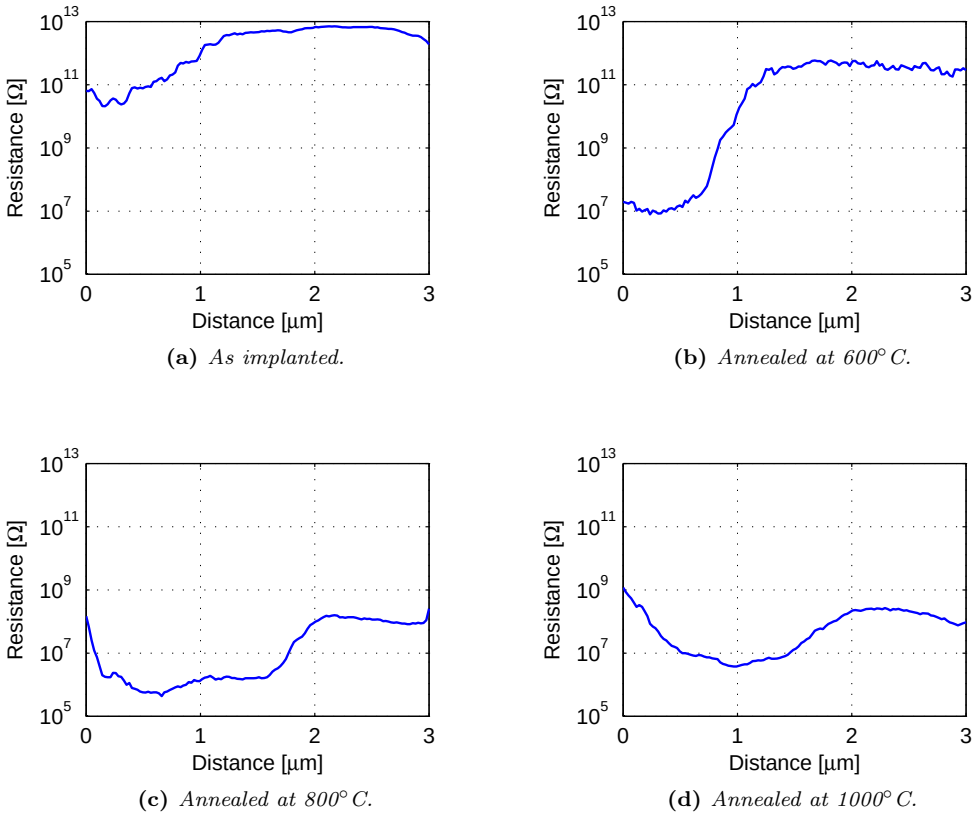

(a) *As implanted.* **(b)** *Annealed at 600° C.*

(c) *Annealed at 800° C.* **(d)** *Annealed at 1000° C.*

Figure 5.6: *Resistance profiles of germanium implanted zinc oxide samples. In all profiles, the sample edge is located 100–300 nm to the left of the plot.*

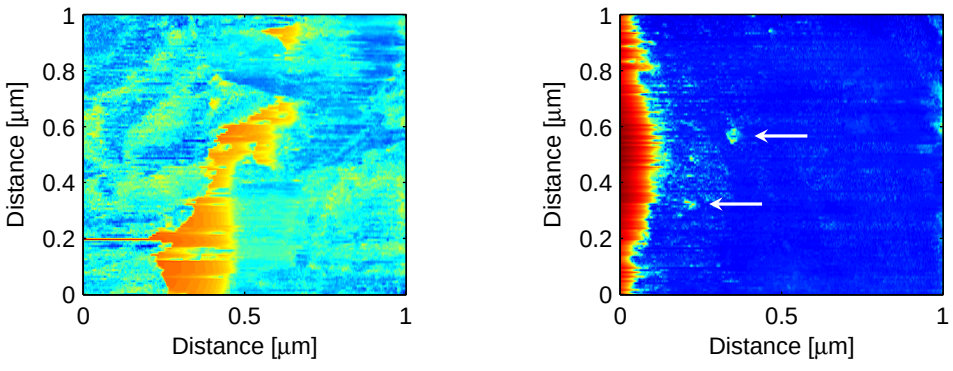

(a) **(b)**

Figure 5.7: *(a) Indications of precipitates in the as-cleaved 1000° C annealed Ge implanted sample. (b) White arrows pointing at indications of precipitates in the same sample after mechanical polishing.*

Experiments

For SSRM experiments the samples received no preparation apart from manual cleaving to access a fresh cross section. On all four samples, SSRM was conducted with a bias voltage of 4 V applied to the sample with respect to the probe. The scan size was 3×3 µm and the scans were run at a frequency of 0.25 lines/second with the same doped diamond probe for all samples.

To see whether the expected precipitates could be observed by SSRM, a 1×1 µm scan was performed on the sample annealed at 1000°C with a bias of 900 mV and a frequency of 0.25 lines/s. As ZnO is a very soft material, it was expected that the precipitates would be at least as hard, and probably harder. This should imply a higher polishing rate for zinc oxide than the precipitates, meaning that polishing could make the precipitates more accessible for measurements. The sample was hence polished with the procedure developed in the previous chapter, before a second SSRM study was undertaken. This measurement was done over an area of the same size, and with the same frequency and doped diamond probe as for the as-cleaved measurement. The bias was increased to 1 V.

Results and Discussion

Figure 5.6 shows the results of the scanning spreading resistance microscopy of the temperature series. In the as-implanted sample shown in figure 5.6a the lower resistance close to the sample edge (far left) is expected to be caused by a partial activation of the implanted germanium. The high resistance further into the sample may, as for silicon, be caused by lattice damage from the implantation.

The resistance profile after a 600°C anneal is shown in figure 5.6b. The most prominent difference to the as-implanted case is a drastically reduced resistance in the implanted area. Also, the resistance deeper into the sample has decreased by almost two orders of magnitude. From the SIMS profiles in figure 5.5 it is seen that annealing at 600°C does not significantly alter the lithium and germanium distributions. It thus seems plausible that the observed reduction in resistance is caused by a reduced degree of lattice damage, and this correlates with Hall effect measurements which show a slightly increased mobility.

After annealing at 800°C the resistance of the implanted region has decreased further and, more notably, the resistance of the region *beneath* the implantation peak has dropped dramatically. From the SIMS profiles this correlates well with a slightly increased Ge concentration at the implantation peak and a drastic depletion of lithium. The erratic jumps in the Li SIMS profile are caused by the lithium concentration falling below the detection limit of the instrument.

Finally, after the 1000°C anneal, the size of the low resistance region has decreased and it appears to have shifted slightly deeper into the sample. The SIMS profiles show that the peak of the Ge concentration does indeed lie somewhat deeper than after the 800°C anneal, but not as much as what is indicated in the SSRM results. The lithium on the other hand, has returned to the implanted region to a concentration higher than that seen in the as-implanted sample. The resistance is however drastically lowered, which is assumed to be related to a reduced degree of crystal damage. No germanium precipitates were observed in these SSRM measurements, indicating that the electrical properties in the implanted region is dominated by the bulk carrier concentration (including Ge acting as a donor) and the precipitates, if any, are too small to be observed. This is indeed confirmed by TEM measurements where inclusions with diameters below 10 nm was observed, *i.e.* too small to be detected by SSRM with the presently used probes.

From the STEM micrograph of the sample annealed at 1000°C, shown in figure 5.5a, it is clearly seen that a significant number of precipitates have formed in the region between 300 and 1000 nm from the sample edge. SSRM results of the same sample, shown in figure 5.7, also show indications of this, but not in the same amount. This is, at least partly, because STEM measures *through* the sample while SSRM has the best resolution for features at the surface. In the measurement of the as-cleaved surface shown in figure 5.7a, there is a considerable non-uniformity in the resistance level. It is possible that this is caused by implantation damage, but germanium related precipitates may also be a source of this effect. The precipitates observed in figure 5.5a have been identified as $ZnGeO_4$, which is a wide band gap semiconductor ($E_g \sim 4.8$ eV). It is likely that this has a lower carrier concentration than the surrounding ZnO which may explain the higher resistance regions seen in figure 5.7a. An additional contribution might stem from the heterojunctions between the precipitates and the surrounding matrix. These can cause depletion regions which makes the observed regions of higher resistance larger than the physical size of the precipitates.

The SSRM results after polishing are shown in figure 5.7b, where the interface between the sample and the epoxy can be seen in the left hand side of the image. A few hundred nanometers inside of the sample edge small localized regions of increased resistance can be observed, and it is plausible that these result from precipitates.

To summarize the findings, germanium, like silicon, acts as a donor when introduced into zinc oxide. Unlike silicon however, the Ge atoms tend to agglomerate into precipitates upon annealing at 1000°C.

5.3 Heterostructures

For synthesizing devices consisting of several materials, or multiple layers of the same material, magnetron sputtering and epitaxial growth are both widely used in research and production. Both techniques are routinely used at the University of Oslo for producing samples for various projects, and knowledge about the nanoscale electrical properties of the resulting films is thus valuable.

Two groups of heterostructures have been studied. One is the sputter deposited reference samples elaborated in section 4.2, while the other consists of epitaxially grown ZnO and $Mg_xZn_{1-x}O$ films.

5.3.1 Sputter Deposited Reference Structures

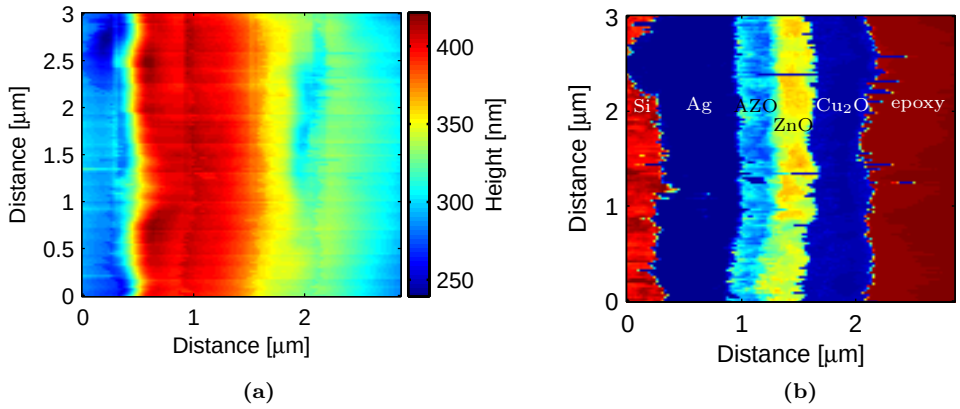

Figure 5.8: *Simultaneously acquired topography (a) and SSRM (b) images of a polished R3 reference sample. From left to right, the regions correspond to the silicon substrate, silver, Al doped ZnO, undoped ZnO, cuprous oxide, and finally epoxy resin at the far right.*

Background

The sputter deposited films produced at MiNaLab have been widely characterized in terms of structure and macroscopic electrical properties, but in-depth knowledge about the microscopic conductivity was lacking. Hence, as the set of sputter deposited reference samples described in section 4.2 was available, an examination of their resistivities was conducted.

Experiments

The details of the thin film deposition were given in section 4.2. Following the preparation scheme described in section 4.6 scanning spreading resistance microscopy was conducted on a reference sample of the R3 geometry. A bias of 2 V was applied to the sample with respect to the probe and an area of $3 \times 3\,\mu m$ was scanned at a frequency of 0.25 lines/s with a boron doped diamond coated probe.

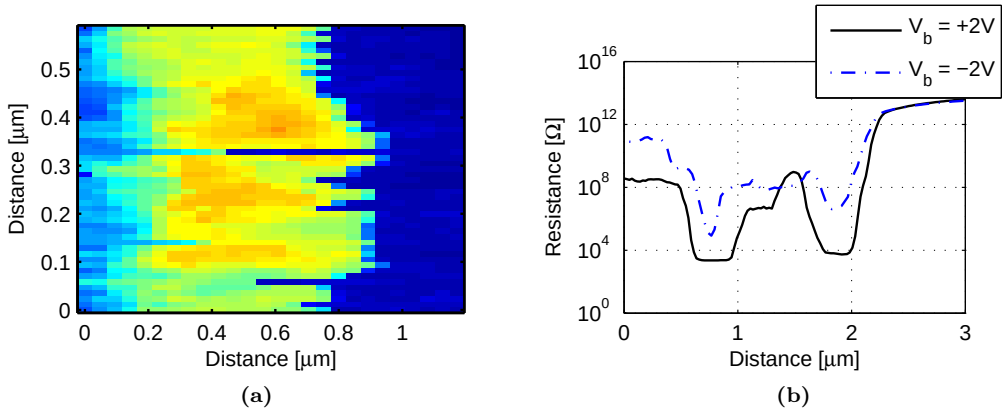

Figure 5.9: *(a) Zoomed view of the central area of figure 5.8b where highly resistive areas of the ZnO film are visible. (b) Averaged SSRM resistance profiles for the R3 sample scanned with the CDT-NCHR probe with positive and negative bias voltage.*

Results and Discussion

The resulting SSRM image is shown in figure 5.8b. It can be observed that while the silver and cuprous oxide films appear to have a fairly uniform resistance throughout, the same cannot be said about particularly the ZnO and partially the AZO film. Comparison of the SSRM image with the simultaneously acquired topography data shown in figure 5.8a shows no indication of the topography being the cause of this non-uniformity. In the AZO film, the bulk appears to have a fairly uniform resistance, which means that the Al dopants are evenly distributed. It however appears to be more contrast along the interfaces with the neighboring films. A possible explanation is local carrier depletion associated with the formation of a Schottky barrier and an n-n$^+$ junction to the Ag and ZnO film, respectively. In the undoped zinc oxide film, the bulk shows significant inconsistencies in the measured resistance. Figure 5.9a shows a zoomed view of the central region of figure 5.8b, where two of the larger irregularities can be seen. These appear to be several hundred nanometers in the longest direction which, although the resistance contours is not necessarily equal to the actual size of a feature, is significantly larger than the expected grain size (10–40 nm). A more plausible origin of the high resistance regions is then unintentional introduction of impurities either from the target or the sputtering chamber. The highest measured resistance in these features is $3.4 \times 10^7\,\Omega$ which is about one order of magnitude higher than the surrounding areas of the film. The identification of such non-uniformities is important from a device perspective, where optimal process control is pursued.

Like seen before, in figure 5.8b the resistance in the Cu_2O appears to be of the same order of magnitude as the Ag. The averaged resistance profile of this dataset is plotted in figure 5.9b along with a second profile obtained with the same probe and sample but with opposite bias polarity, *i.e.* −2 V applied to the sample with respect to the probe. With the negative bias, the Ag and Cu_2O films appear narrower than when positive bias was applied, and the ZnO and AZO are not as well discriminated. The significant influence of the bias polarity on the measured resistance indicates that the tip-sample contact is rectifying for most of the films. An exception seems to be the ZnO film which measures to an identical resistance with either polarity. This does however not provide any insight into the unexpectedly low resistance of the Cu_2O film, and its origin still remains unknown.

5.3.2 Epitaxially Grown ZnO/MgZnO Heterostructures

Background

SPM provides a nanoscopic view of material properties and is potentially a powerful tool for direct measurements of quantum wells and two-dimensional electron gases in ZnO/$Mg_xZn_{1-x}O$ structures. Three heterostructures which were expected to form a 2DEG have been explored. Additionally one ZnO/AZO sample has been grown for microscopic characterization of the resistivity in these films. Films grown by MOCVD at MiNaLab have been widely characterized electrically

Table 5.1: *Heterostructure sample geometries.*

Name	Structure
678	Al_2O_3/AZO/ZnO
679	Al_2O_3/ZnO/$Mg_xZn_{1-x}O$
A25	Al_2O_3/ZnO/$Mg_xZn_{1-x}O$/Ag
A8	Al_2O_3/ZnO/$Mg_xZn_{1-x}O$/ZnO/$Mg_xZn_{1-x}O$/Ag

in the past. However, like for the sputter deposited films, all prior examinations have been macroscopic in nature (Hall effect and photoluminescence measurements) so little is actually known about their microscopic resistance distributions. Sample names and structures are given in Table 5.1. Of these, 678 and 679 were grown in-house by MOCVD on an EMF Titan reactor, while A8 and A25 was grown by MOCVD at the Institue of Microelectronics in Singapore. All four samples were grown on sapphire (0 0 0 1) substrates.

Experiments

678 and 679 were both prepared at 370°C and 600 Torr with diethyl-zinc (DEZn), trimethyl-aluminium (TMAl), tert-butanol (t-BuOH), and bismethylcyclopentadienyl-magnesium ($MeCp_2Mg$) as precursors for, Zn, Al, O, and Mg, respectively. The flow rates for the respective species were 100, 12, 150, and 700 sccm, and the substrates were rotated at 60 rpm for both samples. For 678, the nominal film thicknesses were 250 nm for the AZO and 500 nm for the undoped ZnO. For 679, the ZnO film was expected to have a thickness of 250 nm while the $Mg_xZn_{1-x}O$ should be 1250 nm.

A8 and A25 were prepared with the same Mg precursor but with dimethyl-zinc as the Zn precursor. The temperature was 920°C, and growth was carried out in an Aixtron reactor with close-coupled showerhead configuration. For A8, the nominal film thicknesses were 2 µm for the bottom ZnO layer, 60 nm for the $Mg_xZn_{1-x}O$ barriers, and 40 nm for the ZnO well layer. Nominal film thicknesses for A25 were 2 µm for the ZnO and 70 nm for the $Mg_xZn_{1-x}O$. For both samples, the expected Mg concentration was $x = 0.18$. For contacting, a 500 nm thick Ag-film was thermally evaporated on top of both samples.

678 and 679 did not receive any sample preparation apart from manual cleaving prior to SSRM measurements, which were conducted with a bias of 4 V applied to the sample, and scanned with a frequency of 0.25 lines/s with a diamond coated probe. A8 and A25 were ion milled with the Hitachi IM4000 at the University College of Southeast Norway as explained in section 4.6.3. The same probe type and frequency as for the 678/679 samples were used, but the bias voltages were 500 and 50 mV for A8 and A25, respectively.

Results and Discussion

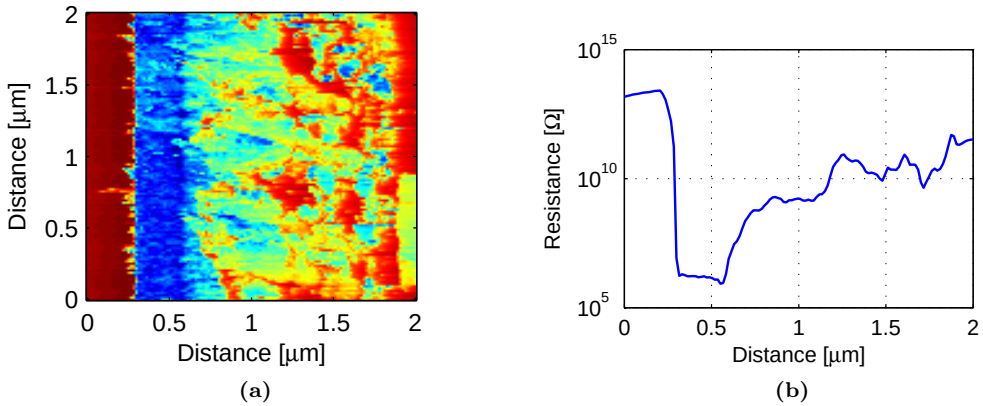

(a) (b)

Figure 5.10: *SSRM and average resistance profile of an unpolished specimen of 678 before deposition of the Al film.*

Figure 5.10 shows SSRM data and an average resistance profile of the 678 sample. From left to right, the regions seen are the sapphire substrate, AZO, and ZnO. It can be identified that the AZO film has a relatively uniform resistance throughout while, on the contrary, the undoped ZnO film does not. The reason for the non-uniformity has not been absolutely ascertained, but as the Titan reactor has required severe maintenance and service work prior to the growth of this sample it seems plausible that the cause is related to the state of the reactor.

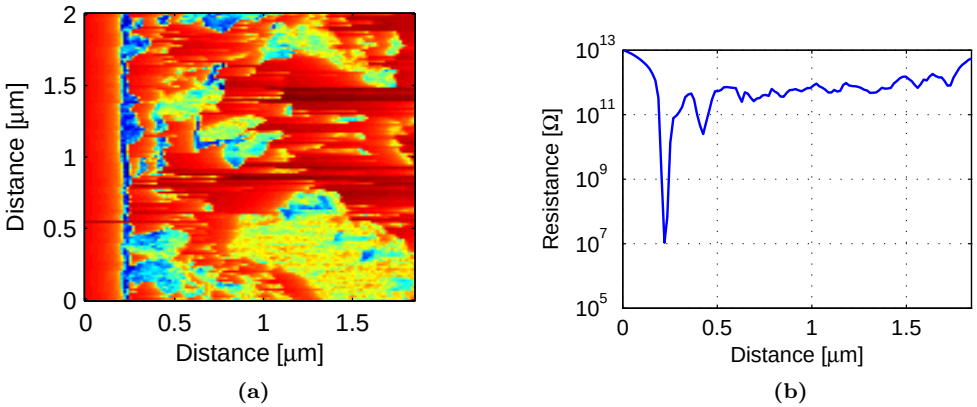

Figure 5.11: *SSRM and average resistance profile of an unpolished 679 prior to Al deposition.*

Figure 5.11 shows the results of SSRM on a 679 sample, where the substrate is again seen at the left side and the films should have been visible towards the right. Unfortunately, neither the ZnO nor the $Mg_xZn_{1-x}O$ film has a uniform resistance, and only the substrate-ZnO interface is identifiable. To improve the electrical contact between the samples and the microscope, an aluminium film was thermally evaporated on top of both 678 and 679, but the subsequent SSRM measurements did not yield better results. On this basis it is evident that observing a two dimensional electron gas will be impossible due to the non-uniform resistance in the films and that attention must be directed towards improving the film quality before further 2DEG experiments can take place.

The results of an SSRM study of the A25 sample is shown in figure 5.12a. Here, the zinc oxide, $Mg_xZn_{1-x}O$, and Ag films are all clearly identified with ZnO to the left, an approximately 100 nm wide $Mg_xZn_{1-x}O$ barrier peak in the center, and Ag towards the right. Keeping in mind that the finite size of the probe will influence the apparent feature dimensions, the width of the well is fairly consistent with the 70 nm that was estimated from the growth rate. Although there is a marked dip in the resistance on the ZnO-side of the MZO barrier this is far too faint to claim that it is caused by a 2DEG.

Results from the A8 sample are shown in figure 5.12b. Here, a ZnO quantum well (orange) is seen between two $Mg_xZn_{1-x}O$ barriers (red) in the region from $\sim$ 50 nm to 200 nm. To the far left is the top of the ZnO layer, and to the right of the well the silver film is clearly visible. The left barrier has a uniform width of about 40 nm, while the width of the right barrier varies from 40 nm at the bottom of the figure to 70 nm at the top. The well has an approximately uniform width of 35 nm. From the deposition rates the expected widths were 60 nm for the barriers and 40 nm for the well which is in reasonable agreement with the measured values. From the averaged resistance plot in the lower half of figure 5.12b it can be extracted that the resistance in the well is about $1 \times 10^{10}\,\Omega$ while the left and right barriers measure $4 \times 10^{11}\,\Omega$ and $7 \times 10^{11}\,\Omega$ respectively. The resistance level in the well is however about the same as in the ZnO film outside the well, so it is concluded that no two dimensional electron gas is observable here either.

The reason for the missing 2DEG can possibly be related the synthesis of these particular samples. It is also possible that the ion milling has caused an unacceptable degree of damage to the surface.

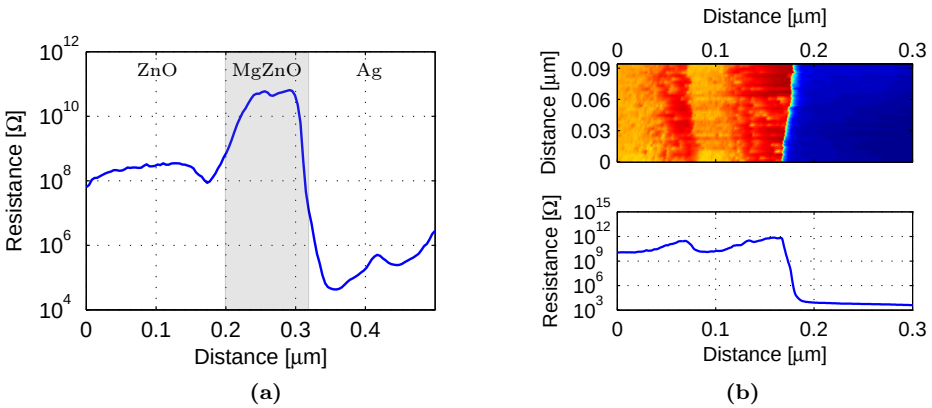

Figure 5.12: *(a) Average resistance profile of an ion milled A25 sample. (b) SSRM result for an ion milled A8 sample. From left to right this figure shows zinc oxide, a 60 nm MZO barrier, a 40 nm ZnO quantum well, a second MZO barrier of the same width as the other, and finally a silver layer.*

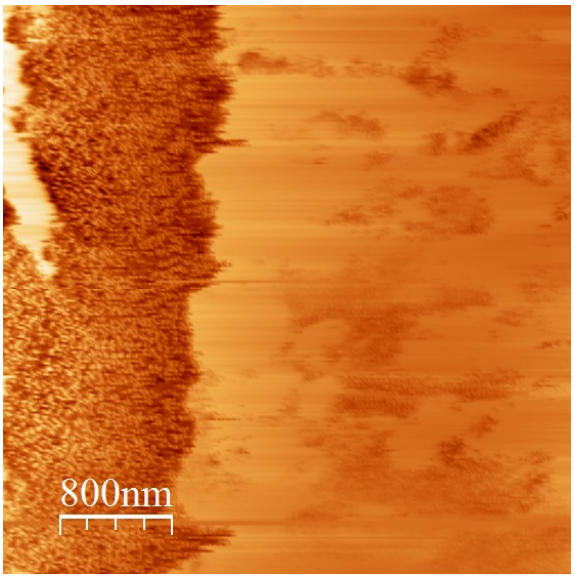

Figure 5.13: *SSRM data captured with the Nanonics SPM. Discussed under further work.*

Chapter 6

Conclusions and Further Work

This chapter summarizes the conclusions made during the course of working with this thesis and identifies areas where continued effort could prove fruitful.

Method Development

For silicon substrates, manual mechanical polishing with cloths and diamond slurry was found to be a relatively fast, simple, and reliable way of preparing samples for scanning spreading resistance microscopy. Mechanical polishing with diamond lapping films was also determined to be a viable option, but is more time consuming and with no observed advantages over slurry based polishing. During polishing, the sample should be protected by either a slab of aluminium or a dummy piece of silicon, and Heraeus Kulzer Technovit 5000 resin was found to yield a sharp sample edge. For sapphire substrates, no mechanical processing route was found to produce adequate results. However, initial attempts at ion milling looks promising, and this appears to be the road ahead. Like silicon, zinc oxide substrates were found to be well suited for polishing with diamond slurry if protected either by an Al slab or a ZnO dummy. Here Struers Epofix was found to be the best suited resin.

Seven different probes were tested and compared to see which gave the highest quality SSRM images. In general it was found that, apart from the one with the lowest force constant, the boron doped diamond probes were superior to the other options. Specifically, in accordance with prior experience, the CDT-NCHR from Nanosensors was consistently found to produce the highest contrast. Contrary to previous reports, it has been found that with the probes, samples, and settings used in this work, silver paste provides a better back side contact to the microscope than eutectic indium-gallium.

Three Matlab scripts were produced to simplify the data analysis workflow, and these will be made available to the other users of the Dimension 3100.

Experimental Work

The scanning spreading resistance microscopy and scanning capacitance microscopy done on the copper diffused zinc oxide sample clearly identified that the in-diffused atoms show acceptor behaviour, reducing the conductivity of the sample. The individual contributions from the precipitates and the substitutional Cu could, however, not be distinguished. Comparison of SSRM and SCM results indicate that the diffusion has not caused p-type conduction in the measured sample. The samples with in-diffused Al and Ga both showed a 10^2–10^3 difference in resistance between bulk and the in-diffused region. For the aluminium sample this is consistent with the known carrier concentration of the substrate and the chemical profile acquired by SIMS. For the Ga sample this is lower than expected, but may be an indication that the processing has decreased the bulk resistivity of the substrate.

The SSRM study of the ion implanted samples support the SIMS data in proving that both Si and Ge take zinc lattice sites. No clear image of the precipitates seen by STEM in the germanium implanted samples could be acquired with SSRM or SCM, but results indicative of their presence were obtained.

Further, the examination of epitaxial films grown at MiNaLab showed that their resistivities were far from uniform on the nanoscale. The samples obtained from the Institute of Microelec-

tronics in Singapore exhibited well defined resistance levels, and both the single heterostructure and quantum well were successfully delineated with SSRM with dimensions close to the expected values based on the deposition rates. Unfortunately, no sign of a two dimensional electron gas could be found in either sample.

Further Work

In the area of sample preparation, it is expected that better polishing of sapphire can be achieved with a more refined ion milling procedure. Two of the immediate ideas are (i) to reduce the accelerating voltage when the ion beam polishes the films, and (ii) to follow the cross sectional milling with a short low-power plan view milling to remove the damaged surface layer.

To better understand what went wrong with the grown ZnO and $Mg_xZn_{1-x}O$ films so that they can hopefully be improved in the future, structural characterization would have been beneficial to identify whether the non-uniform resistivity stems from structural or electronic properties. Structural characterization of the cuprous oxide film on the R3 structure would also have been interesting to hopefully gain insight into the unexpectedly low resistance.

Although initial temperature dependent SSRM has been conducted on both A8 and A25 samples no reliable result has been obtained at low temperature, as the probe becomes severely unstable when contacting the sample. The reason is not known, but one theory is that it is related to heat transfer between the probe and the sample. More work needs to be done to ascertain the cause of the instability and subsequently improve the mechanical tip-sample contact before the electrical low temperature measurements can be developed further. Resistance contrast has however been achieved at room temperature with the same instrument, as illustrated in figure 5.13. Here the low resistance region to the left is silver, while the high resistance region on the right is zinc oxide. Although contrast is achieved and relatively stable at room temperature, it has proved difficult to find parameters which provides a measurable resistance without saturating the linear amplifier. Initial attempts at implementing a logarithmic amplifier has not changed this, but a more thorough assessment should be carried out.

Appendix A

Matlab Scripts

A.1 BinaryImport

```
% Script to import biary file from Nanoscope 5.33
%
% Inputs: - path to folder containing datafile
%         - filename
%
% Output: - topography data
%         - SSRM/SCM data
%         - string stating datatype
%         - # of samples per line
%         - # of lines
%         - bias voltage
%         - scan size
%
% CHANGELOG:
% - v 2.0
%     - Implemented import of SCM data
%     - Implemented output of # of lines and datatype string
%
function[ topo , data2 , sampsperline , numlines , biasVoltage,...
                ss , datatype ] =  BinaryImport_v2( fname , fdir )
%
% ------------------------------------------------------------------



% ------------------- Extract header from file --------------------

% cd to given dir.
cd( fdir );

% Read entire file into a vector of characters
text = fileread(fname);

% Find last line of header. regexp gives index of first character,
% add 13 to get index of last char.
headerEndIdx = regexp(text,'\*File list end') + 13;

% Split header part of text vector at each newline character
splittext = strsplit( text( 1 : headerEndIdx ),'\n' );

% Transpose result from row to column form
```

```
header = splittext';

% Should now be able to regexp for the desired quantities as usual

% In header: 3 symbols follow the d on the last line before
% padding starts i.e. padding starts at
% text(20647) = rawData(10324)

% ------------------------------------------------------------------



% --------------- Extract datatype from header --------------------

% Find line stating datatype
dtIdx = ...
        regexp( header , '\\@2:Image Data: S \[\]\ "\w+/?\w*\s?\w*"
           ' );
dtLine = find( ~cellfun( 'isempty' , dtIdx ) )

% Extract datatype from this line
% 1. delete everything up to first double quote
datatype =...
        regexprep( header( dtLine( 1 ) ) ,...
                '\\@2:Image Data: S \[\]\s"' , '');

% 2. Delete last double quote and trailing space
datatype = regexprep( datatype , '"\s?' , '' )

% 3. Convert from cell array to string
datatype = char(datatype)

% ------------------------------------------------------------------



% --------------- Extract samples/line from header ----------------

% Find the lines stating samples/line: ###
% First the string is matched to all cells of the header array,
% returning an array of zeros and ones. One if the cell matches
% the string, zero otherwise
splIdx = regexp( header , '\Samps/line: \d\d\d' ) ;

% Find indices of the ones
splLines =  find( ~cellfun( 'isempty' , splIdx ) ) ;

% Then extract the number of s/l from one of these lines of header
% The regexprep call replaces all non-numeral characters in
% the first argument with nothing ('')
splString = regexprep( header( splLines( 1 ) ) , '\D' , '' ) ;

% Then convert the string representation of the number to a
% numeric representation
sampsperline = str2double( splString ) ;

% ------------------------------------------------------------------
```

```
% -------------------- Extract number of lines ------------------

numlinesIdx = regexp( header , '\\Number of lines: \d\d\d' );
numlinesLine = find( ~cellfun( 'isempty' , numlinesIdx ) );
numlines = regexprep( header ( numlinesLine(1) ) , '\D' , '' );
numlines = str2double( numlines )

% ---------------------------------------------------------------



% ----------------- Extract bias voltage -------------------------

% Follow same procedure as for samples/line
biasIdx = regexp( header ,...
    '\@2:DC sample bias: V \[Sens. DC sample bias\] \(\d+\.\d+ mV/
       LSB\) -?\d+\.\d+ mV' ) ;

% Find indices of matches
biasLine = find( ~cellfun( 'isempty' , biasIdx ) );

% Check whether dataset is AFM or SSRM. 0 = SSRM, 1 = AFM
if isempty(biasLine) == 0

    % If data is SSRM, extract the number as string in two steps
    %  - 1. delete everything up to the closing bracket
    %  - 2. delete the units
    biasString = regexprep( header( biasLine(1) ) , '.*\)' , '' ) ;
    biasString = regexprep( biasString , ' .?V' , '' ) ;

    % Convert string to number
    biasVoltage = str2double( biasString ) ;

else
    biasVoltage = 0 ;
end
% ---------------------------------------------------------------



% ---------------------- Extract scan size ----------------------

% Match scan size string. Allow integral and decimal scan sizes
ssIdx = regexp( header , '\Scan size: \d+\.?\d*? .m' ) ;

% Find indices of matches
ssLines = find( ~cellfun( 'isempty' , ssIdx ) ) ;

% Extract scan size as string.
ssString = regexprep( header( ssLines( 1 ) ) , '[^\d.]' , '' ) ;
ssStringLength = cellfun( 'length' , ssString ) ;

% Apply appropriate formatting if length of string is 2 or 6
if ssStringLength == 2
   ssString = regexprep( ssString , '^\d' , '' ) ;
elseif ssStringLength == 6
```

```
    ssString = regexprep( ssString , '^\d.\d' , '' ) ;
end

% Convert string to number
ss = str2double( ssString );

% ------------------------------------------------------------------



% ------------- Extract raw data as 16 bit signed int's -----------

% Open specified file again
fid2 = fopen( fname , 'r' );

% Read entire file contents into vector of doubles
rawData = fread( fid2 , 'int16' );

% Close file
fclose(fid2);

% ------------------------------------------------------------------



% ------------------------- Data processing ----------------------

% Finding start of datapoints
 % - assume padding has started at
 % rawData(0.5 * (headerEndIdx + 70) )
offset = round( 0.5 * (headerEndIdx + 70) );
dataStart =  find( rawData( offset : end) , 1 );
dataStart = dataStart + offset - 2;
% Why need to subtract 2 ? Data starts at 20481 after all
% bless gives offset, i.e. first element has offset = 0
% rawData read in matlab shows element number,
% i.e. first element = 1
% Also, loop is defined so it adds 1 to all indices, i.e.
% input to loop is the last element before start of dataset.

% Sort datapoints into arrays
for k = 1 : numlines ,
    for m = 1 : sampsperline ,
        topoElement = ...
                  rawData( dataStart + ( ( k - 1 ) * sampsperline )
                      + m ) ;
        rawTopo( m , k ) = topoElement ;

        data2Element = ...
                  rawData( dataStart + ( sampsperline * numlines )
                     + ...
                    ( k - 1 ) * sampsperline + m ) ;
        rawdata2( m , k ) = data2Element ;
    end
end

% Transpose data to match the measurement
rawTopo = rawTopo' ;
```

```
rawdata2 = rawdata2' ;

% Extract conversion parameters for height from header
    % nm/V
    nmvIdx = ...
          regexp( header , '\\@Sens\. Zscan: V \d+\.?\d* nm/V' ) ;

    % Find indices of matches
    nmvLines = find( ~cellfun( 'isempty' , nmvIdx ) ) ;

    % Then extract the nm/V from one of these lines of header...
    % Delete everything preceding the number
    nmvString = regexprep( header( nmvLines(1) ) , '.+ V' , '' );

    % Delete unit
    nmvString = regexprep( nmvString , '[^\d\.]' , '' );

    % Convert string to number
    nmv = str2double( nmvString ) ;

    %   Sensitivity
    hsensIdx = ...
          regexp( header , '\\@2:Z scale: V \[Sens. Zscan\] \(\d
             *\.?\d* V/LSB\) \d*\.?\d* V');

    hsensLines = find( ~cellfun( 'isempty' , hsensIdx ) );

    % Delete everything up to the closing bracket
        % following the first number
    hsensString = ...
          regexprep( header( hsensLines(1) ) , '.*\)' , '' );
    % Delete unit
    hsensString = regexprep( hsensString , ' .?V' , '' );

    hsens = str2double( hsensString );

    % Range of recorded values,
        % 16 bit signed => 65536 possible values
    range = 65536;

    % Compute height (nm) from raw data and conversion variables
    topo = rawTopo * nmv * hsens / range ;

% Extract conv. parameters from header depending on
% the performed measurement
switch datatype
    case 'Resistance'
        % Extract sensitivity
        rsensIdx = ...
                  regexp( header , '\\@2:Z scale: V \[Sens.
                     Resistance\] \(\d*\.?\d* V/LSB\) \d*\.?\d* V'
                     );

        rsensLines = find( ~cellfun( 'isempty' , rsensIdx ) );

        % Delete everything up to closing bracket
        rsensString = ...
                  regexprep( header( rsensLines(1) ) , '.*\)' , ''
```

```
                );
        % Delete unit
        rsensString = regexprep( rsensString , '.?V' , '' );
        rsens = str2double( rsensString );

        % Compute resistance [V]
        data2 = rawdata2 * rsens / range ;


    case 'dC/dV Amp'
        % Extract sensitivity
        csensIdx = ...
                regexp( header , '\\@2:Z scale: V \[Sens. dC/dV
                    Amp\] \(\d*\.?\d* V/LSB\) \d*\.?\d* V' );
        csensLines = find( ~cellfun( 'isempty' , csensIdx ) );

        % Delete up to closing bracket
        csensString = ...
                regexprep( header( csensLines(1) ) , '.*\)' , ''
                    );

        % Delete unit
        csensString = regexprep( csensString , '.?V' , '' );
        csens = str2double( csensString );

        % Compute dC/dV Amp [V]
        data2 = rawdata2 * csens / range ;


    case 'dC/dV Phase'
        % Extract sensitivity
        csensIdx = ...
                regexp( header , '\\@2:Z scale: V \[Sens. dC/dV
                    Phase\] \(\d*\.?\d* ./LSB\) \d*\.?\d* .' );
        csensLines = find( ~cellfun( 'isempty' , csensIdx ) );

        % Delete up to closing bracket
        csensString = ...
                regexprep( header( csensLines(1) ) , '.*\)' , ''
                    );

        % Delete unit
        csensString = regexprep( csensString , '[^\d\.]' , '' );
        csens = str2double( csensString );

        % Compute dC/dV Phase [deg]
        data2 = rawdata2 * csens / range ;


    case 'SCM Data'
        % Extract sensitivity
        csensIdx = ...
                regexp( header , '\\@2:Z scale: V \(\d*\.?\d* V/
                    LSB\) \d*\.?\d* V' );
        csensLines = find( ~cellfun( 'isempty' , csensIdx ) );

        % Delete up to closing bracket
        csensString = ...
```

```
                    regexprep( header( csensLines(1) ) , '.*\)' , ''
                        );

        % Delete unit
        csensString = regexprep( csensString , '[^\d\.]' , '' );
        csens = str2double( csensString );

        % Compute SCM data [V]
        data2 = rawdata2 * csens / range ;
end % of switch


% ------------------------------------------------------------------



% -------------------------- Testoutput -------------------------
%
% toposize = size(topo)
% data2size = size(data2)
% samplesperline = sampsperline
% scansize = ss
% bias = biasVoltage
% ---------------------------------------------------------------
%
%
% % ------------------------ Calibration/comparison --------------
%
% % For comparing manually computed values to nanoscope conversion
% %  - place 128 column output file from NS6 in same folder as
% %    the one to compare it to, then uncomment this section.
% %    Differences are found in dtopo and dssrm matrices:
% %
% figure( 'name' , 'Matlab Processed' )
% subplot(1,2,1)
% imagesc(topo)
% colormap hot
% set(gca,'YDir','normal')
%
% subplot(1,2,2)
% imagesc(data2)
% colormap hot
% set(gca ,'YDir' , 'normal')
%
% compfolder = fdir;
% compfile = 'jon_20160316_gzo-1000.003.txt';
%
% [ comptopo , compdata2 ,...
%   SamplesPerLine , BiasVoltage , ScanSize ] = ...
%     nanoscope_import_ssrm_v3_1_Ns6( compfile , compfolder ) ;
%
% % Transpose topo and SSRM data
% comptopo = comptopo' ;
% compdata2 = compdata2' ;
%
% figure('name' , 'Nanoscope Processed' )
% subplot(1,2,1)
% imagesc(comptopo)
```

```
% colormap hot
% set( gca , 'YDir' , 'normal' )
%
% subplot(1,2,2)
% imagesc(compdata2)
% colormap hot
% set( gca , 'YDir' , 'normal' )
%
% % Find difference between manually and
% % automatically converted values
% dtopo = comptopo - topo;
% ddata2 = compdata2 - data2;
%
% figure( 'name' , 'Difference' )
% subplot(1,2,1)
% imagesc(dtopo)
% colormap hot
% colorbar
% set( gca , 'YDir' , 'normal' )
%
% subplot(1,2,2)
% imagesc(ddata2)
% colormap hot
% colorbar
% set( gca , 'YDir' , 'normal' )
%
%
```

A.2 Multiplot

```
% Script to plot topography, SSRM, average resistance and infobox
% for a range of files.
%
%
%CHANGELOG:
% v 1.1
% - Optional planefit of topo image
%
% v 2.0
% - Implemented use of BinaryImport.m to read raw data from NS 5.33
% - Planefitting in both x and y directions
% - Automatic extraction of sample name for textbox from filename
%
% v 3.0
% - Restructured to enable plotting of SCM data
% from BinaryImport v3
%
%
clear

% ---------------------------- Input ------------------------------

% Define directory and filename:
%
% For windows
%fdir = ...
 'C:\Users\jonborg\Dropbox\Skole\UiO\Thesis\Experiments\SSRM\A25\
    A25pH\20160315' ;
%
% For linux
fdir = '/home/jon/Dropbox/Skole/UiO/Thesis/Matlab/testfiles/SCM' ;
%
% For both (do not include full stop before serial number)
filenameBase = 'jon_20160316_gzo-1000' ;

% Serial number of first file
firstFile = 1;

% Number of files to process
numFiles = 3;

% Choose whether to close figures. 0 = no, 1 = yes.
closeFig = 0;

% Choose whether to save figures. 0 = no, 1 = yes.
saveFig = 0;

% Choose whether topo image should be planefit. 0 = no, 1 = yes.
planefit = 1;

% Textbox details
probeType = 'Nanosensors CDT-NCHR' ;
plotNotes = '' ;

% Invert y-axis?
% imgsc inverts by default, set Y-axis to 'normal' to invert
```

```
%  or 'reverse' to keep imgsc default
yaxisDirection = 'normal' ;

% ------------------------------------------------------------------



% ------------------------- Main ---------------------------------

% Define cell array for filenames
files = cell( numFiles , 1 );

% Looping over the specified files
for i = firstFile : firstFile + numFiles - 1

    % Determine appropriate padding for serial number of filenames
    if i < 10
        padding = '00' ;
    elseif 10 <= i < 100
        padding = '0' ;
    else
        padding = '' ;
    end

    % Assemble filename from base + serial number + .txt
    files{i} = ...
          strcat( filenameBase , '.' , padding , num2str( i ) );
    disp(files{i})

    % Load data from import script
    [ topo , data2 , samplesPerLine , numlines , biasVoltage ,...
          scanSize , datatype ] = BinaryImport_v2( files{i} , fdir
             ) ;

    % Converting scan size to microns
    scanSize = scanSize / 1000;



    % ---------------------- Planefitting procedure ---------------

    switch planefit
        case 1
            disp('Planefitting topography')
            % Calculate slope of each line
            topoSlope = topo(:,end) - topo(:,1) ;

            % Calculate average slope of topo image
            avgSlope = sum(topoSlope,1) / size(topoSlope,1) ;

            % Subtract slope from image
            planefitTopoImg = topo ;

            ii = 0 ;
            for ii = 1 : samplesPerLine
                planefitTopoImg( : , ii ) = ...
                    planefitTopoImg( : , ii ) -...
                                        ( avgSlope * ii /
```

```
                                                samplesPerLine ) ;
                ii = ii + 1;
            end

            % Calculate slope of each column
            topoSlope = ...
                          planefitTopoImg(end , :) -
                             planefitTopoImg( 1 , : );

            % Calculate average slope
            avgSlope = sum(topoSlope,1) / size(topoSlope,1);

            % Subtract slope from image
            ii = 0 ;
            for ii = 1 : samplesPerLine
                planefitTopoImg( ii , : ) = ...
                    planefitTopoImg( ii , : ) - ...
                                          ( avgSlope * ii /
                                             samplesPerLine ) ;
                ii = ii + 1;
            end
    end

    % ---------------- Averaging procedure ------------------------

    % Calculate average value of each column of data2. Average of
    % column n is taken as sum of elements in column n divided by
    % the # of elements in the column.
    disp('Calculating avg. resistance')
    data2average = sum( data2 , 1 ) ./ size( data2 , 1 ) ;

    % If data2 is SSRM, convert average values from volts to ohms
    switch datatype
        case 'Resistance'
            if biasVoltage > 0
                sign = -1 ;
            elseif biasVoltage < 0
                sign = 1 ;
            end
            data2average = 1e6 ./ 10.^( sign * data2average ) ;
            avgYlabel = 'Resistance [\Omega]';

        case 'dC/dV Amp'
            avgYlabel = 'dC/dV [V]';

        case 'dC/dV Phase'
            avgYlabel = strcat('dC/dV Phase', '[', char(176) , ']')

        case 'SCM Data'
            avgYlabel = 'SCM Data [V]'
    end

    % Convert x-indices to distance for plotting avg. curve
    xlength = linspace( 0 , scanSize , samplesPerLine  ) ;

% ------------------------------------------------------------------
```

```
    % Set limits for image plotting
    plotLimits = [ 0 , scanSize ] ;

    % Extract sample name from filename.
        % Find index of underscore preceeding sample name
        uScores = regexp( files{i} , '_' ) ;
        nameStartIdx = uScores(2) + 1 ;

        % Find index of point following sample name
        points = regexp( files{i} , '\.' ) ;
        nameStopIdx = points( end ) - 1 ;

        sampleName = files{i}( nameStartIdx : nameStopIdx ) ;

        % Capitalise initial letter
        sampleName = ...
                  [ upper( sampleName( 1 ) ) sampleName( 2 : end )
                     ];



% ------------------------ Plotting -----------------------------

    fprintf('Plotting \n')

    % Define new figure
    figure( 'units' , 'normalized' , 'position' , [.1 .1 .5 .63 ] )

    % Set output file dimensions
    set(gcf,'PaperUnits','inches','PaperPosition',[0 0 9.6 6.91])

    % Plot topo data
    subplot(2,2,1, 'position' , [0.1 0.5838 0.4 0.3412 ] )
    switch planefit
        case 0
            imagesc( plotLimits , plotLimits , topo ) ;
            title ( 'Raw topography' , 'FontSize' , 14 )
        case 1
            imagesc (plotLimits , plotLimits , planefitTopoImg );
            title ( 'Planefit topography' , 'FontSize' , 14 )
    end
    colormap jet
    colorbar('eastoutside')
    xlabel( 'Distance [\mum]' , 'FontSize' , 14 )
    ylabel( 'Distance [\mum]' , 'FontSize' , 14 )
    set( gca , 'YDir' , yaxisDirection )
    set( gca, 'FontSize' , 11 )

    % Plot data2
    subplot(2,2,2)
    set( gca, 'Position' , [ 0.6 , 0.5838 , 0.3347 , 0.3412 ] )
    imagesc( plotLimits , plotLimits , data2 ) ;
    colormap jet
    title ( datatype , 'FontSize' , 14 )
    xlabel( 'Distance [\mum]' , 'FontSize' , 14 )
    ylabel( 'Distance [\mum]' , 'FontSize' , 14 )
    set( gca , 'YDir' , yaxisDirection )
```

```
    set( gca, 'FontSize' , 11 )

    % Plotting column averaged data2 as function of distance
    subplot(2,2,4)
    set( gca , 'Position' , [ 0.6 , 0.11 , 0.3347, 0.3412 ] )
    semilogy( xlength , data2average )
    title( ['Average' ,' ', datatype] , 'FontSize' , 14 )
    xlabel( 'Distance [\mum]' , 'FontSize' , 14 )
    ylabel( avgYlabel , 'FontSize' , 14 )
    xlim( [ 0 , scanSize ] )
    grid on
    set( gca , 'YMinorGrid' , 'on' )
    set( gca , 'FontSize' , 11 )

    % Place textbox in subplot 3
    subplot( 2 , 2 , 3 )
    set( gca , 'Position' , [ 0.1 , 0.11 , 0.3347 , 0.3412 ] )
    text( 0.25 , 1.05 ,...
          sprintf('%s' , 'Measurement Details') , 'FontSize' , 14 )
    text( 0 , 0.9 ,...
          sprintf(' Sample: %s ' , sampleName ) , 'FontSize' , 14 )
    text( 0 , 0.8 ,...
          sprintf(' Scan size: %.1f \\mum ' , scanSize ) ,...
            'FontSize' , 14 )
    text( 0 , 0.7 ,...
          sprintf(' Samples/line: %.f ' , samplesPerLine ) ,...
            'FontSize' , 14 )
    text( 0 , 0.6 ,...
          sprintf(' Bias voltage: %.f mV ' , biasVoltage ) ,...
            'FontSize' , 14 )
    text( 0 , 0.5 ,...
          sprintf(' Probe type: %s ' , probeType ) ,...
            'FontSize' , 14 )
    text( 0 , 0.4 ,...
          sprintf(' Filename: %s ' , files{i}(5:end) ) ,...
            'FontSize' , 14 , 'Interpreter' , 'none' )
    text( 0 , 0.27 ,...
          sprintf(' Notes: %s ' , plotNotes  ) , 'FontSize' , 14 )
    axis off

% ------------------------------------------------------------------

    % Save figure?
    switch saveFig
        case 1
            print( '-dpng' ,  '-r100' ,...
                          strcat(files{i}(5:end) , '.png') );
            fprintf('Saving figure \n\n')
    end

    % Close figure?
    switch closeFig
        case 1
            close
    end


end % End of for-loop
```

```
%
    ------------------------------------------------------------------------
```

A.3 D3100processing

```
% Script to process and plot data from BinaryImport.m
%
%
% --- CHANGELOG ---
% v 1.4
% - Implemented plotting of calibration curve rho(R)
% - Implemented plotting of SIMS and SSRM data in same figure
%
% v 2.0
% - Restructured to enable plotting of SCM data
%     from BinaryImport v3
% - Rewored plotting scheme
%
clear

% ---------------------------- Input -----------------------------

% Directory and filename:
% For windows
fdir = ...
  'C:\Users\jonborg\Dropbox\Skole\UiO\Thesis\Experiments\
    SSRM\GaZO-1100c160min\20160303' ;
% For linux
%fdir = '/home/jon/Dropbox/Skole/UiO/Thesis/Experiments/SSRM/GZO
   -1000';
% For both
fname = 'jon_20160303_gazo6-1100c160min.001' ;

% Amount of rotation, positive values yields clockwise rotation
rotationFactor = -0.1;

% Select which plots to dislay.
% Choices:
%          - 'subplots' for 2x2 subplots
%          - 'separate' for processed topo, data2 + avg., textbox
%          - 'SIMS' for SSRM/SCM vs SIMS curves,
%             see line 210 for SIMS module.
%           - 'calCurve' for plotting R vs. nominal resistivity
whatToPlot = 'separate';


% Select whether plots should have titles. 0 = no, 1 = yes.
plotTitles = 0;

% Select size of separate figures. 0 = standalone, 1 = subfigures
plotSize = 1;

% Select wheteher topo image should be planefit. 0 = no, 1 = yes.
planefit = 1;

% Select whether data should be flipped left-right so x-axes become
% measure of depth when sample edge faces right. 0 = no, 1 = yes.
lrflip = 0;

% Details for textbox
probeType = '' ;
```

```
plotNotes = '' ;

% Predetermined y-limits for avg. data2. 0 = no, 1 = yes.
setYlim = 1;
ylimits = [ 1e8 , 1e12 ];

% Predetermined y-ticks for avg. data2. 0 = no, 1 = yes.
setYticks = 1;
yTicks = [ 1e8 , 1e9, 1e10 , 1e11 , 1e12 ];% , 1e12 ];

% Invert y-axis?
% imgsc inverts by default, set Y-axis to 'normal' to invert or
%   'reverse' to keep imgsc default
yaxisDirection = 'normal' ;

% ------------------------------------------------------------------



% Load data from import script
[ topo , data2 , samplesPerLine , numlines , biasVoltage ,...
   scanSize , datatype ] = BinaryImport_v2( fname , fdir ) ;

% Convert scan size to microns
scanSize = scanSize/1000;

% Generate padding for use when rotating
padded data2img = zeros( samplesPerLine , 2 * samplesPerLine ) ;
paddedTopoImg = zeros( samplesPerLine , 2 * samplesPerLine ) ;

% Find center of padded image in x-direction
centerX = 0.5 * size( padded data2img , 2 ) ;

% Define start and stop indices for insertion into padding
startX = centerX - 0.5 * samplesPerLine ;
stopX  = centerX + 0.5 * samplesPerLine - 1 ;

% Insert images in center of padding
padded data2img( : , startX : stopX ) = data2( : , : ) ;
paddedTopoImg( : , startX : stopX ) = topo( : , : ) ;



% ------------------------- Straightening -------------------------

counter1 = 0 ;
for i = ( samplesPerLine / 2 ) + 1 : samplesPerLine
  rotated data2img( i , : ) = ...
      circshift(padded data2img( i , : ) ,...
            [ 0 , fix( rotationFactor * ( counter1 + 1 ) ) ] ) ;
  rotatedTopoImg( i , : ) = ...
      circshift(paddedTopoImg( i , : ) ,...
            [ 0 , fix( rotationFactor * ( counter1 + 1 ) ) ] ) ;
  counter1 = counter1 + 1 ;
end

counter2 = 0 ;
for i = ( samplesPerLine / 2 ) : -1 : 1
```

```
  rotateddata2img( i , : ) = ...
      circshift(paddeddata2img( i , : ) ,...
            [ 0 , - fix( rotationFactor * counter2 ) ] ) ;
  rotatedTopoImg( i , : ) = ...
      circshift(paddedTopoImg( i , : ) ,...
            [ 0 , - fix( rotationFactor * counter2 ) ] ) ;
  counter2 = counter2 + 1 ;
end

% After rotating image, at least two corners are padded with zeros.
% Find indices of these zeros. As Topo and SSRM images are rotated
% by the same amount, only need to find zeros in one of them.
if rotationFactor < 0
    xmin = find( rotateddata2img( 1 , : ) , 1 , 'first' ) ;
    xmax = find( rotateddata2img( end , : ) , 1 , 'last' ) ;
else
    xmin = find( rotateddata2img( end , : ) , 1 , 'first' ) ;
    xmax = find( rotateddata2img( 1 , : ) , 1 , 'last' ) ;
end

% Remove zeros
croppeddata2img = rotateddata2img( : , xmin : xmax ) ;
croppedTopoImg = rotatedTopoImg( : , xmin : xmax ) ;

% -------------------------------------------------------------------



% -------------------- Planefitting --------------------------------

planefitTopoImg = croppedTopoImg ;

switch planefit
    case 1
        % Calculate slope of each line of topo image
        topoSlope = ...
                  croppedTopoImg( : , end ) - croppedTopoImg( : , 1
                      ) ;

        % Calculate average slope
        avgSlope = sum( topoSlope , 1 ) / size( topoSlope , 1 ) ;

        % Weighted subtraction of slope from original data
        i = 0 ;
        for i = 1 : size( croppedTopoImg , 2 )
            planefitTopoImg( : , i ) = ...
              planefitTopoImg( : , i ) - ...
                            ( avgSlope * i / size( croppedTopoImg ,
                                2 ) ) ;
          i = i + 1;
        end


        % Calculate slope of each column. topoSlope no longer
                % needed, so reuse this variable here
        topoSlope = ...
                  planefitTopoImg( end , : ) - planefitTopoImg( 1 ,
                      : );
```

```
        % Calculate average slope
        avgSlope = sum( topoSlope , 1 ) / size( topoSlope , 1 );

        % Subtract slope from image
        i = 0 ;
        for i = 1 : size( croppedTopoImg , 1 )
            planefitTopoImg( i , : ) = ...
                planefitTopoImg( i , : ) - ...
                                ( avgSlope * i / size(
                                    croppedTopoImg , 1 ) ) ;
            i = i + 1;
        end
end

% ------------------------------------------------------------------



% ------------------- Resistance averaging procedure --------------

% Calculate average value of each column of data2. Average of
% column n is taken as sum of elements in column n divided by
% the # of elements in the column.
disp('Calculating avg. resistance')
data2average = ...
  sum( croppeddata2img , 1 ) ./ size( croppeddata2img , 1 ) ;

% If data2 is SSRM, convert average values from volts to ohms
switch datatype
    case 'Resistance'
        if biasVoltage > 0
            sign = -1 ;
        elseif biasVoltage < 0
            sign = 1 ;
        end
        data2average = 1e6 ./ 10.^( sign * data2average ) ;
        avgYlabel = 'Resistance [\Omega]';

    case 'dC/dV Amp'
        avgYlabel = 'dC/dV [V]';

    case 'dC/dV Phase'
        avgYlabel = strcat('dC/dV Phase', '[', char(176) , ']')

    case 'SCM Data'
        avgYlabel = 'SCM Data [V]'
end

% Convert x-indices to distance
xlength = ...
  linspace( 0 , scanSize * ( xmax - xmin + 1 ) / samplesPerLine,...
    ( xmax - xmin + 1 )  ) ;

% ------------------------------------------------------------------
```

```
% ------------------ Flip left / right ---------------------------

switch lrflip
    case 1
        planefitTopoImg = fliplr( planefitTopoImg );
        croppeddata2img = fliplr( croppeddata2img );
        data2average = fliplr( data2average );
end

% ----------------------------------------------------------------



% Set limits for plot of original image
plotLimits1 = [ 0 , scanSize ] ;

% Set limits for plot of rotated image
plotLimits2 = ...
  [ 0 , scanSize * ( xmax - xmin + 1 ) / samplesPerLine ] ;


% Extract sample name from filename.
%   Find index of underscore preceeding sample name
    uScores = regexp( fname , '_' ) ;
    nameStartIdx = uScores(2) + 1 ;

%   Find index of point following samplename
    points = regexp( fname , '\.' ) ;
    nameStopIdx = points( end ) - 1 ;

    sampleName = fname( nameStartIdx : nameStopIdx ) ;

%   Capitalise initial letter
    sampleName = ...
          [ upper( sampleName( 1 ) ) sampleName( 2 : end ) ];



% Set plot parameters
alw = 0.5; % axis line width
lw = 1; % line width
msz = 8; % marker size

switch plotSize
    case 0
        % Plot parameters for single figure
        width = 10; % [cm]
        height = 7; % [cm]
        fsz = 2; % font size
    case 1
        % Plot parameters for 2-figure subplots
        width = 6; % [cm]
        height = 5; % [cm]
        fsz = 9; % font size
end
```

```
% ----------------------- Import SIMS data ----------------------

switch whatToPlot
    case 'SIMS'
        SIMSdir = ...
                  'C:\Users\jonborg\Dropbox\Skole\UiO\Thesis\
                     Experiments\SIMS\GZO-1000';
        SIMSdepthFile = 'SIMSdepth.txt';
        SIMSconcFile = 'SIMSconc.txt';

        cd (SIMSdir)

        SIMSdepth = fileread( SIMSdepthFile );
        SIMSdepth = strsplit( SIMSdepth, '\n' );
        SIMSdepth = SIMSdepth';
        SIMSdepth = str2double( SIMSdepth );
        %SIMSdepth = flipud( SIMSdepth );


        SIMSconc = fileread( SIMSconcFile );
        SIMSconc = strsplit( SIMSconc , '\n' );
        SIMSconc = SIMSconc';
        SIMSconc = str2double( SIMSconc );
        %SIMSconc = flipud( SIMSconc );

        % Plotting w.o. plotyy()
        figure( 'name' , 'SIMS vs. SSRM' )
        set(gcf,...
                        'units' , 'centimeters',...
                        'Position' , [ 5 5 width+1 height],...
                        'OuterPosition' , [4 4 width+2.5 height
                           +3.5] );

        ssrmcurve = ...
                  semilogy( xlength , fliplr( data2average ) ,...
                   'Color' , 'b' );
        ax1 = gca;
        set(ax1,...
            'units','centimeters',...
            'XColor','b',...
            'YColor','b',...
            'FontSize',fsz,...
            'LineWidth',alw,...
            'box','off',...
            'Xlim',[0 SIMSdepth(end-150)],...
            'YTick',[1e4 1e6 1e8 1e10 1e12 1e14 1e16])
        xlabel('Depth [\mum]')
        ylabel('Resistance [\Omega]')
        grid on
        set(ssrmcurve,...
            'LineWidth',lw)

        ax1_pos = get( ax1 , 'Position' );
        ax2 = axes('units','centimeters','Position',ax1_pos);

        simscurve = ...
                  semilogy( ax2 , SIMSdepth , SIMSconc ,...
                    'Parent' , ax2 , 'Color' , 'k' );
```

```
        set(ax2,...
            'units','centimeters',...
            'XAxisLocation','top',...
            'YAxisLocation','right',...
            'Color','none',...
            'XColor','k',...
            'YColor','k',...
            'FontSize',fsz,...
            'LineWidth',alw,...
            'box','off',...
            'Xlim',[SIMSdepth(95) SIMSdepth(end-150)],...
            'YTick',[1e18 1e19 1e20 1e21 1e22])
        xlabel('Depth [\mum]')
        ylabel('Concentration [cm^{-3}]')
        set(simscurve,...
            'LineWidth',lw,...
            'LineStyle','-.')

        legend([ssrmcurve,simscurve],{'SSRM','SIMS'})

        cd(fdir)
end

% ------------------------------------------------------------------



% -------------------- Calibration curve -------------------------

switch whatToPlot
    case 'calCurve'
        % Nominal resistivities, used as indices for
                % the resistivity lookup table
        Ag = 1;
        ZnO = 2;
        AZO = 3;
        Cu2O = 4; % from:
                % http://www.journalamme.org/papers_vol24_1/24121.
                   pdf

        % Resistivity lookup table
        rlt = [ 1e-5 , 1e-1 , 1e-3 , 1e4 ];

        % Extracting resistivities from lookup table
        rv = [ rlt(1) , rlt(3) , rlt(2) , rlt(4) ];

        % Indices of Measured resistances, found from
                % red line in left subplot
        Ag_idx = 30;
        ZnO_idx = 30;
        AZO_idx = 30;
        Cu2O_idx = 30;

        % Resistance vector
        R = data2average; % abbreviation
        Rv = [R(Ag_idx) , R(AZO_idx) , R(ZnO_idx) , R(Cu2O_idx) ];

        % Parameters for help plot
```

```
        avgres = sum(data2average) / size(data2average,2) ;
        x2 = ...
                  linspace(1,size(data2average,2),size(data2average
                     ,2));
        baseline = ones( 1 , size(data2average,2)) * avgres;

        % Generate help plot (left) and calibration curve (right)
        figure('name' , 'Resistivity vs. resistance')
        subplot( 1 , 2 , 1 )
        [ ax , h1 , h2 ] = ...
                  plotyy( xlength , data2average ,...
                    x2 , baseline , @semilogy );
        set( ax(1) , 'Xlim' , [xlength(1) xlength(end)] );
        set(ax(2),...
                    'XaxisLocation' , 'top',...
                        'Xlim' , [x2(1) x2(end)],...
                        'xcolor' , 'r',...
                        'Xgrid' , 'on' );
        set(h2,'Marker','*','MarkerSize',12,'color','r');
        title('Average resistance')
        xlabel('Depth [\mum]')
        ylabel('Resistance [\Omega]')

        subplot( 1 , 2 , 2 )
        loglog( Rv , rv , '*-')
        title('Calibration curve')
        xlabel('Resistance [\Omega]')
        ylabel('Resistivity [\Omegacm]')
        grid on
end

% ------------------------------------------------------------------



% ------------------------- Plotting -------------------------------

% Check if subplots or separate figures should be plotted
switch whatToPlot
    case 'subplots'
        % Setting overall figure size
        figure('units' , 'normalized',...
                       'position' , [.1 .1 .5 .63 ] )

        % Topography
        subplot(2,2,1, 'position' , [0.1 0.5838 0.4 0.3412 ] )
        set( gca , 'YDir' , yaxisDirection )

        if plotTitles == 1 && planefit == 0
            imagesc( plotLimits2 , plotLimits1 , croppedTopoImg ) ;
            title ( 'Topography' , 'FontSize' , 14 )
        elseif plotTitles == 1 && planefit == 1
            imagesc( plotLimits2 , plotLimits1 , planefitTopoImg );
            title ( 'Planefit Topography' , 'FontSize' , 14 )
        else
            imagesc( plotLimits2 , plotLimits1 , planefitTopoImg );
        end
        colorbar('eastoutside')
```

```
xlabel(colorbar,'[nm]')

xlabel( 'Distance [\mum]' )
ylabel( 'Distance [\mum]' )



% Data 2
subplot(2,2,2)
set( gca, 'Position' , [ 0.6 , 0.5838 , 0.3347 , 0.3412 ] )
set( gca , 'YDir' , yaxisDirection )

imagesc( plotLimits2 , plotLimits1 , croppeddata2img ) ;

% Add title if wanted
if plotTitles == 1
    title ( 'SSRM' , 'FontSize' , 14 )
end
xlabel( 'Distance [\mum]' )
ylabel( 'Distance [\mum]' )


% Average data 2
subplot(2,2,4)
set( gca , 'Position' , [ 0.6 , 0.11 , 0.3347, 0.3412 ] )


semilogy(xlength,data2average,...
    'LineWidth',lw ,...
    'MarkerSize',msz ,...
    'Color','b' );
set(gca,...
            'YMinorGrid' , 'off',...
                'YGrid' , 'off',...
                'YMinorTick' , 'off')

if plotTitles == 1
    title( ['Average' ,' ', datatype] , 'FontSize' , 14 )
end
xlabel( 'Distance [\mum]')
ylabel( avgYlabel)% , 'FontSize' , 14 )
xlim([0,scanSize * ( xmax - xmin + 1 ) / samplesPerLine ])

switch setYlim
    case 1
    ylim( ylimits )
end
switch setYticks
    case 1
    set( gca , 'YTick' , yTicks )
end
grid on


% Textbox
subplot(2,2,3)
set( gca , 'Position' , [ 0.1 , 0.11 , 0.3347 , 0.3412 ] )
```

```
        text( 0.25 , 1.05 ,...
                  sprintf('%s' , 'Measurement Details') , 'FontSize
                     ' , 14 )
        text( 0 , 0.9 ,...
                  sprintf(' Sample: %s ' , sampleName ) , 'FontSize
                     ' , 14 )
        text( 0 , 0.8 ,...
                  sprintf(' Scan size: %.1f \\mum ' , scanSize ) ,
                     ...
                    'FontSize' , 14 )
        text( 0 , 0.7 ,...
                  sprintf(' Samples/line: %.f ' , samplesPerLine )
                     ,...
                    'FontSize' , 14 )
        text( 0 , 0.6 ,...
                  sprintf(' Bias voltage: %.f mV ' , biasVoltage )
                     ,...
                    'FontSize' , 14 )
        text( 0 , 0.5 ,...
                  sprintf(' Probe type: %s ' , probeType ) ,...
                    'FontSize' , 14 )
        text( 0 , 0.4 ,...
                  sprintf(' Filename: %s ' , fname(5:end) ) ,...
                    'FontSize' , 14 , 'Interpreter' , 'none' )
        text( 0 , 0.3 ,...
                  sprintf(' Notes: %s ' , plotNotes  ) , 'FontSize'
                      , 14 )
        axis off

% ------------------------------------------------------------------

% If separate figures are to be plotted
    case 'separate'
        % Topography figure
        figure(1)
        set(gcf,...
                    'units' , 'centimeters',...
                        'Position', [ 5 5 width height],...
                        'OuterPosition',[4 4 width+1.75 height
                           +3.25] );
        set(gca,...
                    'units' , 'centimeters',...
                        'FontSize', fsz,...
                        'LineWidth', lw,...
                        'Position', [ 1.1 1 width-1.5 height-1],...
                        'YMinorGrid' , 'off' ,...
                        'YGrid' , 'on',...
                        'YDir', yaxisDirection);

        if plotTitles == 1 && planefit == 0
            imagesc( plotLimits2 , plotLimits1 , croppedTopoImg ) ;
            title ( 'Topography' , 'FontSize' , fsz )
        elseif plotTitles == 1 && planefit == 1
            imagesc( plotLimits2 , plotLimits1 , planefitTopoImg )
               ;
            title ( 'Planefit Topography' , 'FontSize' , fsz )
        else
            imagesc( plotLimits2 , plotLimits1 , planefitTopoImg )
```

```
        ;
end
colormap jet
pos = get(gcf,'Position');
c = colorbar('units','centimeters',...
                     'location','manual',...
                                'position',[width-0.3 1
                                   0.3 height-1]);
set(c,...
            'units' , 'centimeters',...
                'FontSize', fsz,...
                'LineWidth', lw);

ylabel( c , 'Height [nm]', 'FontSize' , fsz)

xlabel( 'Distance [\mum]' )
ylabel( 'Distance [\mum]' )


% Data 2 figure
figure(2)
    set(gcf,...
                    'units' , 'centimeters',...
                        'Position', [ 5 5 width height],...
                        'OuterPosition',[4 4 width+1.25
                           height+3] );
    set(gca,...
                    'units' , 'centimeters',...
                        'FontSize', fsz,...
                        'LineWidth', lw);
    imagesc( plotLimits2 , plotLimits1 , croppeddata2img );

    % Add title if wanted
    if plotTitles == 1
        title ( datatype , 'FontSize' , 14 )
    end

    colormap jet
    xlabel( 'Distance [\mum]' )
    ylabel( 'Distance [\mum]' )
    set( gca , 'YDir' , yaxisDirection )

% Averaged data 2
figure(3)
set(gcf,...
            'units' , 'centimeters',...
                'Position', [ 5 5 width+1 height],...
                'OuterPosition',[4 4 width+2 height+3] );
set(gca,
            'units' , 'centimeters',...
                'FontSize', fsz,...
                'LineWidth', lw,...
                'YMinorGrid', 'off');

semilogy(xlength,data2average,...
                        'LineWidth',lw ,...
                        'MarkerSize',msz ,...
                        'Color','b' );
```

```
        if plotTitles == 1
            title( ['Average' ,' ', datatype] , 'FontSize' , 14 )
        end

        xlabel( 'Distance [\mum]')
        ylabel( avgYlabel)
        xlim( [0, scanSize * ( xmax - xmin + 1 ) / samplesPerLine])

        switch setYlim
            case 1
                ylim( ylimits )
        end
        switch setYticks
            case 1
                set( gca , 'YTick' , yTicks )
        end
        grid on

        % Textbox
        figure(4)
        text( 0.25 , 1.05 ,...
                  sprintf('%s' , 'Measurement Details') , 'FontSize
                     ' , 14 )
        text( 0 , 0.9 ,...
                  sprintf(' Sample: %s ' , sampleName ) , 'FontSize
                     ' , 14 )
        text( 0 , 0.8 ,...
                  sprintf(' Scan size: %.1f \\mum ' , scanSize ) ,
                     ...
                    'FontSize' , 14 )
        text( 0 , 0.7 ,...
                  sprintf(' Samples/line: %.f ' , samplesPerLine )
                     ,...
                    'FontSize' , 14 )
        text( 0 , 0.6 ,...
                  sprintf(' Bias voltage: %.f mV ' , biasVoltage )
                     ,...
                    'FontSize' , 14 )
        text( 0 , 0.5 ,...
                  sprintf(' Probe type: %s ' , probeType ) ,...
                    'FontSize' , 14 )
        text( 0 , 0.4 ,...
                  sprintf(' Filename: %s ' , fname(5:end) ) ,...
                    'FontSize' , 14 , 'Interpreter' , 'none' )
        text( 0 , 0.3 ,...
                  sprintf(' Notes: %s ' , plotNotes  ) , 'FontSize'
                      , 14 )
        axis off

end % end of what to plot
```

Bibliography

[1] "IPCC, 2013: Summary for Policymakers," in *Climate Change 2013: The Physical Science Basis. Contribution of Working Group I to the Fift Assessment Report of the Intergovernmental Panel on Climate Change* (T. F. Stocker, D. Qin, G.-K. Plattner, M. Tignor, S. K. Allen, J. Boschung, A. Nauels, Y. Xia, V. Bex, and P. M. Midgely, eds.), Cambridge University Press, 2013. [Online; accessed 1–March–2016.].

[2] International Energy Agency, *Energy and Climate Change – World Energy Outlook Special Report*. 2015. [Online; accessed 1–March–2016.].

[3] M. A. Green, K. Emery, Y. Hishikawa, W. Warta, and E. D. Dunlop, "Solar cell efficiency tables (version 46)," *Progress in Photovoltaics: Research and Applications*, vol. 23, no. 7, pp. 805–812, 2015.

[4] W. Shockley and H. J. Queisser, "Detailed Balance Limit of Efficiency of p-n Junction Solar Cells," *Journal of Applied Physics*, vol. 32, no. 3, pp. 510–519, 1961.

[5] B. G. Streetman and S. K. Banerjee, *Solid state electronic devices*. Pearson Prentice-Hall, sixth ed., 2006.

[6] J. Nelson, *The Physics of Solar Cells*. Imperial College Press, 2003.

[7] R. J. D. Tilley, *Understanding solids: the science of materials*. John Wiley & Sons Ltd, 2004.

[8] S. A. Campbell, *Fabrication engineering at the micro- and nanoscale*. Oxford university press, fourth ed., 2008.

[9] D. S. Sholl and J. A. Steckel, *Density Functional Theory: A Practical Introduction*. John Wiley & Sons, 2009.

[10] J. H. Davies, *The Physics of Low-Dimensional Semiconductors: An Introduction*. Cambridge University Press, 1998.

[11] K. Momma and F. Izumi, "*VESTA3* for three-dimensional visualization of crystal, volumetric and morphology data," *Journal of Applied Crystallography*, vol. 44, no. 6, pp. 1272–1276, 2011.

[12] T. Heinzel, *Mesoscopic Electronics in Solid State Nanostructures*. Wiley-VCH, third ed., 2010.

[13] M. Brandt, H. von Wenckstern, G. Benndorf, H. Hochmuth, M. Lorenz, and M. Grundmann, "Formation of a two-dimensional electron gas in ZnO/MgZnO single heterostructures and quantum wells," *Thin Solid Films*, vol. 518, no. 4, pp. 1048–1052, 2009.

[14] J. Ye, S. Ter Lim, S. Gu, H. H. Tan, C. Jagadish, and K. L. Teo, "Origin and transport properties of two-dimensional electron gas at ZnMgO/ZnO interface grown by MOVPE," *Physica Status Solidi C: Current Topics in Solid State Physics*, vol. 10, no. 10, pp. 1268–1271, 2013.

[15] D. Lin, J. Wu, C. Hung, C. Lu, Y. Huang, C.-T. Liang, and N. Chen, "Optical investigation of an AlGaN/GaN interface with the presence of a two-dimensional electron gas," *Physica E: Low-dimensional Systems and Nanostructures*, vol. 43, no. 1, pp. 125–129, 2010.

[16] Ü. Özgür, Y. I. Alivov, C. Liu, A. Teke, M. A. Reshchikov, S. Doğan, V. Avrutin, S.-J. Cho, and H. Morkoç, "A comprehensive review of ZnO materials and devices," *Journal of Applied Physics*, vol. 98, no. 4, p. 041301, 2005.

[17] A. Kołodziejczak-Radzimska and T. Jesionowski, "Zinc Oxide From Synthesis to Application: A Review," *Materials*, vol. 7, no. 4, pp. 2833–2881, 2014.

[18] O. Madani Ghahfarokhi, K. Chakanga, S. Geissendoerfer, O. Sergeev, K. von Maydell, and C. Agert, "DC-sputtered ZnO:Al as transparent conductive oxide for silicon heterojunction solar cells with μc-Si:H emitter," *Progress in Photovoltaics: Research and Applications*, 2014.

[19] S. B. Zhang, S.-H. Wei, and A. Zunger, "Intrinsic n-type versus p-type doping asymmetry and the defect physics of ZnO," *Phys. Rev. B*, vol. 63, p. 075205, 2001.

[20] X. Jiang, J. Shi, M. Zhang, H. Zhong, P. Huang, Y. Ding, X. Cao, M. Wu, and Z. Liao, "Breakthrough of the p-type doping bottleneck in ZnO by inserting an ultrathin ZnX (X=S, Se and Te) layer doped with N_x or Ag_{zn}," *Journal of Physics D: Applied Physics*, vol. 49, no. 9, p. 095104, 2016.

[21] Q. Li, J. Zhang, Z. Zhang, F. Li, and X. Hou, "Electron transport in ZnMgO/ZnO heterostructures," *Semiconductor Science and Technology*, vol. 29, no. 11, p. 115001, 2014.

[22] S. J. Pearton, D. P. Norton, K. Ip, Y. W. Heo, and T. Steiner, "Recent progress in processing and properties of ZnO," *Progress in Materials Science*, vol. 50, no. 3, pp. 293–340, 2005.

[23] V. Quemener, *Electrical Characterization of Bulk and Thin Film Zinc Oxide*. PhD thesis, University of Oslo, 2012.

[24] W.-W. Feng, S. Cho, M.-S. Wang, and D. D. Dung, "Co-contribution of hydrogen impurities and native defects might be the answer for the n-type conductivity in ZnO," *Physics Letters A*, vol. 380, no. 3, pp. 480–484, 2016.

[25] L. Vines, R. Schifano, M. Schofield, and B. G. Svensson, "Impurity migration in bulk and thin-film ZnO," *PHYSICA SCRIPTA*, vol. T148, 2012.

[26] L. Vines, E. V. Monakhov, R. Schifano, W. Mtangi, F. D. Auret, and B. G. Svensson, "Lithium and electrical properties of ZnO," *Journal of Applied Physics*, vol. 107, no. 10, 2010.

[27] K. M. Johansen, L. Vines, T. S. Bjørheim, R. Schifano, and B. G. Svensson, "Aluminum Migration and Intrinsic Defect Interaction in Single-Crystal Zinc Oxide," *Phys. Rev. Applied*, vol. 3, p. 024003, 2015.

[28] K. M. Johansen, J. S. Christensen, E. V. Monakhov, A. Y. Kuznetsov, and B. G. Svensson, "Deuterium diffusion and trapping in hydrothermally grown single crystalline ZnO," *Applied Physics Letters*, vol. 93, no. 15, 2008.

[29] K. S. Chan, J. D. Ye, P. Parkinson, E. Monakhov, K. M. Johansen, L. Vines, B. G. Svensson, C. Jagadish, and J. Wong-Leung, "Structural and optical properties of H implanted ZnO," in *COMMAD 2012*, pp. 219–220, 2012.

[30] P. T. Neuvonen, L. Vines, B. G. Svensson, and A. Y. Kuznetsov, "Intrinsic Point-Defect Balance in Self-Ion-Implanted ZnO," *Phys. Rev. Lett.*, vol. 110, p. 015501, 2013.

[31] A. Y. Azarov, K. E. Knutsen, P. T. Neuvonen, L. Vines, B. G. Svensson, and A. Y. Kuznetsov, "Impurity sublattice localization in ZnO revealed by Li marker diffusion," *Physical Review Letters*, vol. 110, p. 175503, 2013.

[32] A. Y. Azarov, A. Hallén, X. L. Du, P. Rauwel, A. Y. Kuznetsov, and B. G. Svensson, "Effect of implanted species on thermal evolution of ion-induced defects in ZnO," *Journal of Applied Physics*, vol. 115, no. 7, 2014.

[33] S. Sasa, T. Tamaki, K. Koike, M. Yano, and M. Inoue, "Origin of high-density two-dimensional electron gas in ZnO/ZnMgO heterostructures - art. no. 012030," in *International Symposium on Advanced Nanodevices and Nanotechnology* (S. M. Goodnick and D. K. Ferry, eds.), vol. 109, pp. 12030–12030, 2008.

[34] H. Tampo, H. Shibata, K. Maejima, A. Yamada, K. Matsubara, P. Fons, S. Kashiwaya, S. Niki, Y. Chiba, T. Wakamatsu, and H. Kanie, "Polarization-induced two-dimensional electron gases in ZnMgO/ZnO heterostructures," *Applied Physics Letters*, vol. 93, no. 20, 2008.

[35] J. D. Ye, S. Pannirselvam, S. T. Lim, J. F. Bi, X. W. Sun, G. Q. Lo, and K. L. Teo, "Two-dimensional electron gas in Zn-polar ZnMgO/ZnO heterostructure grown by metal-organic vapor phase epitaxy," *Applied Physics Letters*, vol. 97, no. 11, 2010.

[36] K. Koike, I. Nakashima, K. Hashimoto, S. Sasa, M. Inoue, and M. Yano, "Characteristics of a $Zn_{0.7}Mg_{0.3}O$?ZnO heterostructure field-effect transistor grown on sapphire substrate by molecular-beam epitaxy," *Applied Physics Letters*, vol. 87, no. 11, 2005.

[37] K. Koike, D. Takagi, M. Kawasaki, T. Hashimoto, T. Inoue, K. ichi Ogata, S. Sasa, M. Inoue, and M. Yano, "Ion-Sensitive Characteristics of an Electrolyte-Solution-Gate ZnO/ZnMgO Heterojunction Field-Effect Transistor as a Biosensing Transducer," *Japanese Journal of Applied Physics*, vol. 46, no. 10L, p. L865, 2007.

[38] S. Sasa, T. Hayafuji, M. Kawasaki, K. Koike, M. Yano, and M. Inoue, "Improved Stability of High-Performance ZnO/ZnMgO Hetero-MISFETs," *IEEE Electron Device Letters*, vol. 28, no. 7, pp. 543–545, 2007.

[39] F. Djamdji and R. Blunt, "Hall-mobility profiling in high-electron-mobility transistor structures," *Materials Science and Engineering: B - Solid State Materials for Advanced Technology*, vol. 20, no. 1-2, pp. 77–81, 1993.

[40] P. De Wolf, M. Geva, C. L. Reynolds, T. Hantschel, W. Vandervorst, and R. B. Bylsma, "Two-dimensional carrier profiling of InP-based structures using scanning spreading resistance microscopy," *Journal of Vacuum Science & Technology A*, vol. 17, no. 4, pp. 1285–1288, 1999.

[41] St. J. Dixon-Warren, R. P. Lu, S. Ingrey, D. Macquistan, T. Bryskiewicz, G. Smith, and B. Bryskiewicz, "Scanning spreading resistance microscopy study of a metalorganic chemical vapor deposited grown InP optoelectronic structure," *Journal of Vacuum Science & Technology A*, vol. 19, no. 4, pp. 1752–1757, 2001.

[42] J. Osterman, A. Hallén, and S. Anand, "Carrier profiling of Al-doped 4H-SiC by scanning spreading resistance microscopy," *Applied Physics Letters*, vol. 81, no. 16, pp. 3004–3006, 2002.

[43] E. V. Monakhov, J. S. Christensen, K. Maknys, B. G. Svensson, and A. Y. Kuznetsov, "Hydrogen implantation into ZnO for n^+-layer formation," *Applied Physics Letters*, vol. 87, no. 19, 2005.

[44] K. M. Johansen, R. Schifano, E. V. Monakhov, and B. G. Svensson, "Investigation of contact material for cross section scanning spreading resistance microscopy on zinc oxide," *physica status solidi (c)*, vol. 5, no. 10, pp. 3361–3363, 2008.

[45] J. R. Matey and J. Blanc, "Scanning capacitance microscopy," *Journal of Applied Physics*, vol. 57, no. 5, pp. 1437–1444, 1985.

[46] J. J. Kopanski, "Scanning capacitance microscopy for electrical characterization of semiconductors and dielectrics," in *Scanning probe microscopy: Electrical and electromechanical phenomena at the nanoscale* (S. Kalinin and A. Gruverman, eds.), vol. 1, ch. 3, pp. 88–112, Springer science+business media, 2007.

[47] S. Anand, C. Carlström, E. R. Messmer, S. Lourdudoss, and G. Landgren, "Doping landscapes in the nanometer range by scanning capacitance microscopy," *Applied Surface Science*, vol. 144-145, pp. 525–529, 1999.

[48] W. Brezna, H. Wanzenböck, A. Lugstein, E. Bertagnolli, E. Gornik, and J. Smoliner, "Scanning capacitance microscopy investigations of focused ion beam damage in silicon," *Physica E: Low-dimensional Systems and Nanostructures*, vol. 19, no. 1-2, pp. 178–182, 2003.

[49] M. Lamhamdi, F. Cayrel, E. Frayssinet, A. Bazin, A. Yvon, E. Collard, Y. Cordier, and D. Alquier, "Two-dimensional dopant profiling of gallium nitride p-n junctions by scanning capacitance microscopy," *Nuclear Instruments and Methods in Physics Research Section B: Beam Interactions with Materials and Atoms*, vol. 372, pp. 67–71, 2016.

[50] O. Douhéret, K. Maknys, and S. Anand, "Scanning capacitance microscopy investigations of InGaAs/InP quantum wells," *Thin Solid Films*, vol. 459, no. 1-2, pp. 67–70, 2004.

[51] A. Krtschil, A. Dadgar, N. Oleynik, J. Bläsing, A. Diez, and A. Krost, "Local p-type conductivity in zinc oxide dual-doped with nitrogen and arsenic," *Applied Physics Letters*, vol. 87, no. 26, 2005.

[52] L. Wang, J. Laurent, J. M. Chauveau, V. Sallet, F. Jomard, and G. Brémond, "Nanoscale calibration of n-type zno staircase structures by scanning capacitance microscopy," *Applied Physics Letters*, vol. 107, no. 19, 2015.

[53] P. Eyben, *Scanning spreading resistance microscopy: high resolution two-dimensional carrier profiling of semiconductor structures*. PhD thesis, Katholieke Universiteit Leuven, 2004.

[54] C. C. Williams, "Two-dimensional dopant profiling by scanning capacitance microscopy," *Annual Review of Materials Science*, vol. 29, pp. 471–504, 1999.

[55] E. V. Monakhov, A. Y. Kuznetsov, J. S. Christensen, K. Maknys, and B. G. Svensson, "Evolution of high-dose implanted hydrogen in ZnO," *Superlattices and Microstructures*, vol. 38, no. 4-6, pp. 472–478, 2005. E-MRS 2005 Symposium G:ZnO and Related Materials Part 12005 European Materials Research Society Spring Meeting.

[56] H. K. Wickramasinghe, "Scanned-probe microscopes," *Scientific American*, vol. 261, no. 4, pp. 98–105, 1989.

[57] J. Loos, "The art of SPM: Scanning probe microscopy in materials science," *Advanced Materials*, vol. 17, no. 15, pp. 1821–1833, 2005.

[58] Username: SecretDisc, "AFM (used) cantilever in Scanning Electron Microscope, magnification 1000x.GIF." `https://commons.wikimedia.org/wiki/File:AFM_(used)_cantilever_in_Scanning_Electron_Microscope,_magnification_1000x.GIF`. [Illustration published to Wikimedia commons under the CC-BY-SA 3.0 licence. Accessed 21-September-2015.].

[59] G. Binnig and H. Rohrer, "Scanning tunneling microscopy - from birth to adolescence." Nobel Lecture, 1986.

[60] G. Binnig, C. F. Quate, and C. Gerber, "Atomic force microscope," *Physical review letters*, vol. 56, pp. 930–933, mar 1986.

[61] W. Morris, "Atomic force microscopy," in *Encyclopedia of Materials: Science and Technology* (K. H. Jürgen Buschow, R. W. Cahn, M. C. Flemings, B. Ilschner, E. J. Kramer, S. Mahajan, and V. Patrick, eds.), pp. 1–6, Oxford: Elsevier, second ed., 2001.

[62] F. Giessibl and G. Binnig, "Investigation of the (001) cleavage plane of potassium bromide with an atomic force microscope at 4.2 K in ultra-high vacuum," *Ultramicroscopy*, vol. 42, pp. 281–289, 1992.

[63] F. J. Giessibl, "Atomic Resolution of the Silicon (111)-(7x7) Surface by Atomic Force Microscopy," *Science*, vol. 267, no. 5194, pp. 68–71, 1995.

[64] C. Frétigny, "Atomic force microscopy," in *Nanoscience* (C. Dupas, P. Houdy, and M. Lahmani, eds.), pp. 91–119, Springer Berlin Heidelberg, 2007.

[65] R. García and R. Pérez, "Dynamic atomic force microscopy methods," *Surface Science Reports*, vol. 47, no. 6-8, pp. 197–301, 2002.

[66] L. Zang, "University of Utah, MSE 6075: Nanoscale Probing and Imaging, lecture slides, Lecture 10." `http://www.eng.utah.edu/~lzang/images/Lecture_10_AFM.pdf`. [Accessed 22-October-2015.].

[67] T. Fukuma, J. I. Kilpatrick, and S. P. Jarvis, "Phase modulation atomic force microscope with true atomic resolution," *Review of Scientific Instruments*, vol. 77, no. 12, 2006.

[68] F. J. Giessibl, "Advances in atomic force microscopy," *Rev. Mod. Phys.*, vol. 75, pp. 949–983, 2003.

[69] Y. Martin, C. C. Williams, and H. K. Wickramasinghe, "Atomic force microscope-force mapping and profiling on a sub 100-Å scale," *Journal of Applied Physics*, vol. 61, no. 10, pp. 4723–4729, 1987.

[70] T. R. Albrecht, P. Grütter, D. Horne, and D. Rugar, "Frequency modulation detection using high-q cantilevers for enhanced force microscope sensitivity," *Journal of Applied Physics*, vol. 69, no. 2, pp. 668–673, 1991.

[71] N. Kobayashi, Y. J. Li, Y. Naitoh, M. Kageshima, and Y. Sugawara, "High-Sensitivity Force Detection by Phase-Modulation Atomic Force Microscopy," *Japanese Journal of Applied Physics*, vol. 45, no. 8L, p. L793, 2006.

[72] H. Hida, M. Shikida, K. Fukuzawa, S. Murakami, K. Sato, K. Asaumi, Y. Iriye, and K. Sato, "Development of self-vibration/detection afm probe using quartz tuning fork," *IEEJ Transactions on Electrical and Electronic Engineering*, vol. 4, no. 3, pp. 378–385, 2009.

[73] M. Heyde, M. Sterrer, H.-P. Rust, and H.-J. Freund, "Atomic resolution on MgO(001) by atomic force microscopy using a double quartz tuning fork sensor at low-temperature and ultrahigh vacuum," *Applied Physics Letters*, vol. 87, no. 8, 2005.

[74] F. J. Giessibl, "Atomic resolution on Si(111)-(7×7) by noncontact atomic force microscopy with a force sensor based on a quartz tuning fork," *Applied Physics Letters*, vol. 76, no. 11, pp. 1470–1472, 2000.

[75] D. C. D'Avanzo, C. Clare, and C. Dell'Oca, "Laser Interferometer Bevel Angle Measurement for Spreading Resistance Profiling," *Journal of The Electrochemical Society*, vol. 127, no. 12, pp. 2704–2708, 1980.

[76] S. M. Hu, "Between carrier distributions and dopant atomic distribution in beveled silicon substrates," *Journal of Applied Physics*, vol. 53, no. 3, pp. 1499–1510, 1982.

[77] C. M. Osburn, H. L. Berkowitz, J. M. Heddleson, R. J. Hillard, R. G. Mazur, and P. Rai-Choudhury, "Profiling of ultra-shallow complementary metal-oxide semiconductor junctions using spreading resistance: A comparison to secondary ion mass spectrometry," *Journal of Vacuum Science & Technology B*, vol. 10, no. 1, pp. 533–539, 1992.

[78] P. De Wolf, T. Clarysse, W. Vandervorst, J. Snauwaert, and L. Hellemans, "One- and two-dimensional carrier profiling in semiconductors by nanospreading resistance profiling," *Journal of Vacuum Science & Technology B*, vol. 14, no. 1, pp. 380–385, 1996.

[79] Electronics and Engineering Dictionary, "Spreading Resistance." `http://www.dictionaryofengineering.com/definition/spreading-resistance.html`, 2004. [Accessed 24-November-2015.].

[80] P. Eyben, D. Degryse, and W. Vandervorst, "On the spatial resolution of scanning spreading resistance microscopy : experimental assessment and electro-mechanical modeling," *AIP Conference Proceedings*, vol. 788, no. 1, pp. 264–269, 2005.

[81] P. De Wolf, M. Geva, T. Hantschel, W. Vandervorst, and R. B. Bylsma, "Two-dimensional carrier profiling of InP structures using scanning spreading resistance microscopy," *Applied Physics Letters*, vol. 73, no. 15, pp. 2155–2157, 1998.

[82] P. Eyben, N. Duhayon, D. Alvarez, and W. Vandervorst, "Assessing the resolution limits of scanning spreading resistance microscopy and scanning capacitance microscopy," *AIP Conference Proceedings*, vol. 683, no. 1, pp. 678–684, 2003.

[83] W. Vandervorst, P. Eyben, S. Callewaert, T. Hantschel, N. Duhayon, M. Xu, T. Trenkler, and T. Clarysse, "Towards routine, quantitative two-dimensional carrier profiling with scanning spreading resistance microscopy," *AIP Conference Proceedings*, vol. 550, no. 1, pp. 613–619, 2001.

[84] N. Duhayon, P. Eyben, M. Fouchier, T. Clarysse, W. Vandervorst, D. Álvarez, S. Schoemann, M. Ciappa, M. Stangoni, W. Fichtner, P. Formanek, M. Kittler, V. Raineri, F. Giannazzo, D. Goghero, Y. Rosenwaks, R. Shikler, S. Saraf, S. Sadewasser, N. Barreau, T. Glatzel, M. Verheijen, S. A. M. Mentink, M. von Sprekelsen, T. Maltezopoulos, R. Wiesendanger, and L. Hellemans, "Assessing the performance of two-dimensional dopant profiling techniques," *Journal of Vacuum Science & Technology B*, vol. 22, no. 1, pp. 385–393, 2004.

[85] D. Wolpert and P. Ampadu, *Managing Temperature Effects in Nanoscale Adaptive Systems*. Springer-Verlag New York, 2012.

[86] R. F. Egerton, *Physical Principles of Electron Microscopy*. Springer, 2005.

[87] Usernames: MarcoTolo, Steff, and ARTE, "Schema MEB (en).svg." `https://commons.wikimedia.org/wiki/File:Schema_MEB_%28en%29.svg`, 2010. [Illustrations published to Wikimedia commons under the CC-BY-SA 1.0 licence. Accessed 10-November-2015.].

[88] Australian Microscopy and Microanalysis Research Facility, "Electromagnetic lenses, apertures and beam size." `http://www.ammrf.org.au/myscope/sem/practice/principles/lenses.php`, 2014. [Online; accessed 16-January-2015].

[89] University at Buffalo, "SEM/EDS: Scanning electron microscopy with x-ray microanalysis." `http://wings.buffalo.edu/faculty/research/scic/sem-eds.html`. [Online; accessed 16-January-2015].

[90] V. B. Özdöl, V. Srot, and P. A. van Aken, "Sample Preparation Techniques for Transmission Electron Microscopy," in *Handbook of Nanoscopy* (G. Van Tendeloo, D. Van Dyck, and S. J. Pennycook, eds.), vol. 1, pp. 473–498, Wiley-VCH Verlag GmbH & Co. KGaA, 2012.

[91] D. B. Williams and C. B. Carter, *Transmission Electron Microscopy: A Textbook for Materials Science*, ch. 10: Specimen Preparation, pp. 173–193. Springer US, second ed., 2009.

[92] M. W. Allen, M. M. Alkaisi, and S. M. Durbin, "Metal Schottky diodes on Zn-polar and O-polar bulk ZnO," *Applied Physics Letters*, vol. 89, no. 10, p. 103520, 2006.

[93] U. Grossner, S. Gabrielsen, T. M. Børseth, J. Grillenberger, A. Y. Kuznetsov, and B. G. Svensson, "Palladium Schottky barrier contacts to hydrothermally grown n-ZnO and shallow electron states," *Applied Physics Letters*, vol. 85, no. 12, pp. 2259–2261, 2004.

[94] I. Yonenaga, "Hardness, Yield Strength and Dislocation Velocity in Elemental and Compound Semiconductors," *Materials Transactions*, vol. 46, no. 9, pp. 1979–1985, 2005.

[95] P. Eyben, W. Vandervorst, D. Alvarez, M. Xu, and M. Fouchier, "Probing semiconductor technology and devices with scanning spreading resistance microscopy," in *Scanning probe microscopy: Electrical and electromechanical phenomena at the nanoscale* (S. Kalinin and A. Gruverman, eds.), vol. 1, ch. 2, pp. 31–87, Springer science+business media, 2007.

[96] Struers, "Cold mounting product guide." `http://ipaper.ipapercms.dk/StruersAS/ColdMountingEnglish/`. [Online; accessed 22-February-2016].

[97] E. H. Enoksen, "Diffusion of potential p-type dopants in crystalline ZnO," Master's thesis, University of Oslo, 2016. [Not yet published].

[98] H. Qiu, F. Gallino, C. Di Valentin, and Y. Wang, "Shallow donor states induced by in-diffused Cu in ZnO: A combined HREELS and hybrid dft study," *Phys. Rev. Lett.*, vol. 106, p. 066401, 2011.

[99] F. Gallino and C. Di Valentin, "Copper impurities in bulk ZnO: A hybrid density functional study," *The Journal of Chemical Physics*, vol. 134, no. 14, 2011.

[100] T. Børseth, J. Christensen, K. Maknys, A. Hallén, B. Svensson, and A. Kuznetsov, "Annealing study of Sb^+ and Al^+ ion-implanted ZnO," *Superlattices and Microstructures*, vol. 38, no. 4-6, pp. 464–471, 2005. E-MRS 2005 Symposium G: ZnO and Related MaterialsPart 12005 European Materials Research Society Spring Meeting.

[101] R. Schifano, M. Schofield, L. Vines, S. Diplas, E. V. Monakhov, and B. G. Svensson, "Al and Si doping of sputtered ZnO thin films," *IOP Conference Series: Materials Science and Engineering*, vol. 34, no. 1, p. 012007, 2012.

[102] S. Limpijumnong, S. B. Zhang, S.-H. Wei, and C. H. Park, "Doping by large-size-mismatched impurities: The microscopic origin of arsenic- or antimony-doped *p*-type zinc oxide," *Phys. Rev. Lett.*, vol. 92, p. 155504, 2004.

[103] L.-W. Lai, C.-H. Liu, C.-T. Lee, L.-R. Lou, W.-Y. Yeh, and M.-T. Chu, "Investigation of silicon nanoclusters embedded in ZnO matrices deposited by cosputtering system," *Journal of Materials Research*, vol. 23, pp. 2506–2511, 9 2008.

[104] K. S. Chan, L. Vines, L. Li, C. Jagadish, B. G. Svensson, and J. Wong-Leung, "Equilibrium shape of nano-cavities in H implanted ZnO," *Applied Physics Letters*, vol. 106, no. 21, 2015.

[105] Y. Wang, J. Zou, Y. J. Li, B. Zhang, and W. Lu, "Mn behaviors in Mn-implanted ZnO," *Acta Materialia*, vol. 57, no. 7, pp. 2291–2299, 2009.

[106] B. B. Aarseth, "Ion implantation of ZnO by the group IV elements Si and Ge: Doping, defects and nonocrystallization," Master's thesis, University of Oslo, 2016. [Not yet published].